

**Magma storage and ascent of historic and
prehistoric eruptions of Fogo,
Cape Verde Islands:
A barometric, petrologic and geochemical
approach**

Dissertation

for the doctorate degree
of the Department of Geosciences
at the University of Bremen

Submitted by

Elliot Hildner

Bremen, September 2011

Promotionskolloquium: 11.11.2011

Mitglieder der Kommission:

PD Dr. Andreas Klügel

PD Dr. Frank Lisker

Prof. Dr. Heinrich Villinger

PD Dr. Thor H. Hansteen

PD Dr. Matthias Zabel

Alexander Diehl

Vertreter:

Prof. Dr. Reinhard X. Fischer

Dr. Niels Jöns

Melanie Siegburg

ERKLÄRUNG

Name: Elliot Hildner

Anschrift: Sedanstr. 86, 28201 Bremen

Hiermit versichere ich, dass ich

1. die Arbeit ohne unerlaubte fremde Hilfe angefertigt habe,
2. keine anderen als die von mir angegebenen Quellen und Hilfsmittel benutzt habe und
3. die den benutzten Werken wörtlich oder inhaltlich entnommen Stellen als solche kenntliche gemacht habe.

Bremen, den 20.09.2011

*There is a crack
A crack in everything
That's how the light gets in*

Leonard Cohen, Anthem

Table of contents

Abstract.....	1
Zusammenfassung.....	3
I Introduction.....	5
The Cape Verde Islands.....	7
Fogo.....	8
Aims of the study.....	12
Overview of research.....	14
II Magma storage and ascent during the 1995 eruption of Fogo,.....	15
Cape Verde Archipelago	
<i>Hildner E, Klügel A, Hauff F</i>	
Submitted to Contributions to Mineralogy and Petrology: received 24.11.2010;	
accepted 28.02.2011; published online 16.03.2011	
Abstract.....	16
2.1. Introduction.....	17
2.2. Geological setting.....	20
2.2.1. Geology of Fogo.....	20
2.2.2. Chronology of the 1995 eruption.....	20
2.2.3. Precursory and coeval seismicity.....	21
2.3. Petrography.....	22
2.3.1. Early erupted phonotephrites.....	22
2.3.2. Basanites.....	22
2.3.3. Occurrence of fluid inclusions.....	24
2.4. Analytical methods.....	26
2.5. Results.....	29
2.5.1. Whole-rock geochemistry.....	29
2.5.2. Microthermometry of fluid inclusions.....	34
2.5.3. Clinopyroxene-melt geothermobarometry.....	38
2.5.4. Zonations of olivine phenocrysts.....	40
2.6. Discussion.....	44
2.6.1. Interpretation of microthermometric data.....	44
2.6.2. Depths of magma stagnation and fractionation.....	45
2.6.3. Constraints on magma ascent rates.....	47
2.6.4. Differentiation of the 1995 magmas.....	48
2.6.5. Is there a deep connection between Fogo and Brava?.....	49
2.7. Conclusions.....	51
2.8. Acknowledgements.....	52
2.9. References.....	53

III	Barometry of lavas from the 1951 eruption of Fogo, Cape Verde Islands: implications for historic and prehistoric magma plumbing systems	57
<i>Hildner E, Klügel A, Hansteen TH</i>		
<i>Submitted to Journal of Volcanology and Geothermal Research: received 29.07.2011</i>		
Abstract.....	58	
3.1. Introduction.....	59	
3.2. Geological setting.....	62	
3.3.1. Geology of Fogo.....	62	
3.3.2. Historic activity.....	63	
3.3. Sampling and petrography.....	64	
3.3.1. Xenolith samples.....	66	
3.3.2. Occurrence of fluid inclusions.....	68	
3.4. Analytical methods.....	70	
3.5. Results.....	71	
3.5.1. Whole-rock geochemistry.....	71	
3.5.2. Clinopyroxene-melt geothermobarometry.....	74	
3.5.3. Microthermometry.....	80	
3.6. Discussion.....	86	
3.6.1. Interpretation of microthermometric data.....	86	
3.6.2. Depths of stagnation and differentiation of the 1951 magmas.....	87	
3.6.3. Comparison of the 1951 and 1995 magma plumbing systems.....	89	
3.6.4. Temporal evolution of the magma plumbing system.....	89	
3.7. Conclusions.....	94	
3.8. Acknowledgements.....	95	
3.9. References.....	96	
IV	Synthesis and Outlook.....	100
References.....	105	
Acknowledgements.....	108	
Appendix.....	110	
Appendix A.....	111	
Appendix B (on accompanying CD).....	122	

Abstract

Fogo is one of the most active oceanic intra-plate volcanoes in the world and the only island of the Cape Verde Archipelago showing historic activity. This study has been conducted to shed light on the magma plumbing systems of the island. In particular it aims to gain information on the depths of magma stagnation and differentiation, and on the ascent dynamics. Fogo was affected by a giant prehistoric lateral collapse that led to the removal of the summit and the eastern flank of the former Monte Amarelo volcano. The scar was partly refilled by intensive subsequent volcanic activity that is represented by the present-day Cha das Caldeiras plain and the young Pico do Fogo stratovolcano. During the 20th century Fogo experienced two eruptions in 1951 and 1995 that were both fed from fissures on the flanks of Pico do Fogo.

The 1995 eruption differed from earlier eruptions in a distinct chemical and mineralogical bimodality with phonotephrites (2.4-2.8 wt% MgO) being erupted in the first days and basanites (5.2-6.7 wt% MgO) in the later phase, the uncommon southwest orientation of the eruption fissure, and pre-eruptive seismicity between Fogo and the adjacent island of Brava. Geochemical modeling of major and trace elements shows that the phonotephrites formed out of the basanites by crystal fractionation. Clinopyroxene-melt barometry of phenocrysts yields overlapping pressure ranges for final crystal growth before eruption of 460-680 MPa for the basanites and 460-520 MPa for the phonotephrites, corresponding to 16-24 km depth in the lithospheric mantle. Microthermometry of CO₂-dominated fluid inclusions in basanites yield pressures of 270-440 MPa for olivine-hosted and 240-270 MPa for clinopyroxene hosted ones. Inclusions in phenocrysts of the phonotephrites yield a pressure range of 320-470 MPa for olivine-hosted and 200-310 MPa for clinopyroxene-hosted fluid inclusions. Fluid inclusions in olivine, especially of phonotephrites show overlapping pressures with the data of clinopyroxene-melt barometry. The lower pressures derived for clinopyroxene-hosted inclusions are interpreted to reflect a level of syn-eruptive short-term magma stagnation in the lower crust at 8-11 km depth. Chemical zonations of olivine phenocrysts indicate a rapid final magma ascent during eruption in <12 h, probably 1-4 h. Evidence for magma storage at shallow depths (<200 MPa) or for lateral magma movement below the Fogo-Brava platform is not provided by the data. Pb-Sr-Nd isotopic ratios of samples from Brava differ significantly from those of 1995 and older Fogo rocks and do not indicate magma contamination of 1995 magmas by Brava phonolites. The pre-eruptive seismicity may have been triggered by a propagating dike

related to the later 1995 eruption or to a group of active submarine volcanoes between Fogo and Brava.

The 1951 eruption was fed from different vents south and northwest of Pico do Fogo and produced basanites to tephrites (5.0-8.2 wt% MgO). The chemical heterogeneity of the lavas is due to variable phenocryst contents as shown by petrographic observations, least-square mass balance calculations and trace element patterns. Clinopyroxene-melt barometry yields pressure ranges of 480-650 MPa. Microthermometry of fluid inclusions yields 250-430 MPa for olivine and clinopyroxene phenocrysts, and 100-290 MPa for inclusions in xenoliths. The combined data indicate pre-eruptive magma storage and crystal fractionation in 17-22 km depth and short-term stagnation during eruption in 8-13 km depth in the lower crust, which is essentially identical with the depths calculated for the 1995 eruption. The xenolith data may indicate that they originate from earlier magma pulses that stalled and crystallized at variable levels within the crust. There is, however, no petrologic evidence for persistent crustal magma chambers.

Clinopyroxene-melt barometric data of historic and prehistoric eruptions comprising a time span of >100 ka, which includes the Monte Amarelo collapse, indicate that magma storage and differentiation occurred in the lithospheric mantle at pressures of 420-870 MPa (15-30 km depth) presumably throughout the subaerial evolution of Fogo. The fractionation depths decreased through time, though this trend was temporarily interrupted by the giant collapse because the oldest post-collapse eruption shows a deeper stagnation level than the youngest pre-collapse one. The petrologic data indicate that large flank collapses may significantly influence deep-seated magma plumbing systems beneath ocean islands. Historic eruptions show shallower and broader pressure ranges and more complexly zoned clinopyroxene phenocrysts, suggesting an increase in complexity of the magma storage system. The lack of shallow persistent magma chambers, however, may be a consequence of the cool Mesozoic crust and thick lithosphere beneath Fogo.

Zusammenfassung

Fogo ist einer der aktivsten ozeanischen Intraplatten-Vulkane der Welt und die einzige Insel der Kapverden, die historische vulkanische Aktivität aufweist. Diese Studie wurde durchgeführt, um Einblick in die Magmenförderersysteme der Insel und Informationen über die Stagnations- und Differentiationstiefen der Magmen und deren Aufstiegsdynamiken zu gewinnen. Fogo wurde von einem großen prähistorischen lateralen Kollaps heimgesucht, der den Gipfel und die östliche Flanke des ehemaligen Monte Amarelo-Vulkangebäudes entfernte. Das Kollapsbecken wurde durch die anschließende intensive vulkanische Tätigkeit, die sich in der heutigen Cha das Caldeiras-Ebene und im jungen Pico do Fogo-Stratovulkan konstituiert, teilweise wiederaufgefüllt. Während des 20. Jahrhunderts traten auf Fogo zwei Eruptionen in den Jahren 1951 und 1995 auf, beide wurden von Eruptionsspalten an den Flanken des Pico do Fogo gespeist.

Die 1995 unterschied sich von früheren Eruptionen durch eine deutliche chemische und mineralogische Bimodalität mit Phonotephriten (2.4-2.8 Gew.% MgO) in den ersten Tagen und der anschließenden Förderung von Basaniten (5.2-6.7 Gew.% MgO), durch eine ungewöhnliche Südwest-Orientierung der Eruptionsspalten und durch Magmenbewegung andeutende präeruptive seismische Aktivität zwischen Fogo und der Nachbarinsel Brava. Geochemische Modellierungen von Haupt- und Spurenelementen zeigen, dass die Phonotephrite durch Kristallfraktionierung aus den Basaniten hervorgegangen sind. Klinopyroxen-Schmelz-Barometrie von Phänokristallen liefert überlappende Druckbereiche für das letzte Kristallwachstum vor der Eruption von 460-680 MPa für die Basanite und 460-520 MPa für die Phonotephrite, entsprechend einer Tiefe von 16-24 km im lithosphärischen Mantel.

Mikrothermometrie von CO₂-dominierten Fluideinschlüssen in Phänokristallen der Basanite liefert Drücke von 270-440 MPa für Einschlüsse in Olivin und 240-270 MPa für Einschlüsse in Klinopyroxen. Einschlüsse in Phonotephriten liefern 320-470 MPa für Olivin und 200-310 MPa für Klinopyroxen. Einschlüsse in Olivin, speziell in den Phonotephriten, zeigen überlappende Druckbereiche mit den Daten der Klinopyroxen-Schmelz-Barometrie. Die geringeren Drücke, die für Einschlüsse in Klinopyroxen-Phänokristallen ermittelt wurden, werden als Anzeichen für ein Niveau kurzzeitiger syneruptiver Magmenstagnation in 8-11 km Tiefe in der unteren Kruste interpretiert. Chemische Zonierungen von Olivinphänokristallen deuten auf einen raschen finalen Magmenaufstieg während der Eruption in weniger als 12 h, wahrscheinlich in 1-4 h, hin. Die petrologischen Daten geben keine Hinweise für Magmenstagnation in geringen

Tiefen (<200 MPa) oder für lateralen Magmentransport unterhalb der Fogo-Brava-Plattform. Pb-Sr-Nd Isotopenverhältnisse von Brava-Proben unterscheiden sich deutlich von denen der 1995er und älteren Fogo-Gesteinen und deuten nicht auf eine Kontamination der 1995-Magmen durch Brava-Phonolite hin. Die prä-eruptive Seismizität kann durch einen propagierenden Magmengang im Zusammenhang mit der späteren 1995-Eruption oder mit einer Gruppe von aktiven Unterwasservulkanen zwischen Fogo und Brava ausgelöst worden sein.

Die Eruption von 1951 förderte Basanite bis Tephrite (5.0-8.2 Gew.% MgO) aus mehreren Schloten südlich und nordwestlich vom Pico do Fogo. Die leichte chemische Heterogenität ist variablen Phänokristallgehalten geschuldet, was durch petrographische Beobachtungen, Massenbilanzierungen und Spurenelement-Muster gezeigt werden kann. Klinopyroxen-Schmelz-Barometrie liefert Druckbereiche von 480-650 MPa, während Fluideinschlussdaten von Olivin- und Klinopyroxen-Phänokristallen 250-430 MPa, und Einschlüsse in Xenolithen 100-290 MPa anzeigen. Die kombinierten Daten implizieren präeruptive Magmenstagnation und Kristallfraktionierung in 17-22 km Tiefe und kurzzeitige Stagnation während der Eruption in 8-13 km Tiefe in der unteren Kruste. Diese Tiefen sind essenziell identisch mit denen, die für die Eruption von 1995 ermittelt wurden. Die Xenolithe stammen vermutlich von früheren Magmenschüben, die in unterschiedlichen Niveaus in der Kruste stagnierten und kristallisierten. Es gibt jedoch keine petrologischen Hinweise für langlebige krustale Magmenkammern.

Klinopyroxen-Schmelz-Barometriedaten von historischen und prähistorischen Eruptionen, die eine Zeitspanne von > 100 ka und den Monte Amarelo-Kollaps umfassen, zeigen, dass Magmenstagnation und -differentiation vermutlich während der gesamten subaerischen Entwicklung von Fogo im Druckbereich von 420-870 MPa (15-30 km Tiefe) im lithosphärischen Mantel stattfand. Die Fraktionierungstiefen nahmen im Laufe der Zeit ab, wobei dieser Trend mutmaßlich vom Flankenkollaps unterbrochen wurde, da die älteste Postkollaps-Eruption ein deutlich tieferes Stagnationsniveau aufweist als die jüngste Prækollaps-Eruption. Die petrologischen Daten zeigen, dass große Flankenkollapsereignisse tiefliegende Magmenförderersysteme von Ozeaninseln erheblich beeinflussen können. Die historischen Eruptionen weisen flachere und breitere Druckbereiche und komplexer zonierte Klinopyroxen-Phänokristalle auf, was auf eine Zunahme der Komplexität der Magmenförderersysteme hindeutet. Das mutmaßliche Fehlen von flachen, langlebigen Magmenkammern scheint hingegen eine Folge der kalten mesozoischen Kruste und der dicken Lithosphäre unter Fogo zu sein.

I

Introduction

Research into the magma plumbing systems of active volcanoes is essential for our understanding of magmatic processes preceding and accompanying volcanic eruptions and for estimating the hazard potential of volcanic systems. Intra-plate volcanism is commonly interpreted as the surface manifestation of a thermal anomaly in the underlying mantle due to a plume of uprising hot mantle material (Morgan 1971). The evolution of intra-plate magma plumbing systems is controlled by various geodynamic conditions such as depth and degree of melting, the magma supply rate, the plate motion dynamics and the thermomechanic properties of the crust and the lithospheric mantle (e.g. Clague and Dixon 2000). The depths of magma stagnation and differentiation, the migration pathways of ascending magmas and the eruption dynamics are therefore very variable among different intra-plate volcanic archipelagos or islands. Besides geophysical methods, petrologic investigations of erupted volcanic products are the main approach in gaining depth information of magmatic processes occurring in the Earth's mantle and crust. Magma differentiation depths can be reconstructed by phase relationships, mineral-melt geothermobarometry and by fluid inclusion barometry; the latter even allows the identification of short-term stagnation events in the order of hours to days (Wanamaker et al. 1990; Klügel et al. 2005). In case of the last eruption of Fogo in 1995, seismic and ground deformation data are published (e.g. Amelung and Day 2002; Héleno 2003) and hypotheses of magma stagnation before and during eruption, and ascent dynamics are tested for the first time by petrologic approaches in the present thesis.

Petrologic studies addressing the magma pathways from the mantle to the surface have been carried out for many intra-plate oceanic volcanic systems like the Canary Islands, Madeira Archipelago, Hawaii and Galápagos. Magma plumbing systems of the Canary Islands and Madeira Archipelago tend to establish volcanic rift zones in their shield building phase, but in contrast to Hawaii, these rift zones are not fed by shallow subcaldera magma chambers. Major magma storage and differentiation commonly occurs within the lithospheric mantle or near the Moho. Ephemeral shallow magma chambers within the crust or the volcanic edifice were not observed for La Palma, El Hierro and Madeira, but short-term magma stagnation within the crust and the volcanic

edifices before and during eruptions is common (Hansteen et al. 1998; Klügel et al. 2000; Nikogosian et al. 2002; Schwarz et al. 2004; Klügel et al. 2005; Galipp et al. 2006; Longpré 2008; Stroncik et al. 2009).

Hawaiian volcanoes in their shield-building stage tend to develop summit calderas underlain by shallow magma reservoirs that feed well-established volcanic rift zones by lateral magma transport (e.g. Tilling and Dvorak 1993; Walker 1999). Within these rift zones magma can be temporarily stored and remobilized by subsequently ascending magmas (Garcia et al. 1989). Below the summit reservoir, magma storage occurs over a range of depths within the lithosphere, as is indicated by the progressive emptying of the plumbing system from shallow to deeper levels during sustained eruptions (Putirka 1997).

On Galápagos magma differentiation takes part in several depth levels ranging from very shallow crustal magma chambers to transient magma chambers in the upper mantle. Fractionation depths vary systematically throughout the archipelago in dependency on the magma supply rate and/ or regional differences in the structure of the lithosphere that is affected by a major transform fault and the nearby Galápagos spreading center (Geist et al. 1998). The depths of magma fractionation apparently control the occurrence of the volcanic edifices. Deep calderas are underlain by very shallow magma chambers whereas broad, shallow calderas are connected to magma differentiation in the deeper crust and the lithospheric mantle (Geist et al. 1998).

During their evolution most oceanic volcanic islands become substantially affected by lateral collapses due to flank instability. Numerous collapse structures and/ or their submarine debris avalanches in the order of tens to several thousand km³ have been detected at Hawaiian and Canary Islands (e.g. Moore et al. 1994; McGuire 1996; Masson et al. 2002) and recently at the Cape Verde Archipelago (Masson et al. 2008). A number of studies have identified mechanisms that trigger flank collapses. It was found that magmatic intrusion, the reactivation of basement faults, and hydrothermal alteration of the edifice are important triggering agents (e.g. Voight and Elsworth 1997; Elsworth and Day 1999; Vidal and Merle 2000). In recent years the effects of flank collapses on the magma plumbing systems have become topic in several studies especially on Hawaiian and Canary Islands. Common observations are that in many cases dense, crystal-rich lavas erupt immediately after large flank collapses which has been attributed to the apparent disturbance of the magma plumbing systems (e.g. Presley et al. 1997; Longpré et al. 2009; Manconi et al. 2009), and that subsequent volcanic

activity is concentrated inside the collapse scar (Day et al. 1999; Tibaldi 2004; Masson et al. 2008). Although large lateral flank collapses of oceanic island volcanoes have not occurred in historic time, their hazard potential should not be underestimated.

Considering the unique characteristics of the Cape Verde Islands (discussed in the next section), their magmatic evolution is surprisingly little examined compared with other oceanic intra-plate volcanic settings like Hawaii and the Canary Islands. So far almost nothing is known about the magma pathways and fractionation depths of Cape Verde volcanoes. Only for the submarine stage of Santiago a few barometric data are available, indicating magma fractionation within the lithospheric mantle (Barker et al. 2009). The major goal of this thesis is to shed light on the magma plumbing systems of the active island of Fogo, which is a candidate for future hazardous eruptions and potential renewed flank instability (Day et al. 1999). Before concentrating on the specific issues addressed in this work, a brief summary of the geological setting of the Cape Verde Islands and the volcanic history of Fogo are presented in the next section.

The Cape Verde Islands

The Cape Verde Islands (Fig. 1) represent the top of the Cape Verde swell, a large region of up to 2.2 km elevated seafloor (>1000 km in diameter) of Mesozoic age (125-141 Ma, Courtney and White 1986) that is associated with the underlying Cape Verde mantle plume (McNutt 1988). The Cape Verde swell represents the largest bathymetric and geoid anomaly in the oceans (Lodge and Hellfrich 2006) that is located near the rotational pole of the slowly moving African plate and therefore almost stationary in the hotspot frame of reference (Pollitz 1991). Seismic tomographic studies have revealed a plume-like mantle anomaly beneath the swell reaching down to depths of ≥ 1900 km (Montelli et al. 2004). The islands are arranged in a horseshoe shape open to the west and show a rough age progression from east to west along the northern and the southern island chains. Volcanic activity was initiated at least in the early Miocene at 24-22 Ma (summarized in Holm et al. 2008). Magmatism involves predominantly alkalic silica-undersaturated melts of basanitic to tephritic composition, but phonolites and carbonatites also occur on several islands.

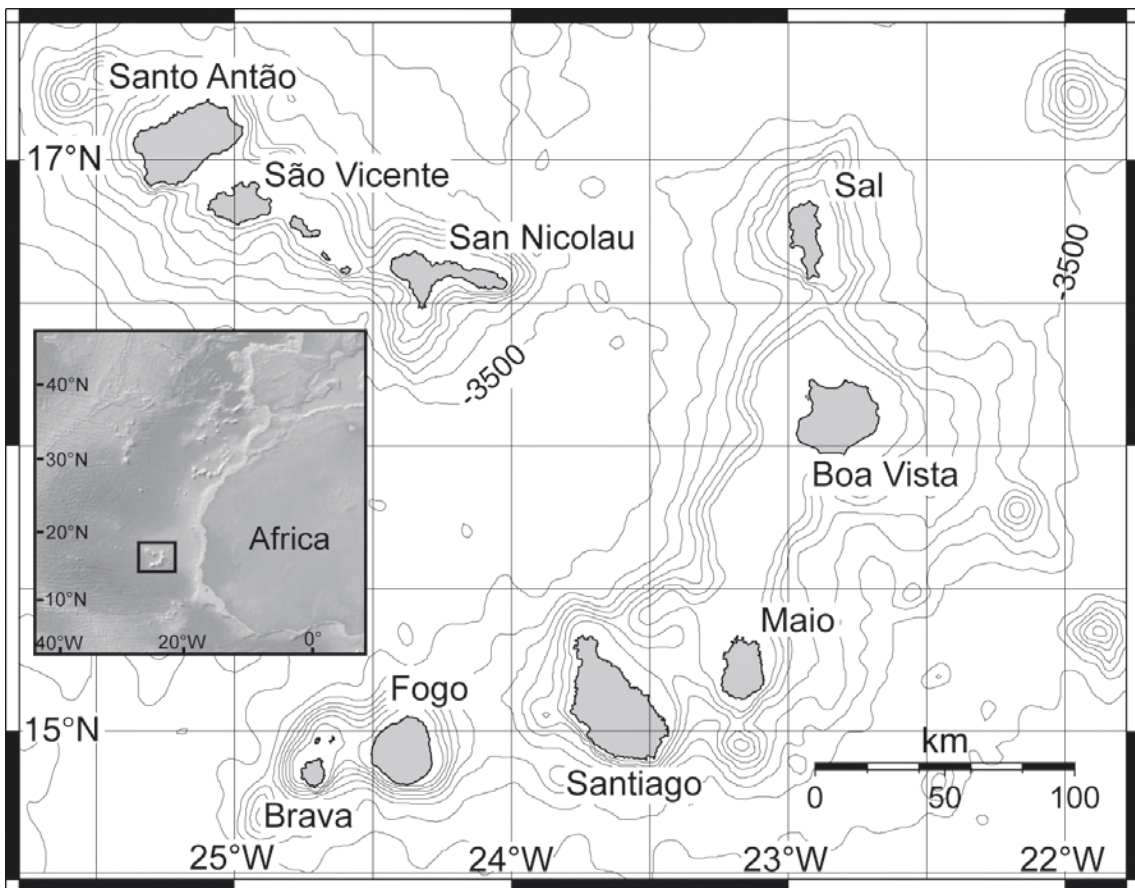


Fig. 1 Location and overview map of the Cape Verde Archipelago with 500m bathymetric contours

Fogo

Fogo is one of the most active oceanic volcanoes on Earth with almost 30 eruptions since its discovery in the 15th century (Ribeiro 1960; Torres et al. 1997). The island shares its volcanic apron with the adjacent island of Brava (Fig. 2) at the southwestern end of the archipelago. Fogo is the only Cape Verde island exhibiting historic volcanic activity, whereas Brava is seismically more active (Heleno 2003). Fogo has a diameter of 25 km and reaches its maximum height at Pico do Fogo stratovolcano (2829 m above sea level) that is encircled to the west by the steep, up to 1000 m high Bordeira cliff (Fig. 3). The Bordeira represents the headwall of a prehistoric, east-directed giant lateral landslide (Monte Amarelo collapse) that has been dated to 123-62 ka (Foeken et al. 2009). The collapse scar has become partly infilled by subsequent intensive volcanic activity, as is now represented by the Cha das Caldeiras plain and the young Pico do Fogo stratovolcano (Fig. 3). Historic volcanic activity was almost restricted to Pico and the inhabited (~1000 residents) Cha das Caldeiras area. The two most recent eruptions of Fogo occurred in 1951 and 1995, where parts of the villages and large agricultural

areas were destroyed by lava flows. Since the last eruption Fogo is permanently geophysically observed by the VIGIL network (Fonseca et al. 2003).

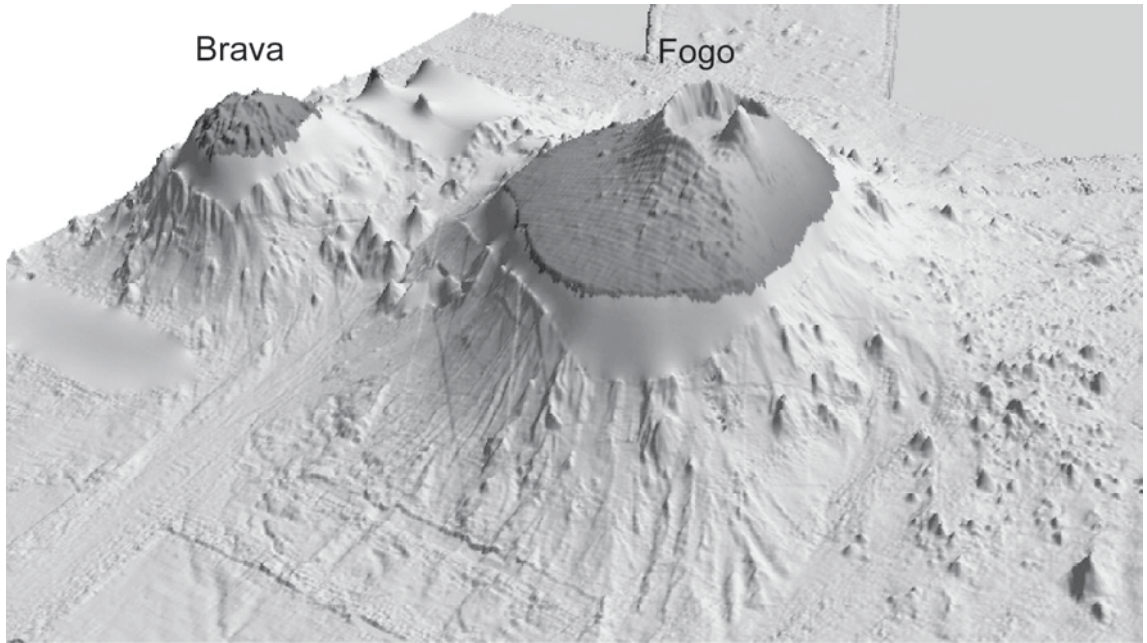


Fig. 2 Three-dimensional topographic and bathymetric model of the Fogo-Brava platform viewed from the southeast. East of Fogo the landslide debris of the Monte Amarelo collapse is clearly visible. Between Fogo and Brava a group of young volcanic cones arises from the seafloor. Modified after Masson et al. (2008)

The geological history of Fogo can be subdivided into four phases according to Day et al. (1999) and Foeken et al. (2009): (1) an uplifted seamount series composed of carbonatites and alkaline basalts that has been dated to ~4.5 Ma. (2) The oldest subaerial lavas (Monte Barro Group) that unconformably overlie the carbonatites lack absolute age constraints. (3) The 2-3 km thick Monte Amarelo Group consisting of highly alkaline basic to intermediate lavas and scoria cones. Absolute age constraints are lacking, but these rocks may be entirely of Quaternary age. The Monte Amarelo Group ended with a giant lateral collapse. (4) The Cha das Caldeiras Group (62 ka to present) that is represented by an approximately 2 km thick collapse-scar infill sequence of alkaline volcanic rocks comprising the Cha das Caldeiras plain and Pico do Fogo, as well as discontinuous lava sequences and scoria cones on the outer flanks of the island.

Amelung and Day (2002) proposed the existence of an enduring shallow crustal magma chamber for the Monte Amarelo volcano that has been removed by the giant lateral collapse. The time that passed since this event is regarded to be too short for the re-establishing of shallow reservoirs within the magma plumbing system. An important goal of this study is therefore the investigation of petrologic evidence for shallow

magma chambers throughout the history of Fogo and especially at the late Monte Amarelo volcano.

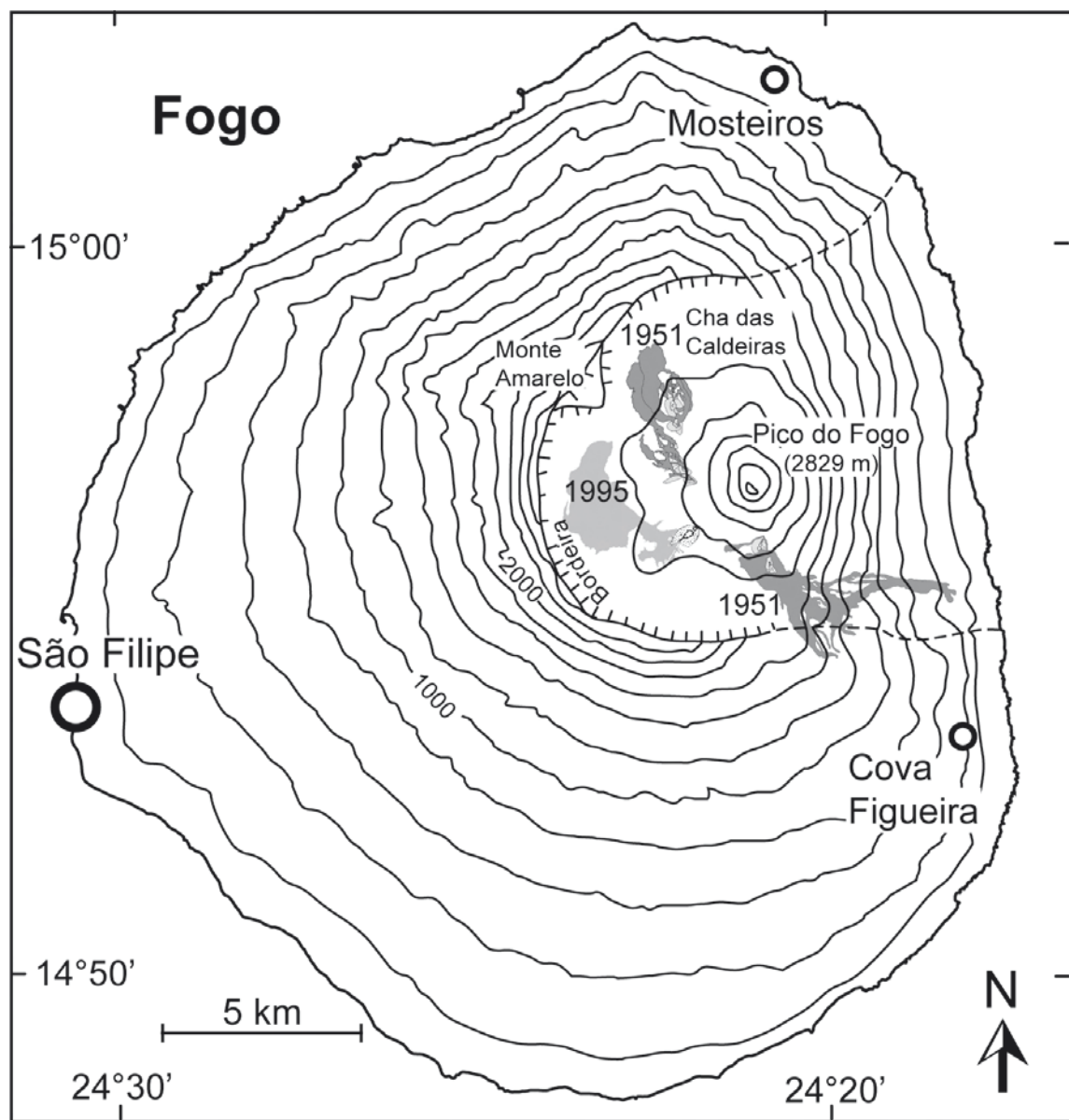


Fig. 3 Map of Fogo with 200 m topographic contours showing the eruption products of the two most recent eruptions of 1995 and 1951, center of research in this thesis. The most prominent features of the island's topography are the up to 1000 m high cliff (Bordeira) representing the headwall of the prehistoric east-directed Monte Amarelo collapse and the young Pico do Fogo stratovolcano arising within the collapse scar.

Historic activity

Eyewitness reports of the historic activity of Fogo since 1500 were collected and studied by Ribeiro (1960) and resumed by Day et al. (2000). In the almost 500 years of witnessed activity significant changes over time were recognized. From about 1500 to 1769 eruptive activity was concentrated on the Pico do Fogo summit itself. Eruptions were prolonged and frequent, but periods of quiescence also occurred throughout decades. Within the 18th century activity changed from summit eruptions of Pico do Fogo to predominantly north-south oriented fissure eruptions at Pico's flanks. The last eruption involving the Pico summit took place in 1785. This shift in activity was interpreted as a structural reconfiguration of the volcanic system and renewed instability of the eastern flank of Fogo (Day et al. 1999).

The two most recent eruptions of 1951 and 1995

The eruptions of 1995 and 1951 are of special interest in this thesis because both are well documented and the eruption products of almost all eruption phases are accessible. A detailed study of those two eruptions therefore promises profound insight into the recent dynamics of the magma plumbing system of Fogo.

The 1951 eruption lasted from June 12th to August 21st and ejected a lava volume of $1.1 \times 10^7 \text{ m}^3$ (Global Volcanism Program, Smithsonian Institute). Detailed descriptions of the course of the eruption can be found in Ribeiro (1960) and Day et al. (2000) and are briefly summarized here. The activity began with the opening of two vents at the southern slope of Pico do Fogo. On the second day several vents opened along a north-propagating fissure at the western slope of Pico. Finally activity concentrated at a single vent northwest of Pico that was, together with one vent south of Pico, active until the end of the eruption (Fig. 3). The eruption fissures showed a north-south orientation similar to previous historic eruptions but feature distinctive en-echelon segmentation especially at the western slope of Fogo. The extruded lavas were basanites to tephrites (Kokfelt et al. 1998). However, a detailed petrologic and geochemical study of the eruption was not carried out until now.

The 1995 eruption lasted from April 2nd to May 26th and ejected a lava volume of $2.9 \times 10^6 \text{ m}^3$ (Global Volcanism Program, Smithsonian Institute) and a total volume of volcanic material of $54-68 \times 10^6 \text{ m}^3$ (Torres et al. 1997). In contrast to other historic eruptions this one showed a distinct chemical bimodality with phonotephrites being

ejected in the first days and basanites during later stages (Munhá et al. 1997; Kokfelt 1998). The eruption was fed by an untypically northeast-southwest oriented fissure parallel to the orientation of the Fogo-Brava platform (Fig. 2) at the southwest flank of Pico do Fogo. On the basis of satellite derived interferograms Amelung and Day (2002) have postulated a depth of >16.5 km of the magma reservoir that fed the 1995 eruption. The eruption was preceded by a small seismic crisis in early 1994 beneath the Fogo-Brava-platform, and beneath and west of Brava; on Fogo, a swarm of microearthquakes occurred towards the southwest of the island (Heleno da Silva et al. 1997, Heleno 2003). The volcano-tectonic seismicity was interpreted to have been triggered by magma movement (Heleno and Fonseca 1999). These indications for possible lateral magma transport between Fogo and Brava and the extraction of uncommonly evolved rocks during the 1995 eruption in combination with the predominantly phonolitic volcanism of Brava led to the assumption of an interrelation of the magma plumbing systems of both islands (Heleno 2003). Such lateral magma transport between distinct volcanic edifices in the order of up to 30 km was inferred at other localities like Hawaii (Rhodes et al. 1989) and Galápagos (Geist et al. 1999) and based on geochemical and petrologic data.

Aims of the study

The goal of this comprehensive geothermobarometric, petrologic and geochemical study is to shed light on the magma plumbing systems of Fogo by investigating the eruption products of several historic and prehistoric eruptions inside and outside the collapse scar of the Monte Amarelo landslide. Based on its distinctive features and the possible magmatic interaction with Brava, a special focus is set onto the 1995 eruption. Another main issue is the well-described but little investigated 1951 eruption that, in contrast to the one of 1995, resembles most features of the historic activity since 1785. The analysis of several historic and prehistoric eruption products is expected to provide insight into the temporal evolution of Fogo's magma plumbing systems.

The major objectives of the study are:

- the investigation of magma stagnation and differentiation depths and the reconstruction of the ascent dynamics of the magmas of the 1995 eruption

- to test the hypothesis that lateral magma transport occurred below the Fogo-Brava platform before or during the 1995 eruption as seems to be indicated by seismic studies
- the clarification of the relationship between the early erupted phonotephrites and the subsequently ejected basanites
- to find out whether the 1995 magmas were contaminated by Brava phonolites
- the reconstruction of the magma stagnation and differentiation depths of the 1951 eruption, and the investigation of the chemical and petrologic properties of the ejected lavas
- the documentation of changing depths of magma differentiation during the evolution of Fogo
- to test the hypothesis of a shallow magma chamber that was removed by the giant lateral collapse (Amelung and Day 2002) and research into petrologic evidence for shallow magma chambers in the history of Fogo
- the investigation of a possible influence of the giant lateral Monte Amarelo collapse on the magma plumbing systems and the depths of magma differentiation

The methods applied to achieve these aims are, besides the field studies, geothermobarometry (clinopyroxene-melt thermobarometry, fluid inclusion microthermometry), and geochemical analyses (major and trace elements, Pb-Sr-Nd isotopes).

Overview of research

This dissertation comprises a comprehensive study of the magma plumbing system of Fogo as an example of a hotspot related active intra-plate volcanic island in the North Atlantic. The results are presented in two self-contained chapters. Chapter 2 has been published and chapter 3 is in review.

CHAPTER II: Magma storage and ascent during the 1995 eruption of Fogo, Cape Verde Archipelago (Hildner E, Klügel A and Hauff, 2011, Contributions to Mineralogy and Petrology, doi: 10.1007/s00410-011-0623-6)

This paper focuses on the chemically and mineralogically bimodal 1995 eruption and presents clinopyroxene-melt thermobarometric and fluid inclusion barometric data from clinopyroxene and olivine phenocrysts to investigate the depths of magma fractionation and stagnation. Diffusion modeling by using chemical profiles of olivine phenocrysts gives insight into the duration of final magma ascent to the surface during eruption. Geochemical and Sr-Nd-Pb isotopic whole-rock data of Fogo and the neighboring island of Brava are presented to verify geophysical indications for shallow lateral magma transport below the Fogo-Brava platform and possible connections of the magma plumbing systems of both islands. In the paper a model of the magma plumbing system and the magma ascent dynamics of the 1995 eruption is developed.

CHAPTER III: Barometric study of historic and prehistoric lavas of Fogo, Cape Verde Islands: the 1951 eruption and implications for the evolution of the magma plumbing system (Hildner E, Klügel A and Hansteen TH, submitted to Journal of Volcanology and Geothermal Research, 29.07.2011)

This paper focuses on the penultimate 1951 Fogo eruption and presents clinopyroxene-melt geothermobarometric data of phenocrysts and fluid inclusion barometric data of olivine and clinopyroxene phenocrysts and xenoliths that are used to reconstruct the magma plumbing system of the eruption. In addition, data of several historic and prehistoric eruptions covering a time period of more than 100 ka allow insight into the temporal evolution of Fogo's magma plumbing system and document effects of the giant lateral Monte Amarelo collapse.

II

Magma storage and ascent during the 1995 eruption of Fogo, Cape Verde Archipelago

Elliot Hildner¹, Andreas Klügel¹, Folkmar Hauff²

¹Universität Bremen, Fachbereich Geowissenschaften, Bremen, Germany

²IFM-GEOMAR, Leibniz Institute of Marine Sciences, Kiel, Germany

Published in Contributions to Mineralogy and Petrology

Received: 24.11. 2010, accepted: 28.02. 2011, published online: 16.03. 2011

Doi: 10.1007/s00410-011-0623-6



Pico do Fogo stratovolcano and Pico Pequeno scoria cone (1995 eruption)

Abstract

The 1995 eruption of Fogo (Cape Verde Islands) differed from previous eruptions by the occurrence of evolved lavas, the SW-orientation of vents, and pre-eruptive seismicity between Fogo and the adjacent (~ 20 km) island of Brava. We have conducted a thermobarometric and chemical study of this eruption in order to reconstruct its magma plumbing system and to test for possible connections to Brava. The bimodal eruption produced basanites (5.2 - 6.7 wt% MgO) and phonotephrites (2.4 - 2.8 wt% MgO) that are related by fractional crystallization. Clinopyroxene-melt-barometry of phenocrysts yields pressure ranges of 460-680 MPa for the basanites and 460-520 MPa for the phonotephrites. Microthermometry of CO₂-dominated fluid inclusions in olivine and clinopyroxene phenocrysts yields systematically lower pressure ranges of 200-310 MPa for basanites and 270-470 MPa for phonotephrites. The combined data indicate pre-eruptive storage of the 1995 magmas within the lithospheric mantle between 16 and 24 km depth. During eruption the ascending magmas stalled temporarily at 8-11 km depth, within the lower crust, before they ascended to the surface in a few hours as indicated by zonations of olivine phenocrysts. Our data provide no evidence for magma storage at shallow levels (<200 MPa) or lateral magma movements beneath the Fogo-Brava platform. Sr-Nd-Pb isotope ratios of samples from Brava differ significantly from those of the 1995 and older Fogo lavas, which rules out contamination of the 1995 magmas by Brava material and indicates different mantle sources and magma plumbing systems for both islands.

Keywords: *Fogo, Cape Verde, Thermobarometry, Fluid inclusions, Pb-Sr-Nd isotopes*

2.1. Introduction

Storage depths and migration paths of magmas have strong control on the evolution of magmatic systems and the dynamics of volcanic eruptions. Our understanding of pre-eruptive magmatic processes therefore critically relies on knowledge about the plumbing systems. Besides geophysical methods, petrological investigation of erupted products is the main approach that can give insight into processes occurring in the Earth's mantle and crust. The combination of petrological with geophysical data, where possible, is particularly rewarding (e.g. Peccerillo et al. 2006). For intra-plate volcanic islands, the largest volcanoes on Earth, a number of petrological studies have focused on magma storage and migration from mantle to surface (e.g. Garcia et al. 1989; Putirka 1997; Hansteen et al. 1998; Chatterjee et al. 2005; Klügel et al. 2000; Schwarz et al. 2004; Galipp et al. 2006; Stroncik et al. 2009). For the Cape Verde Archipelago, such studies have not been carried out so far, and geobarometric data are sparse (Munhá et al. 1997; Barker et al. 2009).

Fogo and the adjacent smaller island of Brava are situated on the Fogo-Brava platform at the southwestern end of the Cape Verde Archipelago (Fig. 1). Fogo is one of the world's most active volcanoes with about 30 eruptions since ~1500 AD, the last occurring in 1995 (Torres et al. 1997). Remarkably, even though Fogo is the only Cape Verde island with historic volcanic activity, Brava is more active seismically. Most of the recent seismic activity on the archipelago occurs below the shallow channel between both islands and at Cadamosto seamount southwest of Brava (Fig. 1; Heleno 2003; Helffrich et al. 2006; Grevemeyer et al. 2010). These observations, and the discovery of numerous small volcanic cones between Cadamosto and Brava and between Fogo and Brava, led Grevemeyer et al. (2010) to postulate two magma plumbing systems in this region, one feeding Fogo and the volcanic cones between Fogo and Brava, and another one feeding the Cadamosto seamount. The investigation of a possible connection between Fogo and Brava is a main focus of our study.

The 1995 eruption on Fogo is of particular interest for a detailed study on magma plumbing because it is well documented by eyewitness accounts, and seismic data were recorded before, during, and after the eruption (summarized in Réffega et al. 1997). On the basis of satellite-derived interferograms, Amelung and Day (2002) argued that ground deformation during the 1995 eruption resulted from a feeder dike but not from a shallow magma chamber, and suggested that magma rose from a reservoir at >16.5 km

depth. In contrast, Munhá et al. (1997) inferred a magma reservoir at 13 ± 3 km depth based on thermodynamic modeling using mineral compositions from ultramafic Fogo xenoliths. The 1995 eruption also shows the following peculiarities: 1) The main eruptive fissure of 1995 was oriented WSW-ENE, towards Brava island, in contrast to most other historic eruptions since 1785 where fissures were oriented roughly N-S (Day et al. 1999, Fig. 1). 2) The eruption was mineralogically and chemically zoned and produced phonotephrites, which are more evolved than other historic lavas (Munhá et al. 1997). This may be reminiscent of Brava, where phonolite rather than basalt is the most abundant recent rock type (Wolff and Turbeville 1985). 3) Seismic observations in January 1994 gave evidence for magma movements under the channel between Fogo and Brava, at depths of probably 2-7 km (Heleno da Silva et al. 1997) that could be related to the 1995 eruption.

Because of these observations, Heleno (2003) suggested a possible connection between the magma plumbing systems of Fogo and Brava, and proposed that the evolved 1995 magmas could have been contaminated by Brava phonolites. This scenario would require lateral magma movement beneath the Fogo-Brava platform, as has been proposed for other localities such as Hawaii (Rhodes et al. 1989) and Galápagos (Geist et al. 1999) based on geochemical and petrological data. Alternatively, the unusual fissure orientation and the more evolved character of the 1995 lavas, and the seismic crisis in 1994 near Brava could be coincidental.

In order to shed more light on Fogo's magma plumbing system, we have carried out a detailed petrological and geochemical study of the 1995 eruption with a focus on geobarometry. The main goals of our study are 1) to determine the depths of storage of the 1995 magmas; 2) to reconstruct magma pathways and ascent dynamics of the eruption; and 3) to test the hypothesis that magma migrated between Brava and Fogo during the eruption. The results improve our understanding of Fogo's recent magma plumbing system and therefore support the ongoing monitoring activities of this potentially hazardous volcano.

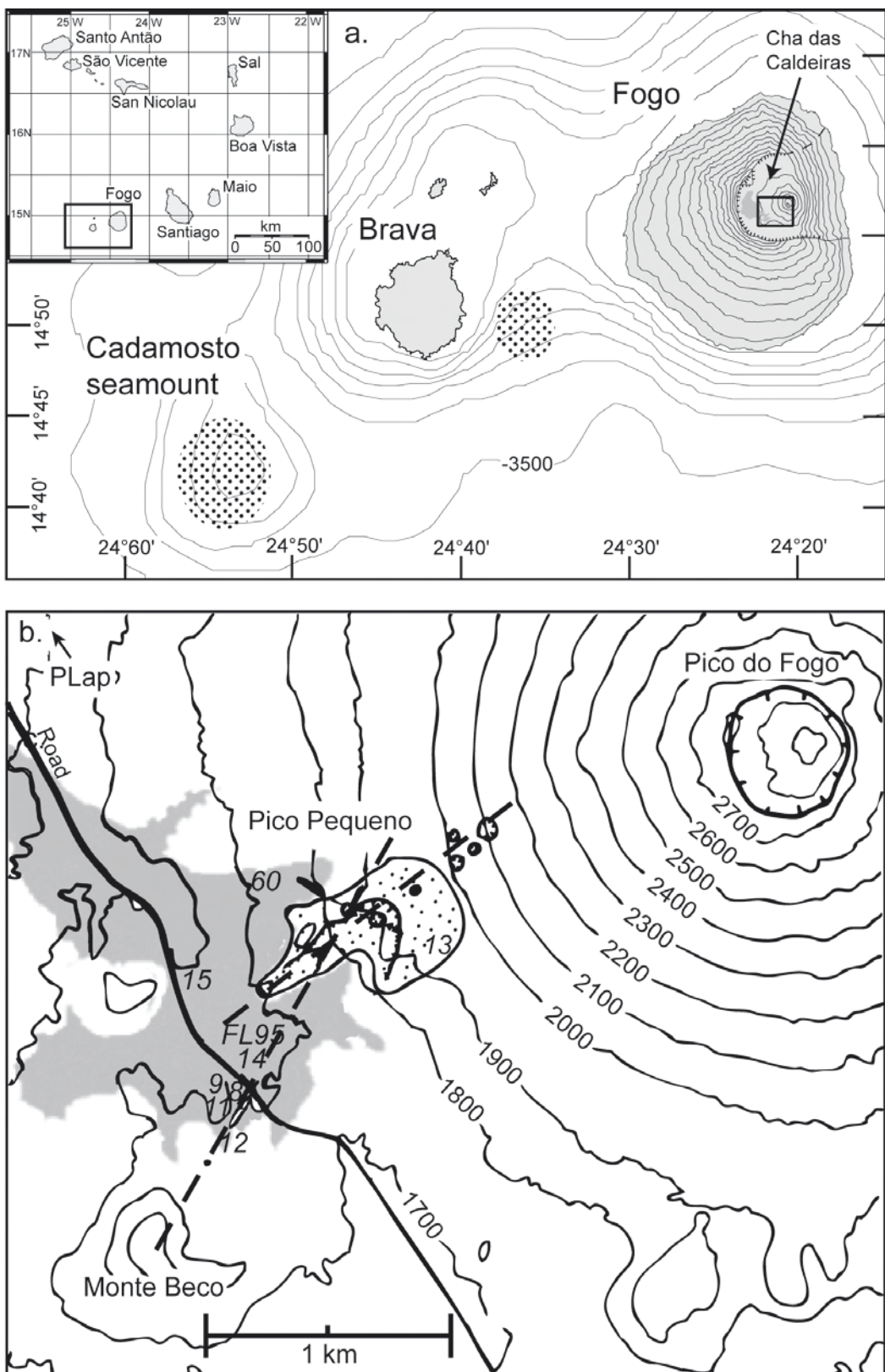


Fig. 1 **a** Location and overview map of the Cape Verde Islands (inset) and map of the Fogo-Brava platform with 500 m bathymetric contours and 200m topographic contours on Fogo. Dotted areas mark seismically active regions in the channel between Fogo and Brava (seismic crisis 1994) and at Cadamosto seamount (Heleno et al 1999; Grevemeyer et al. 2010). The rectangle shows the position of Fig. 1b. **b** Map of eruption centers and main fissures of the 1995 eruption showing the the syn-eruptive scoria cone of Pico Pequeno and sample localities with numbers (modified after Brum da Silveira et al. 1997). Grey shading: 1995 lava flows, dotted: scoria cones

2.2. Geological Setting

The Cape Verde Archipelago, located in the North Atlantic ~500-800 km west of the African coast, consists of nine major islands and several small islets forming the top of the Cape Verde Swell (Fig. 1a). All islands are of volcanic origin, related to the Cape Verde mantle plume, with broadly decreasing age progression from E to W along a northern and a southern chain (summarized in Holm et al. 2008). Magmatism involves dominantly silica-undersaturated melts with basanites-tephrites and nephelinites as the most important lithologies, but phonolites and/ or carbonatites also occur on several islands.

2.2.1. Geology of Fogo

Fogo has a diameter of ~25 km and reaches a maximum height of 2829 m above sea level at Pico do Fogo. According to Day et al. (1999) and Foeken et al. (2009), the evolution of Fogo can be subdivided into four phases: 1) The uplifted Seamount Series (~4.5 Ma) consists of carbonatites and alkaline basalts. 2) The first subaerial lavas of the Monte Barro Group, that lacks absolute age constraints, unconformably overlie the carbonatites. 3) The main phase of intense volcanism, the 2-3 km thick Monte Amarelo Group, consists mainly of highly alkaline basic to intermediate lavas and scoria cones. These rocks may be entirely of Quaternary age. The Monte Amarelo phase ended with a giant lateral collapse between 123-62 ka (Foeken et al. 2009), represented present-day by the up to 1 km high Bordeira cliff. 4) The post-collapse Cha das Caldeiras Group (62 ka to present) consists mainly of alkaline basanites to tephrites. This group includes a ~2 km thick sequence infilling the collapse scarp (Cha das Caldeiras plain) to where most historic eruptions were restricted, and the Pico do Fogo.

2.2.2. Chronology of the 1995 eruption

The eruption lasted from 2nd April to 26th May 1995 and was chemically and mineralogical zoned and bimodal in occurrence. In the first days of the eruption, tephriphonolitic to phonotephritic pyroclastics and lavas were discharged, followed by tephrites to basanites. For the sake of clarity, these groups will be referred to as phonotephrites and basanites throughout this paper. Detailed descriptions of the eruption chronology can be found in Réffega et al. (1997), Correia and Costa (1995),

and in the reports of the Smithsonian Institution (GVNB v. 20, no. 3; no. 4; no. 5; no. 11/12); it is briefly summarized here.

Initial Strombolian activity occurred along a 200 m long radial fissure at the SW flank of Pico do Fogo (Fig. 1b). Pyroclastics started to build up a scoria cone named Pico Pequeno. On April 3rd the fissure had extended to 2 km length, and the eruption style changed to Hawaiian with lava fountains up to 400m high feeding a lava flow that cut the main road to Portela village. Seven vents were active along the main fissure, which consisted of one ENE-WSW radial fracture at Pico do Fogo and a NNE-SSW oriented segment at Monte Beco (Fig. 1b) that became sealed gradually by an aa lava flow. In addition to the main aa lava flow several pahoehoe lobes formed during the first two days. Hawaiian lava fountaining at Pico Pequeno continued until April 17th, then Strombolian activity dominated until the end of the eruption. On April 23rd a new vent opened at the NW base of Pico Pequeno starting to erupt spatter and pahoehoe lava that spread over the earlier aa lavas. Volcanic activity continued with gradually decreasing effusion rates and short phases of intensified explosive action. At the end of the eruption on May 26th, an area of about 6.3 km² was covered by lava flows, and a total volume of about $54\text{-}68 \times 10^6$ m³ of volcanic material had been erupted (Torres et al. 1997).

2.2.3. Precursory and coeval seismicity

Seismic events related to the 1995 eruption are described in detail in Héleno da Silva et al. (1997; 1999) and Héleno (2003) and are summarized briefly herein. In January and February 1994 a small seismic crisis occurred in the surroundings of Brava. Initially the majority of earthquakes were located beneath the channel between Brava and Fogo, later on almost all events occurred beneath and W of Brava. The volcano-tectonic seismicity was interpreted to reflect magma movement. On Fogo itself a swarm of unlocated microearthquakes towards the SW of the islands and volcanic tremor within the Cha das Caldeiras collapse structure were observed (Héleno and Fonseca 1999).

From 25th March 1995 on, weak intermittent earthquakes were felt by the residents of Cha das Caldeiras. On 2nd April earthquakes became more frequent, and a stronger one in the evening was probably associated with the opening of the eruption fissure. Concomitant to the eruption, a weak volcanic tremor was felt on the floor of Cha das Caldeiras. On 10th April seismicity increased probably due to temporary obstruction of the vent and two microearthquakes probably related to a change in eruptive style

occurred on 12th April. Volcanic tremor remained moderate to strong until the end of the eruption, with episodes of increasing amplitude marking the larger events from 18th to 19th April when the eruptive style changed from dominantly Hawaiian to Strombolian. Immediately after the end of the eruption a swarm of seismic events occurred, interpreted as interaction between phreatic fluids and the retreating magma.

2.3. Petrography

We have investigated 11 samples of various eruption products covering the entire temporal and chemical variation of the eruption. Table 1 gives an overview of the sample localities and the major and trace element composition. Table 2 contains clinopyroxene data used for clinopyroxene-melt-thermobarometry. Additional chemical data of the 1995 and other Fogo eruptions are published by Munhá et al. (1997), Silva et al. (1997), Kokfelt (1998), Doucelance et al. (2003), and Escrig et al. (2005). Modal proportions were estimated visually by area in thin sections and hand specimen.

2.3.1. Early erupted phonotephrites

The phonotephrites consist of a glassy to microcrystalline matrix interspersed with 1-15 vol.% of phenocrysts and microphenocrysts ($\leq 3\text{mm}$). The major phenocryst phase is euhedral Ti-rich augitic clinopyroxene (up to 10 vol.%, Mg# 63.4-72.4; Mg# = molar Mg/(Mg+Fe)*100) followed by rounded kaersutitic amphibole (1-5 vol.%) and Ti-Mg-Al-rich magnetite (2-3 vol.%). Rare olivine and plagioclase are partly corroded and interpreted as xenocrysts. The groundmass consists of clinopyroxene and Ti-Mg-Al-rich magnetite with subordinate feldspar, melilite, and amphibole in varying amounts. Apatite occurs as columnar inclusions in clinopyroxene and amphibole phenocrysts.

2.3.2. Basanites

Basanites to tephrites of the 1995 eruption range in their normative olivine content from 7.0 to 13.6 % (using $\text{Fe}^{3+}/\text{Fe}^{2+} = 0.12$ based on analyses of Kokfelt (1998)). The samples consist of a glassy to microcrystalline groundmass interspersed with pheno-

Table 1 Major (wt%) and trace element (ppm) analyses of 1995 eruption products. * denotes trace elements analyzed by XRF, all others by ICP-MS. Mg# corresponds to a $\text{Fe}_2\text{O}_3/\text{FeO} = 0.3$ ($\text{Fe}^{2+}/\text{Fe} = 0.79$) based on the data of Kokfelt (1998)

Sample	Fogo 08	Fogo 09	Fogo 11	Fogo 12	Fogo 13	Fogo 15	Fogo 60	Flow 95	PicoLap95
Rock type	phonoteph	phonoteph	phonoteph	tephrite	tephrite	basanite	phonoteph	basanite	basanite
Description	lapilli	bomb	bomb	bomb	bomb	lava	lava	lava	lapilli
Chronology	early	early	early	early?	very late	late	early	middle	middle?
Lati (N)	14°56.19'	14°56.15'	14°56.15'	14°56.16'	14°56.58'	14°56.58'	14°56.84'	14°56.31'	14°57.62'
Long (W)	24°21.65'	24°21.70'	24°21.70'	24°21.65'	24°21.28'	24°21.80'	24°21.67'	24°21.54'	24°21.95'
<i>Major elements</i>									
SiO_2	46.72	48.91	48.82	42.34	42.86	43.11	47.76	42.37	42.97
TiO_2	2.52	2.05	2.07	3.58	3.55	3.50	2.24	3.69	3.35
Al_2O_3	18.67	19.73	19.65	15.88	15.53	15.75	19.14	15.12	15.08
$\text{Fe}_2\text{O}_3\text{t}$	8.91	7.92	7.93	12.68	13.04	12.85	8.68	13.63	13.11
MnO	0.23	0.20	0.20	0.22	0.19	0.19	0.20	0.19	0.20
MgO	2.59	2.37	2.40	5.20	6.09	5.97	2.79	6.61	6.86
CaO	8.34	7.00	7.00	11.56	11.59	11.26	7.69	11.90	10.45
Na_2O	6.44	6.50	6.46	4.49	4.09	4.12	6.22	3.75	3.95
K_2O	4.34	4.44	4.45	3.15	2.74	2.84	4.18	2.58	2.71
P_2O_5	0.64	0.57	0.57	1.09	0.97	0.96	0.68	0.95	1.06
H_2O	0.45	0.38	0.39	0.23	0.31	0.30	0.60	0.30	1.04
CO_2	0.05	0.04	0.05	0.05	0.04	0.04	0.08	0.05	0.18
Total	99.90	100.1	99.99	100.5	101.0	100.9	100.3	101.1	100.9
Mg#	40.39	41.09	41.36	48.87	52.12	51.99	42.83	53.06	54.95
<i>Trace elements</i>									
Li	16.76	16.67		10.43	8.97	9.06	14.61	8.58	10.20
Sc	4.29	3.92		16.99	26.07	23.74	4.96	28.01	18.58
V	257	184		365	371	358	202	391	332
Cr	0.7	4.0		16.4	82.4	63.8	7.0	88.8	41.1
Co	16.6	14.4		34.6	39.9	38.3	16.8	43.8	41.7
Ni	1.94	2.64		22.27	42.62	39.94	3.33	50.61	63.97
Cu	13.12	10.46		46.10	58.01	57.35	12.24	64.24	47.09
Zn	133	115		139	124	110	125	116	117
Ga	27.7	26.9		25.9	25.4	25.3	26.4	25.4	23.8
Rb	123.7	129.4		84.9	74.0	77.4	117.4	70.3	72.8
Sr*	1597	1409	1408	1277	1059	1095	1380	1009	1055
Y	37.7	30.9		37.3	31.2	31.4	31.1	31.4	31.1
Zr*	640	533	529	517	413	416	521	390	402
Nb	176	155		133	103	106	147	99	104
Cs	1.44	1.42		0.96	0.80	0.82	1.31	0.75	0.82
Ba*	1259	1214	1219	957	882	867	1196	771	835
La	92.6	85.8		75.0	63.1	65.0	83.9	60.5	64.1
Ce	183	165		159	133	135	164	129	135
Pr	20.4	17.9		19.0	15.8	15.9	18.2	15.5	16.1
Nd	74.3	63.2		72.2	60.3	60.7	65.7	60.4	61.4
Sm	13.5	11.2		14.6	12.6	12.2	11.9	12.3	12.2
Eu	4.09	3.44		4.33	3.70	3.69	3.67	3.66	3.74
Gd	11.07	9.19		12.09	10.14	10.40	9.44	10.36	10.49
Tb	1.45	1.19		1.53	1.29	1.30	1.29	1.32	1.29
Dy	8.08	6.66		8.12	6.84	6.80	7.33	7.08	6.80
Ho	1.48	1.19		1.48	1.19	1.19	1.25	1.22	1.20
Er	3.86	3.24		3.55	3.03	3.05	3.27	2.99	3.03
Tm	0.50	0.41		0.45	0.39	0.39	0.43	0.40	0.40
Yb	2.92	2.60		2.69	2.21	2.22	2.60	2.20	2.08
Lu	0.45	0.36		0.41	0.32	0.32	0.38	0.32	0.31
Hf	10.48	9.40		9.63	9.64	9.68	9.38	8.54	8.20
Ta	9.32	8.57		7.61	5.78	5.91	8.26	5.72	6.01
Pb	6.62	6.09		3.98	3.40	3.56	5.93	3.08	3.60
Th	8.26	8.66		5.41	4.81	5.05	8.15	4.47	4.86
U	2.09	2.15		1.34	1.13	1.17	2.01	1.05	1.13

crysts ($\leq 3\text{mm}$) and microphenocrysts of Ti-rich euhedral augitic clinopyroxene (~ 20 vol.%, Mg# 67.3-74.2), euhedral olivine (2-5 vol.%, Mg# 76.5-83.5), Ti-Mg-Al-rich magnetite (~ 5 vol.%) and kaersutitic amphibole (0-5 vol.%). Microlite phases are comprised of clinopyroxene, Ti-Mg-Al-rich magnetite, and subordinate melilite, plagioclase and olivine. Many clinopyroxene phenocrysts reveal hour-glass zonations or show articulate thin zonations at the outermost rims. A few clinopyroxenes contain older rounded cores of similar color to the rim zones; green cores are very rare. Some

clinopyroxene phenocrysts contain apatite inclusions. Sparse groundmass leucite was described for tephrites of 1995 by Munhá et al. (1997) but was not observed in the studied samples.

Xenoliths and xenocrysts are very rare in the products of the 1995 eruption and are restricted to a few small clasts of pyroxenites and pyroxene-hornblendites occurring predominantly in the late lavas.

2.3.3. Occurrence of fluid inclusions

CO₂-rich fluid inclusions occur in some clinopyroxene and olivine phenocrysts and are partly associated with melt inclusions. We investigated both primary inclusions occurring isolated or in randomly oriented groups that were incorporated during growth of phenocrysts, and trails of secondary and pseudosecondary inclusions incorporated in healed cracks (Roedder 1984) (Fig. 2). Secondary inclusions are more abundant than primary inclusions in the studied samples but intersections of secondary inclusion trails are rare. Most fluid inclusions are mature and spherical to oval or have the host crystal shape. The investigated inclusions are up to 21 µm in size with a majority around 2-6 µm. Products of secondary reactions between trapped fluid and the inclusion wall were not observed in any inclusion. A few large primary inclusions show textures of partial decrepitation such as small crystallographically oriented cracks or trails of micro-inclusions radiating from inclusions; these were not included in our analyses.

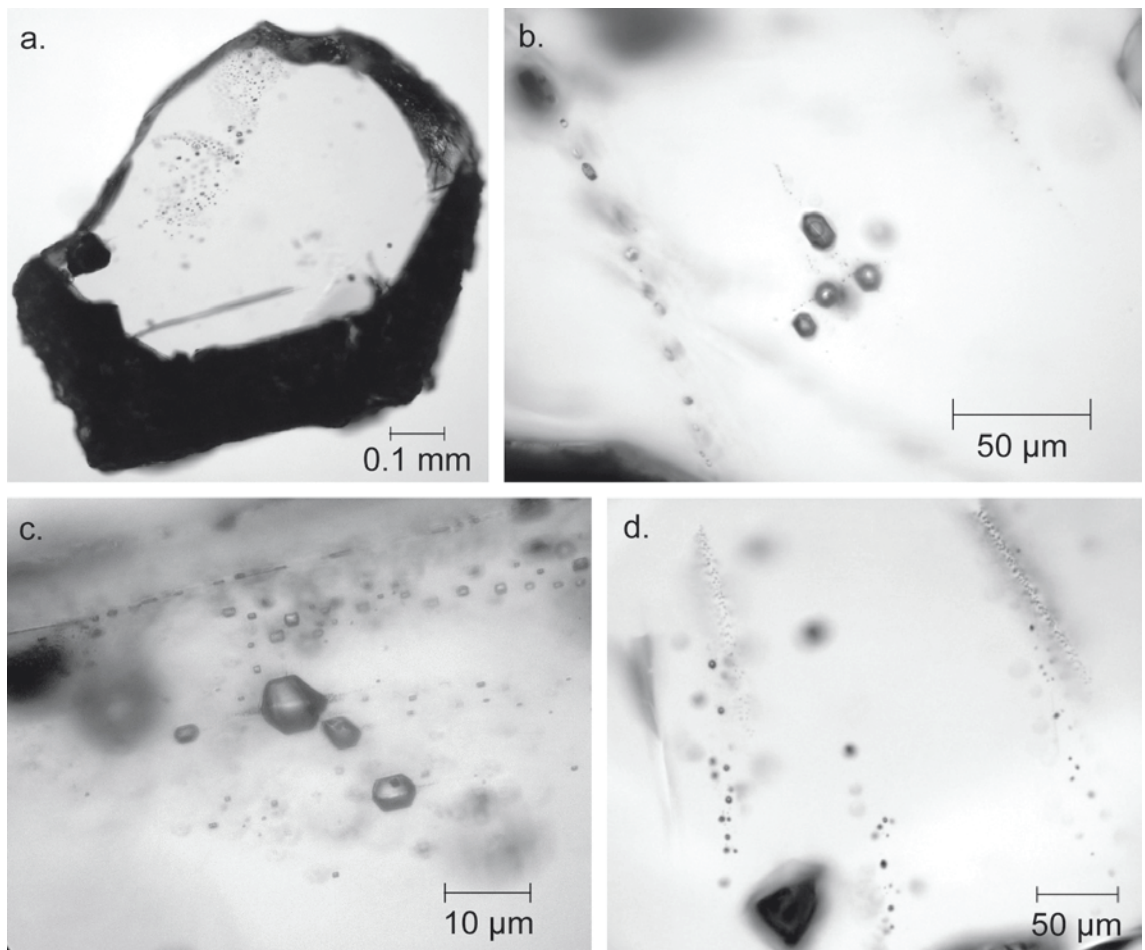


Fig. 2 Photomicrographs of fluid inclusions (FI) in phenocrysts. A. Olivine from a basanitic sample (Fogo 15) showing trails of secondary inclusions in the upper left part. B. Group of large primary FI in olivine of a basanitic sample (Fogo 13) with visible CO₂ bubbles and halos of minute inclusions resulting from decrepitation; these were not incorporated in our analyses. FI have negative crystal shape. Two trails of small melt inclusions crosscut the mineral. C. Group of primary FI in olivine of a phonotephritic sample (Fogo 11). The large FI in the center and the one to the lower right show traces of decrepitation. In the upper part of the photograph trails of small secondary FI and melt inclusions crosscut the mineral. D. Various trails of secondary FI crosscutting a clinopyroxene phenocryst (sample Fogo 09)

2.4. Analytical Methods

Fluid inclusions were examined in 100 µm thick doubly-polished sections of lavas and pyroclastics. Microthermometric measurements were carried out using a Linkam® THMSG 600 heating-cooling stage at the Department of Geosciences, University of Bremen, calibrated with SYNFLINC® synthetic fluid inclusion standards at -56.6 °C (triple point of CO₂) and 0.0 °C (H₂O). Precision of melting and homogenization temperatures as determined by repeated measurements of standards and samples is ± 0.2 °C or better. The standard data as well as some inclusions showing critical behavior at +31.1 °C indicate that the accuracy is also ± 0.2 °C. Densities of CO₂ inclusions were calculated using the auxiliary equations 3.14 and 3.15 of Span and Wagner (1996); the results closely match those obtained by the Angus et al. (1976) equations. Isochores and pressures were computed implementing the Stern and Pitzer (1994) equation of state (EOS) for the CO₂-H₂O system. This EOS yields pressures almost identical to the frequently used EOS by Kerrick and Jacobs (1981) for densities below 0.8 g/cm³, and performs better than the EOS by Holloway (1981) and Bottinga and Richet (1981) based on a smaller data set. See Hansteen and Klügel (2008) for a comparison of different equations of state for fluid inclusion barometry.

Major element analyses of minerals and glasses were performed with a JEOL JXA 8200 electron microprobe (EMP) at IFM-GEOMAR, Kiel. Analytical conditions included a focused beam with a current of 10-20 nA for mineral phases at an acceleration voltage of 15 kV. Glasses were analyzed with a defocused beam of 5-10 µm and a current of 10 nA. Analytical precision and accuracy were monitored by regular analysis of standard reference materials; see Table A1 in the electronic appendix. For diffusion calculations, semi-quantitative traverses across olivines were recorded with a focused beam of 100 nA, a spacing of 0.5 microns, and a dwell time of 1 s per point.

Whole rock analyses of major elements, Sr, Ba and Zr were performed at IFM-GEOMAR using a Philips X'Unique PW 1480 X-ray fluorescence spectrometer; H₂O and CO₂ were analyzed with a Rosemount CSA 5003 infrared spectrometer. All other trace elements were analyzed with a Thermo Finnigan Element2 ICP-MS at the Department of Geosciences, University of Bremen. See Duggen et al. (2009) for details on the analytical methods, and Tables A2 and A3 in the electronic appendix for analyses of standard reference materials accompanying the whole-rock analyses.

Sr-Nd-Pb isotope analyses (Table 4) were carried out at IFM-GEOMAR on 0.5-2 mm sized rock chips that were picked under a binocular microscope to eliminate visual signs of alteration. Depending on Sr-Nd-Pb concentrations, between 50 and 150 mg of sample chips were weighted into Savillex[©] Teflon beakers. To minimize the effects of sample handling the material was leached in ultra-pure 2N HCl at 70°C for one hour and subsequently rinsed three times in ELGA[©] water. The leached chips were then dissolved for 2 days in a 5:1 mixture of ultra-pure HF and HNO₃ at 150°C and ion exchange procedures followed established standard procedures (Hoernle et al. 2008). Isotope analyses were carried out in static multi-collection mode on a Finnigan MAT 262 RPQ2+ (Pb) and on a Thermo Finnigan TRITON-TI (Sr, Nd) thermal ionization mass spectrometer (TIMS). Sr and Nd isotopic ratios were normalized within run to ⁸⁶Sr/⁸⁸Sr = 0.1194 and ¹⁴⁶Nd/¹⁴⁴Nd = 0.7219 respectively and all errors are reported as 2 sigma of the mean. NBS987 measured along with the samples gave ⁸⁷Sr/⁸⁶Sr = 0.710239 ± 0.000014 (n=4) and was normalized to ⁸⁷Sr/⁸⁶Sr = 0.710250. During two subsequent Nd-sessions La Jolla measured along with the samples gave ¹⁴³Nd/¹⁴⁴Nd = 0.511849 ± 0.000008 (n=12) and ¹⁴³Nd/¹⁴⁴Nd = 0.511846 ± 0.000007 (n=12) and were normalized to ¹⁴³Nd/¹⁴⁴Nd = 0.511850. Although in this case the measured Sr and Nd standard values overlap with the normalized ratios, scaling to a fixed standard value ensures long-term comparability of Sr-Nd isotope data and therefore is a standard procedure of the IFM-GEOMAR lab. Pb isotope ratios were determined using the Pb double-spike (Pb-DS) technique. For details of the method see Hoernle et al. (accepted with minor revisions). Pb (DS) values for NBS 981 (n=30) and corresponding external 2sigma errors are ²⁰⁶Pb/²⁰⁴Pb= 16.9413 ± 0.0019, ²⁰⁷Pb/²⁰⁴Pb= 15.4995 ± 0.0019, ²⁰⁸Pb/²⁰⁴Pb= 36.7241 ± 0.0048, ²⁰⁷Pb/²⁰⁶Pb= 0.914891 ± 0.000037 and ²⁰⁸Pb/²⁰⁶Pb= 2.167719 ± 0.000074. Replicate analyses carried out as separate dissolution of sample “Brav 02” is within the errors of the standards.

Table 2 Compositions of clinopyroxene rims used for cpx-melt-thermobarometry. Each sample comprises the mean value of 5-20 analyzed points of one clinopyroxene phenocryst. P and T calculated after Putirka et al. (2003)

Sample_#	SiO ₂	TiO ₂	Al ₂ O ₃	FeO	MnO	MgO	CaO	Na ₂ O	Cr ₂ O ₃	Total	Mg#	P [MPa]	T [°C]
Basanites													
Flow95_01	41.46	4.51	10.80	8.24	0.13	10.94	22.31	0.44	0.01	98.8	70.3	530	1096
Flow95_12	42.36	4.73	10.96	8.01	0.14	10.85	22.27	0.45	0.01	99.8	70.7	540	1098
Flow95_15	41.15	4.75	11.63	8.14	0.11	10.63	22.32	0.45	0.01	99.2	70.0	550	1099
Flow95_16	42.99	4.04	9.90	7.85	0.13	11.41	22.29	0.45	0.01	99.1	72.2	520	1094
Flow95_17	42.42	4.36	10.72	7.93	0.12	11.18	22.31	0.43	0.01	99.5	71.5	510	1096
Flow95_18	44.28	3.82	9.70	7.73	0.15	11.49	22.21	0.46	0.01	99.9	72.6	540	1096
Flow95_19	44.66	3.62	8.83	7.68	0.12	12.13	22.43	0.40	0.00	99.9	73.8	460	1087
Flow95_22	41.57	4.63	11.11	8.32	0.12	10.78	22.18	0.46	0.01	99.2	69.8	560	1099
Flow95_23	43.94	3.48	9.33	7.50	0.11	11.98	22.59	0.42	0.02	99.4	74.0	490	1090
Flow95_26	43.79	3.84	9.79	7.77	0.12	11.71	22.40	0.44	0.01	99.9	72.9	510	1093
PLap95_15	43.51	3.79	9.54	7.84	0.14	11.66	22.46	0.45	0.01	99.4	72.6	520	1088
PLap95_21	41.89	4.42	10.78	8.29	0.13	10.90	22.33	0.47	0.00	99.2	70.1	550	1093
PLap95_27	42.82	4.08	9.94	8.06	0.15	11.30	22.44	0.44	0.00	99.2	71.4	510	1088
Fogo12_03	40.13	5.50	11.83	8.74	0.14	10.09	22.38	0.55	0.00	99.4	67.3	680	1083
Fogo12_07	43.41	3.90	9.68	7.69	0.13	11.60	22.83	0.47	0.01	99.7	72.9	580	1071
Fogo12_09	42.38	4.35	10.56	8.03	0.16	10.77	22.67	0.54	0.01	99.5	70.5	650	1078
Fogo12_10	40.52	5.03	11.57	8.63	0.15	10.26	22.42	0.54	0.00	99.2	67.9	670	1082
Fogo12_11	40.76	5.16	11.59	8.58	0.13	10.27	22.48	0.55	0.01	99.6	68.1	680	1083
Fogo12_12	42.67	4.25	10.35	8.16	0.16	10.87	22.68	0.53	0.01	99.7	70.4	640	1077
Fogo12_19	43.70	3.80	9.52	7.63	0.11	11.74	22.76	0.46	0.01	99.8	73.3	570	1070
Fogo12_20	42.21	4.44	10.46	8.36	0.17	10.99	22.61	0.49	0.00	99.8	70.1	610	1075
Fogo13_04	44.60	3.72	9.46	7.62	0.17	11.84	22.41	0.44	0.01	100.3	73.5	580	1118
Fogo13_06	43.56	4.01	10.27	7.72	0.12	11.43	22.52	0.45	0.01	100.1	72.5	600	1120
Fogo13_09	42.97	4.24	10.81	7.89	0.14	11.10	22.50	0.49	0.01	100.2	71.5	640	1124
Fogo13_10	43.34	4.16	10.46	7.81	0.14	11.45	22.42	0.48	0.00	100.3	72.3	620	1122
Fogo13_11	43.18	4.20	10.58	7.81	0.15	11.31	22.47	0.46	0.01	100.2	72.1	610	1122
Fogo13_13	43.13	4.21	10.49	7.85	0.12	11.46	22.53	0.45	0.01	100.3	72.2	590	1120
Fogo13_14	44.31	3.71	9.49	7.51	0.14	11.80	22.36	0.47	0.01	99.8	73.7	600	1119
Fogo13_15	44.46	3.87	9.61	7.58	0.16	11.76	22.45	0.45	0.01	100.3	73.4	590	1118
Fogo13_17	45.08	3.58	9.12	7.55	0.12	12.15	22.55	0.44	0.00	100.6	74.2	570	1116
Fogo13_18	42.36	4.48	11.29	7.96	0.13	10.92	22.47	0.49	0.00	100.1	71.0	640	1125
Fogo13_19	42.92	4.32	11.31	7.73	0.14	11.03	22.40	0.50	0.00	100.4	71.8	650	1127
Fogo13_20	44.91	3.56	9.68	7.62	0.16	11.84	22.51	0.48	0.01	100.8	73.5	610	1120
Fogo13_23	44.03	3.98	10.16	7.69	0.16	11.67	22.44	0.47	0.01	100.6	73.0	610	1121
Fogo13_24	43.21	4.27	10.82	7.84	0.15	11.31	22.49	0.48	0.01	100.6	72.0	630	1124
Fogo13_25	44.79	3.70	9.25	7.62	0.15	12.15	22.44	0.43	0.01	100.6	74.0	560	1116
Fogo13_26	43.04	4.27	10.85	7.82	0.14	11.29	22.45	0.47	0.01	100.4	72.0	620	1123
Fogo13_28	43.09	4.29	10.80	7.76	0.12	11.31	22.44	0.49	0.01	100.3	72.2	640	1124
Fogo13_29	43.20	4.00	10.37	7.71	0.14	11.46	22.63	0.46	0.01	100.0	72.6	610	1120
Fogo13_31	42.81	4.36	10.58	7.93	0.13	11.36	22.38	0.46	0.01	100.0	71.9	610	1122
Fogo13_33	42.35	4.39	11.21	7.66	0.12	11.00	22.50	0.49	0.00	99.8	71.9	640	1125
Fogo13_34	43.84	3.87	9.90	7.64	0.15	11.63	22.41	0.46	0.01	100.0	73.1	610	1120
Fogo13_35	43.83	3.73	9.30	7.54	0.15	11.76	22.61	0.46	0.01	99.4	73.5	590	1117
Fogo13_37	43.59	3.89	9.68	7.76	0.14	11.78	22.42	0.44	0.01	99.8	73.0	580	1118
Fogo14_04	41.94	4.66	11.16	8.14	0.11	10.77	22.55	0.45	0.01	99.8	73.7	540	1097
Fogo14_07	42.41	4.58	11.25	7.82	0.11	10.78	22.70	0.45	0.01	100.1	71.1	530	1097
Fogo15_01	43.07	4.03	10.24	7.67	0.14	11.19	22.21	0.47	0.00	99.0	72.2	620	1116
Fogo15_07	42.70	4.30	10.92	7.66	0.14	10.86	22.31	0.50	0.01	99.4	71.6	650	1119
Fogo15_10	42.87	4.23	10.20	7.87	0.13	11.19	22.12	0.45	0.00	99.1	71.7	600	1115
Fogo15_11	43.94	3.80	9.55	7.58	0.15	11.58	22.36	0.45	0.01	99.4	73.1	590	1112
Fogo15_12	43.25	4.08	9.97	7.72	0.14	11.31	22.46	0.46	0.01	99.4	72.3	600	1113
Fogo15_14	43.05	4.18	10.26	7.49	0.14	11.20	22.43	0.46	0.00	99.2	72.7	610	1114
Fogo15_16	43.02	4.25	10.58	7.56	0.15	11.05	22.33	0.48	0.01	99.5	72.3	630	1117
Fogo15_19	42.11	4.45	10.99	7.90	0.13	10.85	22.37	0.49	0.01	99.3	71.0	650	1119
Fogo15_21	44.37	3.67	9.34	7.52	0.15	11.67	22.46	0.44	0.01	99.7	73.4	580	1111
Fogo15_24	42.40	4.45	10.79	7.91	0.14	10.98	22.34	0.47	0.01	99.5	71.2	620	1117
Phonotephrites													
Fogo09_01	43.55	3.22	9.49	9.20	0.23	10.62	22.27	0.59	0.00	99.2	67.3	520	1013
Fogo09_02	43.39	3.39	9.82	8.81	0.21	10.46	22.48	0.60	0.00	99.2	67.9	520	1013
Fogo11_02	43.01	3.66	10.04	8.93	0.19	10.52	22.49	0.53	0.00	99.4	67.7	480	1011
Fogo11_03	43.24	3.63	9.89	8.60	0.18	10.77	22.58	0.55	0.01	99.5	69.1	490	1011
Fogo11_08	43.81	3.39	9.57	8.91	0.24	10.74	22.45	0.55	0.00	99.7	68.2	490	1011
Fogo11_10	42.75	3.78	10.09	9.02	0.22	10.44	22.45	0.56	0.01	99.4	67.4	500	1012
Fogo11_14	43.30	3.49	9.76	8.55	0.19	10.80	22.36	0.55	0.00	99.0	69.2	490	1011
Fogo60_01	44.69	3.33	8.92	7.93	0.15	11.69	22.42	0.51	0.01	99.7	72.4	450	1030
Fogo60_05	42.38	3.86	10.23	9.02	0.22	10.30	22.09	0.55	0.01	98.7	67.1	510	1037
Fogo60_07	42.67	3.91	10.14	8.88	0.16	10.70	22.13	0.55	0.01	99.2	68.2	510	1037

2.5. Results

2.5.1. Whole-rock geochemistry

Major and trace elements

Major and trace element data of whole rock analyses are reported in Table 1. Most bivariate plots reveal an articulate chemical bimodality between the early erupted phonotephrites and the later basanites (Fig. 3). Both rock groups have restricted major element compositions with e.g. Mg-contents ranging from 5.2 to 6.7 wt.% in the basanites, and from 2.4 to 2.8 wt.% in the phonotephrites. The basanites also contain more $\text{Fe}_2\text{O}_3(\text{t})$, TiO_2 , CaO and P_2O_5 , and less Al_2O_3 than the phonotephrites. The low concentrations of MgO , Ni (<64 ppm) and Cr (<89 ppm) of the most primitive rocks from the 1995 eruption clearly indicate that they represent not primitive magma but significant differentiation must have occurred at depth.

Trace element concentrations are similarly distinctive for the two rock groups. In phonotephrites, most incompatible elements (e.g. Sr , Ba , Zr , Rb , Nb , Pb , Th , U) are enriched compared to the basanites, whereas elements compatible in the observed phenocryst phases are depleted. The negative P and Ti anomalies in the phonotephrites most likely reflect removal of apatite and kaersutite + Ti-Mg-Al-rich magnetite, respectively (Fig. 4). Rare earth element (REE) patterns are roughly similar for both rock types, but phonotephrites have higher La/Sm and lower Sm/Lu than the basanites and a concave-upward REE pattern, consistent with kaersutite fractionation.

Least-squares mass balance calculations were performed in order to test whether basanites and phonotephrites are related by fractional crystallization. Various compositions of basanites and phonotephrites were chosen for the calculations, all pairs yielded similar results. The lowest sum of squared residuals (0.109) was achieved by fractionating olivine (1.2 wt.%), clinopyroxene (26.2 wt.%), kaersutite (11.8 wt.%), Ti-Mg-Al-rich magnetite (6.8 wt.%) and apatite (1.5 wt.%), which is consistent with our petrographic observations.

This model scenario of fractional crystallization was tested by calculating the concentrations of trace elements in the daughter melt and comparing them to the analyzed values. The calculations used partition coefficients compiled from the

GERM database and proportions of fractionated minerals from the mass balance calculations. The respective data and the results are shown in Table A4 in the electronic

appendix. Both batch- and Rayleigh-crystallization models yield good to excellent agreement between calculated and analyzed concentrations in the daughter melt for most trace elements. We thus conclude that the 1995 phonotephrites are derived from the 1995 basanites through crystal fractionation, but the possibility that both represent two distinct melt batches cannot be ruled out.

Table 3 Compositions of glasses used for clinopyroxene-melt thermobarometry determined by EMP and calculated (*) by crystal fractionation modeling of observed phenocryst phases

Melt	Used for	SiO ₂	TiO ₂	Al ₂ O ₃	FeO	MnO	MgO	CaO	Na ₂ O	K ₂ O	P ₂ O ₅	Total
<i>Tephrites /basanites</i>												
Flow95	Flow95, Fogo 14	44.92	3.31	18.08	10.50	0.24	3.80	9.84	5.02	3.43	1.24	100.38
PicoLap95	PicoLap95	45.83	2.94	18.38	9.55	0.24	3.68	9.18	5.17	3.60	1.23	99.79
Fogo 12*	Fogo 12	44.04	3.08	17.84	10.90	0.24	3.47	9.06	5.78	4.15	1.45	100.00
Fogo 13*	Fogo 13	44.22	3.30	17.06	10.91	0.20	4.38	10.54	4.89	3.32	1.18	100.00
Fogo 15*	Fogo 15	44.58	3.23	17.33	10.71	0.20	4.27	10.15	4.93	3.44	1.17	100.00
<i>Tephriphonolites</i>												
Fogo 11*	Fogo 11, 09	50.54	1.88	20.52	6.45	0.20	2.02	6.40	6.87	4.75	0.39	100.00
Fogo 60*	Fogo 60	49.40	2.06	19.97	7.23	0.20	2.42	7.14	6.62	4.46	0.50	100.00

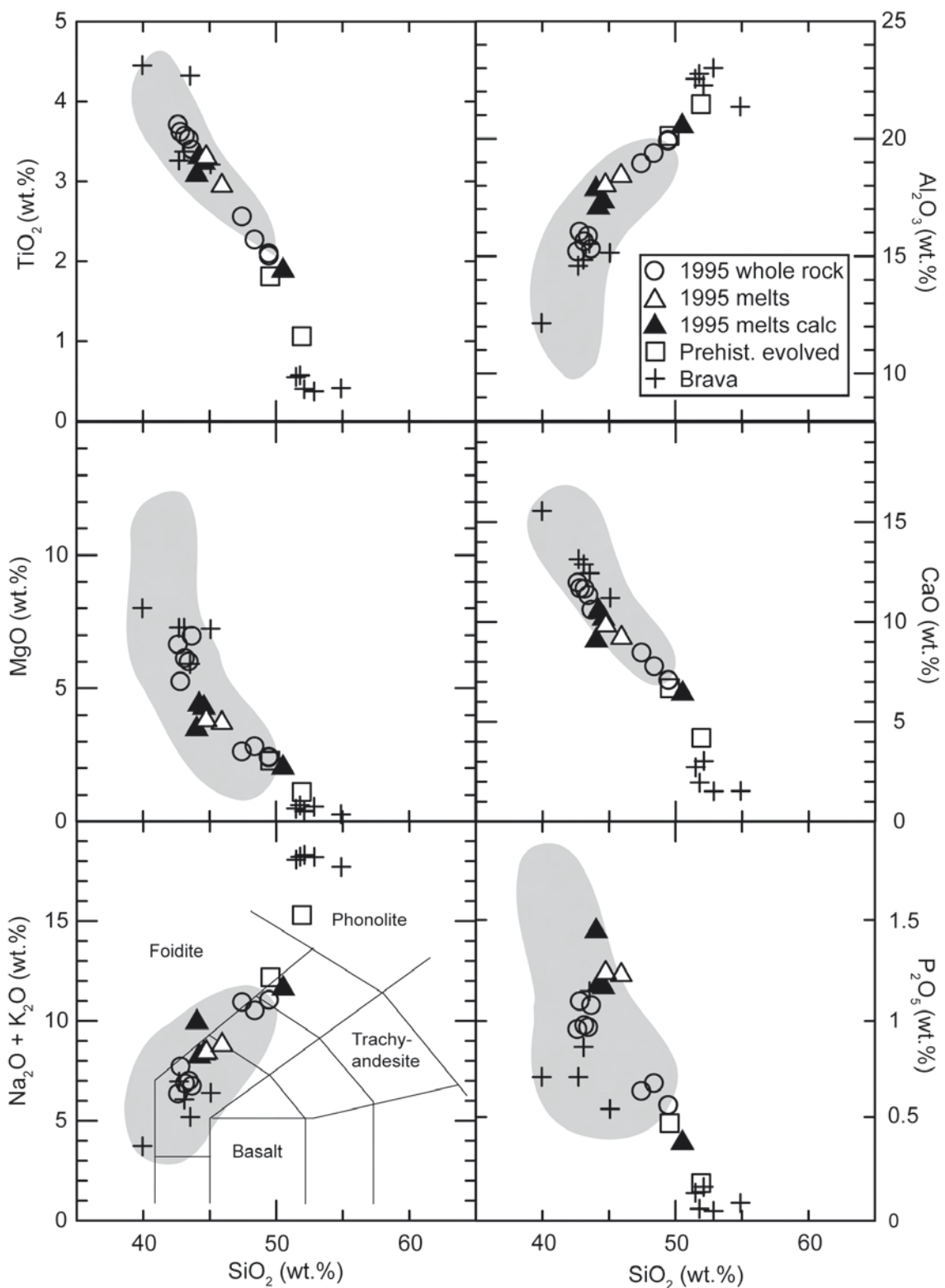


Fig. 3 Variations in major element compositions of samples from Fogo and Brava. Our data from the 1995 eruption are subdivided into whole rock analyses (Table 1), and analyzed glasses and calculated melts (Table 3). Data for prehistoric evolved rocks and Brava rocks are presented in Table A1 in the electronic appendix. Gray shaded fields indicate the range of published Fogo data from historic and prehistoric rocks (Munhá et al. 1997; Kokfelt 1998; Doucelance et al. 2003; Escrig et al. 2005)

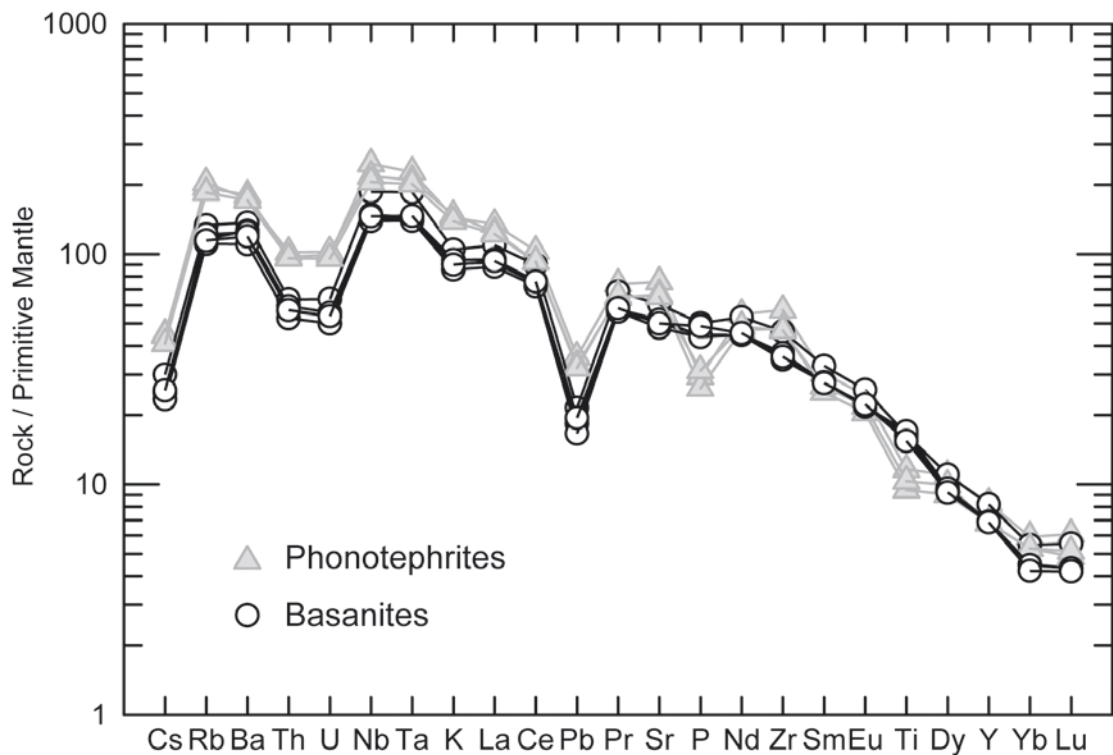


Fig. 4 Incompatible element diagram of investigated basanites and phonotephrites of the 1995 eruption, normalized to primitive mantle (Sun and McDonough 1989). Note the negative P and Ti anomalies of the phonotephrites reflecting apatite and amphibole fractionation, respectively

Isotopic compositions of Fogo and Brava rocks

Radiogenic isotopes are an essential tracer for revealing similarities and differences between the mantle sources of Fogo and Brava, and for testing the hypothesis that the evolved 1995 magmas were contaminated by Brava melts. Isotope data have been published for historic and prehistoric Fogo rocks (Kokfelt 1998; Doucelance et al. 2003; Escrig et al. 2005) but are lacking for Brava and for the rare evolved Fogo rocks. We have therefore determined the Sr-Nb-Pb isotope ratios of 12 samples from Brava (two basanites from the Lower Unit, three basanites and seven phonolites from the Upper Unit; for stratigraphic units see Madeira et al. 2010) and of two prehistoric evolved rocks from Fogo. The elemental concentrations of these samples are shown in Table A5 and in Fig. 3, the isotope data are listed in Table 4 and shown in Fig. 5.

The 1995 basanites and phonotephrites are isotopically alike and do not indicate contamination of the phonotephrites by isotopically distinct material. The isotope ratios of the two evolved Fogo samples are similar to each other and plot within the well-defined arrays of published Fogo data. They differ strongly from the narrow fields of the 1995 eruptives by having lower $^{87}\text{Sr}/^{86}\text{Sr}$ and higher $^{143}\text{Nd}/^{144}\text{Nd}$, $^{206}\text{Pb}/^{204}\text{Pb}$ and

$^{207}\text{Pb}/^{204}\text{Pb}$ ratios. The isotope ratios of the investigated Brava samples differ significantly from those of Fogo. The two Lower Unit samples show by far the lowest $^{87}\text{Sr}/^{86}\text{Sr}$ and the highest $^{143}\text{Nd}/^{144}\text{Nd}$, $^{206}\text{Pb}/^{204}\text{Pb}$, $^{207}\text{Pb}/^{204}\text{Pb}$ of the entire data set. The basanites and phonolites from the Upper Unit show $^{87}\text{Sr}/^{86}\text{Sr}$ ratios similar to Fogo rocks, but higher Nd and Pb ratios. Overall there is very little overlap between the fields for Fogo and for Brava rocks, which is indicative of distinct mantle sources and melting zones for both islands.

In summary, the combined isotope data show clearly that the 1995 basanites and phonotephrites show no affinity to phonolitic rocks from either Fogo or Brava (Fig. 5). This is a strong argument against a significant contribution of phonolitic melts from Brava to the evolved 1995 magmas. The isotope data are however consistent with the derivation of the 1995 phonotephrites from the basanites by crystal fractionation.

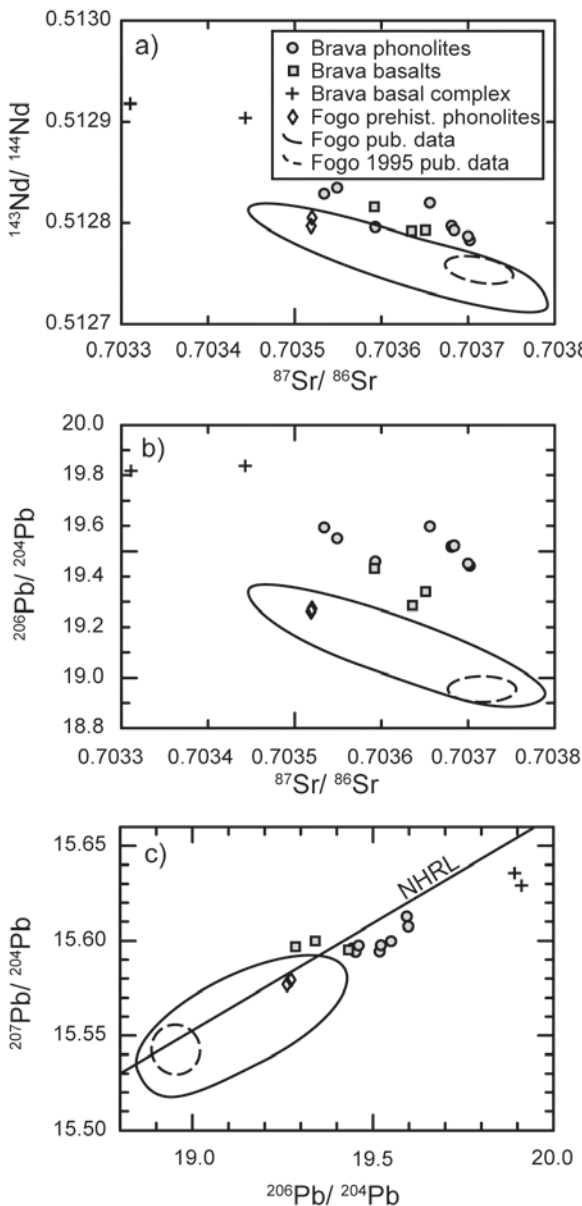


Fig. 5 Sr-Nd-Pb isotopic compositions of basaltic and phonolitic rocks from Brava and two prehistoric evolved rocks from Fogo compared to the array of published Fogo data from historic and prehistoric rocks (Kokfelt 1998; Doucelance et al. 2003; Escrig et al. 2005). The data indicate that the 1995 Fogo lavas cannot be derived by mixing of Fogo melts with Brava phonolites. Standard deviations (2σ) are smaller than symbol size. NHRL = Northern Hemisphere Reference Line (Hart 1984)

Table 4 Sr-Nd-Pb (DS) data of Brava and Fogo samples. Within run 2 sigma errors refer to last significant digits.

Sample	$^{87}\text{Sr}/^{86}\text{Sr}$	2σ	$^{143}\text{Nd}/^{144}\text{Nd}$	2σ	$^{206}\text{Pb}/^{204}\text{Pb}$	2σ	$^{207}\text{Pb}/^{204}\text{Pb}$	2σ	$^{208}\text{Pb}/^{204}\text{Pb}$	2σ	$^{207}\text{Pb}/^{206}\text{Pb}$	2σ	$^{208}\text{Pb}/^{206}\text{Pb}$	2σ
Brav 02	0.703681	(3)	0.512797	(3)	19.5186	(16)	15.5943	(14)	39.1923	(42)	0.79894	(2)	2.00794	(10)
Brav02*	0.703684	(2)	0.512793	(2)	19.5221	(15)	15.5977	(17)	39.2012	(55)	0.79898	(3)	2.00804	(14)
Brav 05	0.703549	(3)	0.512835	(3)	19.5502	(8)	15.5998	(7)	39.1934	(18)	0.79793	(1)	2.00476	(3)
Brav 06	0.703656	(3)	0.512820	(2)	19.5979	(6)	15.6075	(6)	39.1976	(17)	0.79638	(1)	2.00009	(4)
Brav 07	0.703534	(3)	0.512829	(5)	19.5936	(16)	15.6127	(12)	39.1799	(30)	0.79683	(2)	1.99963	(4)
Brav 08	0.703702	(2)	0.512783	(3)	19.4428	(13)	15.5960	(13)	39.1703	(44)	0.80215	(2)	2.01465	(10)
Brav 17	0.703443	(2)	0.512904	(3)	19.9111	(4)	15.6291	(3)	39.1722	(8)	0.78494	(1)	1.96736	(2)
Brav 18	0.703309	(3)	0.512918	(3)	19.8928	(11)	15.6357	(8)	39.1445	(19)	0.78600	(1)	1.96777	(4)
Brav 20	0.703592	(2)	0.512816	(3)	19.4324	(13)	15.5952	(15)	39.1146	(48)	0.80254	(2)	2.01286	(11)
Brav 21	0.703651	(2)	0.512793	(2)	19.3403	(8)	15.5999	(7)	39.0720	(20)	0.80660	(1)	2.02024	(5)
Brav 24	0.703636	(3)	0.512792	(3)	19.2857	(7)	15.5969	(6)	39.0176	(17)	0.80873	(1)	2.02314	(3)
Brav 25	0.703700	(3)	0.512787	(3)	19.4519	(11)	15.5941	(13)	39.1703	(42)	0.80168	(2)	2.01371	(11)
Brav 28	0.703593	(2)	0.512796	(2)	19.4605	(17)	15.5975	(14)	39.1139	(38)	0.80149	(2)	2.00991	(7)
Fogo 19	0.703520	(3)	0.512805	(2)	19.2729	(11)	15.5793	(12)	39.0146	(39)	0.80836	(2)	2.02432	(11)
Fogo 35	0.703519	(2)	0.512797	(3)	19.2624	(36)	15.5770	(39)	38.9995	(128)	0.80867	(7)	2.02464	(33)

2.5.2. Microthermometry of fluid inclusions

Fluid inclusion compositions

We analyzed fluid inclusions in olivine (142 primary, 77 secondary inclusions) and clinopyroxene (13 primary, 94 secondary) phenocrysts of three basanitic and two phonotephritic samples of the 1995 eruption. All observed fluids froze to aggregates of solid CO₂ and vapor during cooling between -80 and -100 °C. Further cooling to -190 °C did not generate other phase transitions. During reheating, melting of fluids occurred between -57.2 and -56.2 °C, close to the triple point of CO₂ (-56.6 °C) (Fig. 6). Initial (T_i) and final melting (T_m) coincided in almost all cases; only two inclusions in olivine showed a melting interval of 0.2 °C. Upon further heating all inclusions homogenized into the liquid phase below or at the critical point of pure CO₂ (31.1 °C).

These data indicate that all investigated fluid inclusions consist of nearly pure CO₂, because significant amounts of components other than CO₂ would have caused a lowering of T_i and a melting interval rather than a triple point (Andersen and Neumann 2001; Frezzotti et al. 2002). Even if minor amounts of other phases like N₂ or CH₄ are present these would not significantly affect the interpretation of the PT conditions during fluid trapping (van den Kerkhof 1990). No evidence for H₂O was found in any observed inclusion although it is expected as a component of volatiles exsolved from basaltic melts (Dixon 1997). Either former H₂O became lost by hydrogen diffusion after fluid trapping (Bakker and Jansen 1991; Hollister 1990; Mackwell and Kohlstedt 1990),

or it reacted with inclusion walls to form secondary minerals (Andersen and Neumann 2001; Frezzotti et al. 2002). No such reaction rims between fluid inclusions and host mineral could be observed, however.

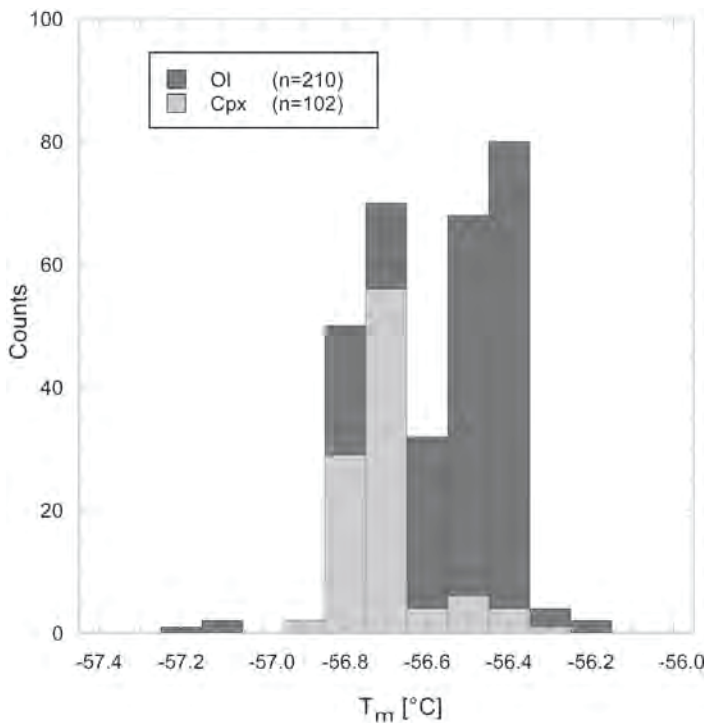


Fig. 6 Measured temperatures of final melting (T_m) of fluid inclusions in olivine and clinopyroxene phenocrysts indicate that most fluids are CO_2 -dominated. Temperatures significantly below the melting temperature of pure CO_2 (-56.6 °C) may indicate the minor presence of components such as N_2 or CH_4 in a few inclusions

Homogenization temperatures and densities of fluid inclusions

All inclusions homogenized into liquid CO_2 between 15.8 and 31.1 °C (Fig. 7a). Not a single inclusion homogenized into the vapor phase, although great care was taken to find such inclusions. Whereas different microthermometric behavior of primary and secondary inclusions was not recognized, inclusions in clinopyroxene have a clear tendency to higher homogenization temperatures, and hence lower densities, than inclusions in olivine. Similar observations were made for fluid inclusions in volcanic rocks from the Canary Islands and were assigned to olivine being less prone to re-equilibration than clinopyroxene (Hansteen et al. 1998; Galipp et al. 2006).

For the basanites, inclusions in olivine ($n=181$) homogenized between 20.6 and 30.3 °C corresponding to densities of 0.58-0.77 g/cm³, with a distinct frequency maximum at 0.64-0.76 g/cm³ based on 90% of the values (Fig. 7b). Inclusions in clinopyroxene ($n=2$) homogenized at 30.1 and 30.7 °C (0.544 and 0.591 g/cm³).

For the phonotephrites, inclusions in olivine ($n=38$) show homogenization temperatures from 15.8 to 27.3 °C corresponding to densities between 0.67 and 0.82 g/cm³, with a distinct frequency maximum at 0.75-0.81 g/cm³ based on 90% of the

values. Inclusions in clinopyroxenes ($n=104$) homogenized from 27.8-31.0 °C equivalent to densities of 0.51-0.66 g/cm³ with a frequency maximum between 0.52 and 0.61 g/cm³.

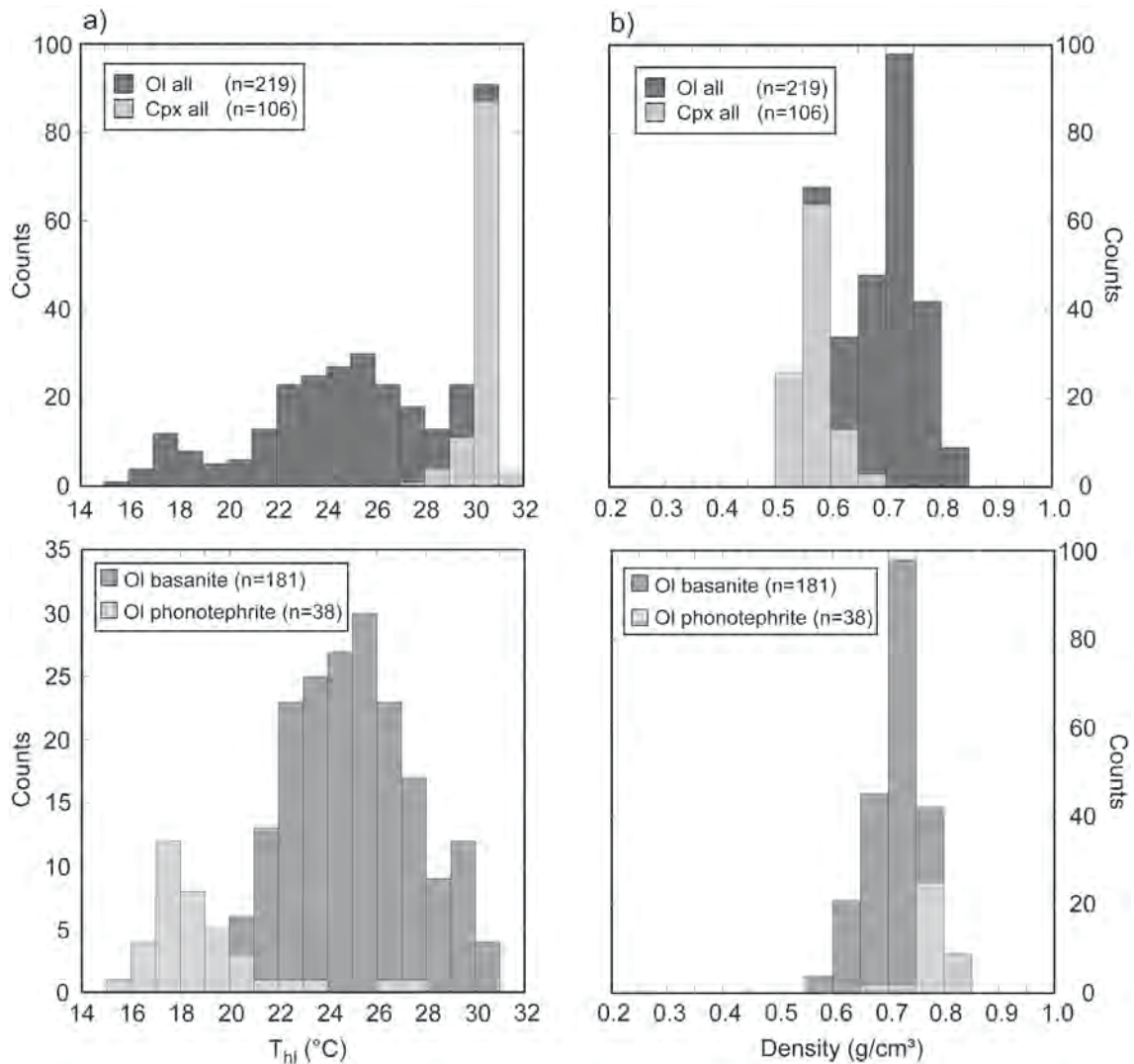


Fig. 7 **a** Measured homogenization temperatures T_{hl} and **b** calculated densities of CO₂-fluid inclusions in olivine and clinopyroxene phenocrysts in basanitic and phonotephritic samples. Upper panels (all inclusions) illustrate differences between olivine- and clinopyroxene-hosted inclusions; lower panels (only inclusions in olivine) illustrate differences between the two magma types. All inclusions homogenized into the liquid phase; n is the number of studied fluid inclusions

Calculated pressures

Pressures of formation or re-equilibration of fluid inclusions were derived from isochores, calculated using the equation of state for pure CO₂ of Stern and Pitzer (1994). Model temperatures of 1100 °C for basanites and 1030 °C for tephriphonolites were chosen based on the results of clinopyroxene-melt geothermobarometry (see

below). Temperature uncertainties have only minor influence on calculated pressures because of the moderately positive slopes of the calculated CO₂ isochores. For example, an uncertainty of ± 20 °C would transform into a pressure uncertainty of $\pm 5\text{--}8$ MPa.

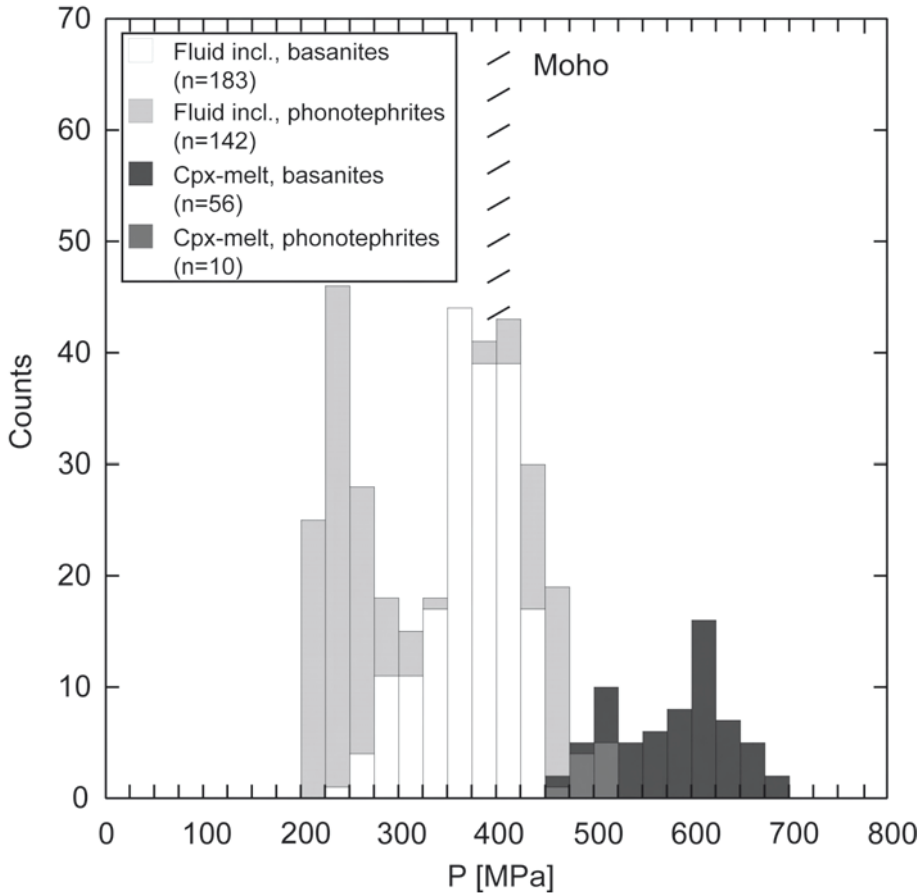


Fig. 8 Distribution of calculated pressures derived from fluid inclusion barometry in olivine and clinopyroxene phenocrysts and from clinopyroxene-melt barometry. Each data point of clinopyroxene-melt barometry corresponds to one clinopyroxene phenocryst. Pressure at Moho depth after the model of Pim et al. (2008)

Olivine-hosted fluid inclusions in basanites yield a range of 265–443 MPa with 90% of the data between 300 and 440 MPa, and those in phonotephrites cover a range of 323–471 MPa with 90% between 400 and 470 MPa. Inclusions in clinopyroxene in phonotephrites yield a range of 202–313 MPa with 90% of data between 220 and 310 MPa (Fig. 8). Despite considerable overlap, the fluid inclusion data show clearly that 1) clinopyroxenes yield significantly lower pressures than olivines in the same rock, and 2) the phonotephrites yield significantly higher pressures than the basanites. These observations place constraints on the interpretation of fluid inclusion data, as is discussed below.

2.5.3. Clinopyroxene-melt geothermobarometry

Temperatures and pressures of clinopyroxene crystallization were calculated by applying the clinopyroxene-melt geothermobarometer of Putirka et al. (2003), which is based on jadeite crystallization and jadeite-diopside + hedenbergite exchange equilibria. The thermobarometer is calibrated for a wide range of compositions, including hydrous and alkalic Si-undersaturated melts, and gave standard errors of estimate ± 33 K and ± 170 MPa for the regression data; a test data set between 0.1 and 4000 MPa gave a SEE of 130 MPa.

Clinopyroxene compositions (Table 2) were determined by analyzing and averaging 4-20 points at a distance of 5-10 μm to the rim of euhedral phenocrysts. Clinopyroxenes showing sector zonation were avoided. For samples Flow 95 and PicoLap95, matrix glass compositions were analyzed directly with the microprobe. For all other samples possessing microcrystalline or microlite-rich matrixes, melt compositions were calculated by a mass balance subtracting the observed amount of phenocrysts from the respective whole rock compositions (Table 3). This procedure is not critical to thermobarometry; for example, even a large relative error of 20 % for the subtracted phenocryst contents would transform into P and T errors of less than 5 % and 0.7 % for olivine, and 2 % and 1 % for clinopyroxene, respectively.

Except for sample Fogo 12, all calculated melt compositions fall on the liquid line of descent for recent Fogo rocks. The higher amount of alkalis in the Fogo 12 melt reflects the high alkali contents of the whole-rock in combination with an exceptionally large amount of clinopyroxene phenocrysts. In order to test for chemical equilibrium between calculated melt and clinopyroxene rim compositions, the following criteria were applied:

1) Test of Fe-Mg exchange equilibrium between clinopyroxene and melt. This test is not straightforward because $K_d = (X_{\text{Fe}^*}/X_{\text{Mg}})_{\text{Cpx}} / (X_{\text{Fe}^*}/X_{\text{Mg}})_{\text{liq}}$ was highly variable in the calibration data of the thermobarometer (Fe^* denotes total Fe). This is largely due to variable (in some cases not controlled) $f\text{O}_2$ and hence variable $\text{Fe}^{3+}/\text{Fe}^{2+}$ in the respective experiments. As suggested by Putirka et al. (2003), we used a constant K_d of 0.275 for the equilibrium test. Another test was made using the empirical relation of Duke (1976):

$$\log(X_{\text{Fe}^*}/X_{\text{Mg}})_{\text{Cpx}} = -0.564 + 0.755 * \log(X_{\text{Fe}^*}/X_{\text{Mg}})_{\text{liq}} \quad (1)$$

Clinopyroxenes with a discrepancy of $>5\%$ between the measured and both calculated Fe/Mg ratios were discarded (none in the basanites, 6 out of 16 in the phonotephrites).

2) Test of measured clinopyroxene components (DiHd, EnFs, Jd, CaTs) matching those predicted by the clinopyroxene saturation model of Putirka (1999) within the $\pm 2\sigma$ level, following Putirka et al. (2003). All clinopyroxenes in basanites match these criteria. All clinopyroxenes in phonotephrites show systematic deviations of $>2\sigma$ in the DiHd component but match the criteria for the EnFs, CaTs and the pressure-sensitive Jd components quite well (Fig. A1). The systematic discrepancy of the DiHd component may be due to the sparse calibration data of the Putirka (2003) calibration for evolved Si-undersaturated melts. We decided to include the phonotephritic clinopyroxenes in our data set and note that the calculated pressures overlap those obtained for the basanites. The calculated pressures and temperatures are carefully interpreted, however.

Calculated pressures and temperatures

Clinopyroxene rims from basanitic samples of the 1995 eruption yield a pressure range of 460-680 MPa with a frequency maximum around ~ 600 MPa, well above the values shown by CO₂ fluid inclusions (Fig. 8). Clinopyroxene from phonotephritic samples yield a smaller pressure range of 460-520 MPa thus overlapping with the basanite data. They also overlap with the highest pressures indicated by fluid inclusions in the same rock type. Because the pressure at the Moho depth near Fogo is around 400 MPa as based on a crustal model by Pim et al. (2008), all pressures indicated by clinopyroxene-melt barometry reflect uppermost mantle depths. Calculated temperatures yield a range of 1070 to 1127 °C for the basanites, and 1011 to 1037 °C for the phonotephrites (Fig. 9).

Model calculations show that the effect of analytical uncertainties is smaller than the prediction error of the thermobarometer and smaller than the overall data spread (Klügel et al. 2005). For the current data set, the pressure and temperature uncertainties due to analytical errors are estimated to be less than ± 50 MPa and $\pm 10^\circ\text{C}$ (2σ).

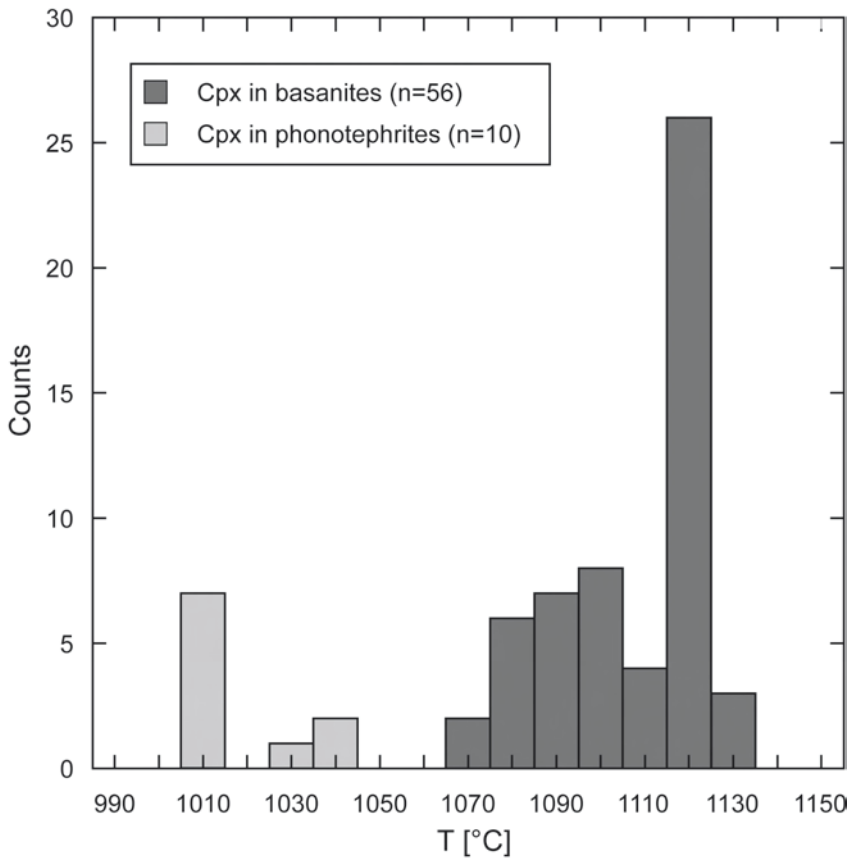


Fig. 9 Temperature distribution derived from clinopyroxene-melt equilibria in basanites and phonotephrites

2.5.4. Zonations of olivine phenocrysts

In order to place constraints on magma ascent dynamics during the eruption, we investigated the zonations of olivine phenocrysts by analyzing 36 semi-quantitative microprobe traverses across 25 euhedral crystals from two basanitic samples representing the main lava flow (Fogo 14) and the late pahoehoe unit (Fogo 15). In addition, a few quantitative profiles were analyzed to obtain accurate concentrations. All traverses were oriented perpendicular to the crystal rims in thin section; their exact orientation relative to the crystallographic axes was not determined.

Most olivines show simple normal zonations with a compositional plateau in the centers ($\text{Fo}_{81.5-82}$, 0.06-0.08 wt% NiO, 0.35-0.40 wt% CaO), and steep decrease in forsterite (Fo%) and NiO contents and increase in CaO near the rims. Some olivines are more complexly zoned, but reverse zonations are rare. The steep rim zonations indicate late-stage chemical disequilibrium between olivine and host melt, caused by an event of rapidly decreasing Mg# and NiO and increasing CaO of the melt. This compositional change can be modeled by fractional crystallization of 4-5 wt% of olivine +

clinopyroxene, and most plausibly reflects rapid microlite nucleation and crystal growth due to decompression-induced magma degassing and undercooling during final ascent (e.g. Sparks and Pinkerton 1978). Because the resulting growth zonations cause solid state diffusion in olivine, fitting of measured zonations by a pure diffusion model can yield upper limits for the actual times to produce them, which represent upper limits for the duration of final magma ascent to the surface (e.g. Klügel et al. 2000; Costa and Chakraborty 2004).

This being said, the simplest model for the rim zonations has the following initial and boundary conditions: olivines have an initially constant composition C_{core} ($t \leq 0, x \geq 0$) in equilibrium with the host melt, where t is time and x is the distance to the crystal-melt interface. At $t=0$ the host melt composition changes instantaneously to cause a different but constant rim concentration C_{rim} ($t \geq 0, x=0$). The resulting diffusion model is that of a semi-infinite half space with the solution

$$\frac{C - C_{rim}}{C_{core} - C_{rim}} = erf \frac{x}{2\sqrt{Dt}} \quad (2)$$

(Crank 1975). Most of the 46 analyzed Fo% zonations are well fitted by this simple equation, whereas the Ca zonations show larger scatter (owing to the low concentrations) and yield less satisfying fits. The semi-quantitative Ni data were too scattered as to be used for diffusion modeling. Profile lengths L were calculated from the error function fit as

$$L = 4\sqrt{Dt} \quad (3)$$

and range from 2.3 to 12.5 μm for Fo%, and 1 to 4 μm for Ca (Fig. 10).

Duration of profile formation

For calculating diffusion times we used a Fe-Mg interdiffusion coefficient $D_{FeMg} = 1.10 \times 10^{-16} \text{ m}^2/\text{s}$ following the master equations of Dohmen and Chakraborty (2007) with the following parameters: oxygen fugacity of the melt = $3.49 \times 10^{-5} \text{ Pa}$ (calculated after Kress and Carmichael (1991) using $\text{Fe}^{3+}/\text{Fe}^{2+} = 0.12$) temperature = 1100°C and pressure = 600 MPa based on the data presented above. For Ca diffusion we used $D_{Ca} = 7.84 \times 10^{-18} \text{ m}^2/\text{s}$ calculated after Coogan et al. (2005). Both D_{FeMg} and D_{Ca} were calculated for [001], the direction of fastest diffusion.

Calculated diffusion times range from 0.8 to 24.7 hours for Fo% and from 1.8 to 22.2 hours for Ca zonations (one single outlier ignored). The majority of both data sets is between 1 and 13 hours with a maximum frequency at 1-4 hours for Fo% and 3-7 hours for Ca (Fig. 10, Table A6). Remarkably, sample Fogo14 from the main lava flow yields shorter zoning profiles and hence shorter timescales (2.5-4.5 μm and 1.0-3.2 hours, respectively; $n = 9$) than sample Fogo15 from the late pahoehoe unit (up to 12.5 μm and 24.7 hours; $n = 34$). In addition to actual variations in diffusion times, much of the observed data spread is caused by the following effects not considered in the simple model:

1) Olivine has a strong diffusion anisotropy: $D_{\text{FeMg}}^{\text{a}} \approx D_{\text{FeMg}}^{\text{b}} \approx D_{\text{FeMg}}^{\text{c}} / 6$ and $D_{\text{Ca}}^{\text{a}} \approx D_{\text{Ca}}^{\text{b}} \approx D_{\text{Ca}}^{\text{c}} / 2$ (Dohmen and Chakraborty 2007; Coogan et al. 2005). As we consider only the [001] direction in our calculations, the diffusion times derived from Fe-Mg and Ca zonations can be underestimated by a factor of up to 6 and 2, respectively. To assess this effect we have calculated the distribution of zonation lengths for 5000 random directions by using eq. (3) for a fixed diffusion time and direction-dependent D_{FeMg} in olivine (e.g. Costa and Chakraborty 2004). The results show that diffusion anisotropy can partly account for variations at zoning profiles $< 6 \mu\text{m}$ long (diffusion times of 2-6 hours), but cannot explain the observed spread to longer profiles (Fig. 10a). For sample Fogo14, the measured data distribution is almost perfectly simulated by a diffusion time of 3.5 hours and random directions.

2) Geometric artifacts due to two-dimensional sectioning of samples and diffusive flux from the third dimension may result in significant overestimates of the diffusion time (e.g. Pan and Batiza 2002; Costa and Chakraborty 2004). In our study, however, both effects are probably of minor relevance because zoning profiles are short compared to the grain sizes and only olivines with similar core plateau compositions were used for the calculations.

3) Crystal growth concomitant to diffusion increases the length of zoning profiles and results in overestimates of the diffusion time. The magnitude of this effect may be large due to strong undercooling of the ascending and degassing magma, as is expressed by the large number of microlites in glassy 1995 samples. This effect could explain the tendency for Ca to yield larger diffusion times than Fo% zonations (Fig. 10b), because the weight of crystal growth relative to solid-state diffusion increases with decreasing diffusivities. This is also illustrated by a plot of measured Fo% versus Ca zonation

lengths, where short zonations tend to deviate from the diffusion field due to increased Ca lengths (Fig. 10c). In addition, the interpretation that growth dominated over diffusion at short Ca profiles is in accordance with their poor fit by the simple diffusion model.

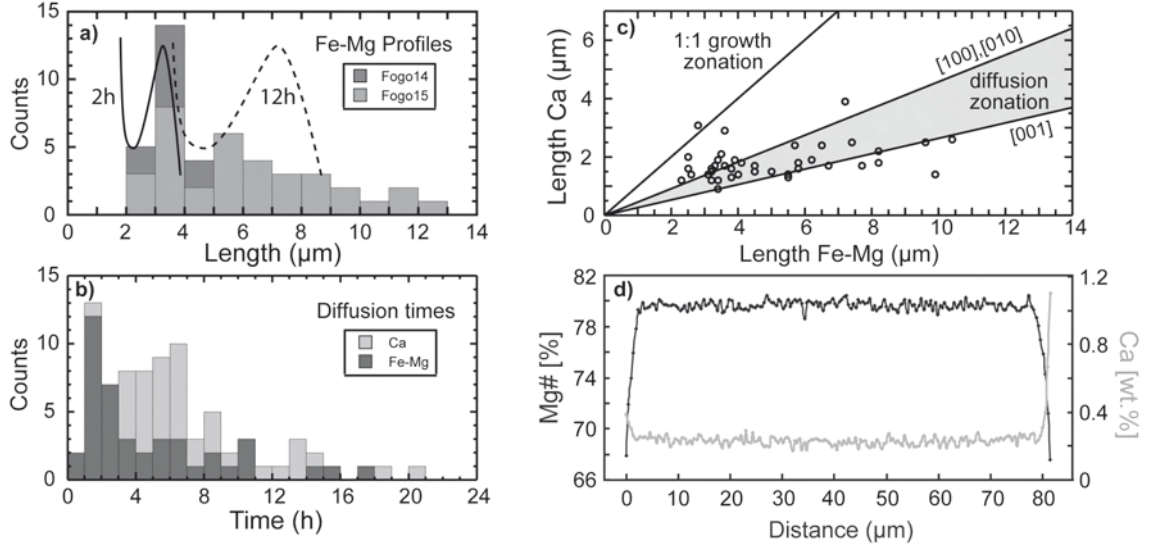


Fig. 10 **a** Calculated lengths for 46 Fo% zonation profiles at the outermost rims of olivine phenocrysts. Curves show distributions of simulated zonation lengths for 5000 randomly oriented crystals at diffusion times of 2 h (solid) and 12 h (dashed). **b** Diffusion times calculated for the outermost Fo% and Ca zonations using the diffusion coefficients for the [001] direction as discussed in the text. Average values are 5.9 h for Fo% and 7.8 h for Ca. **c** Comparison of profile lengths of Fo% and Ca zonations. Most data plot in the field for pure diffusional zonation that is limited by two straight lines with slopes of 0.27 and 0.46, i.e., the square root of the $D_{\text{Ca}}/D_{\text{FeMg}}$ ratios for the different directions. Data outside these limits reflect the effect of crystal growth and uncertainties in the determination of short Ca profile lengths. **d** Example of a zonation profile through an olivine phenocryst (sample Fogo 14_Ol_11)

Despite the effects discussed above and the large scatter for the Ca data, there is a remarkable overlap of diffusion times obtained for Fo% and Ca zonations, but the former yield more robust time constraints. In summary, by considering both anisotropy and crystal growth, our best estimate for actual diffusion times of sample Fogo14 is 1-3 hours. For sample Fogo15 the olivine population is more heterogeneous with respect to zoning profiles and we estimate an actual range of diffusion times of 2-12 hours. The major factors of uncertainty are believed to be the effect of crystal growth, and the proper choice of the strongly temperature-dependent diffusion coefficients.

2.6. Discussion

2.6.1. Interpretation of microthermometric data

Our microthermometric data for CO₂-dominated fluid inclusions in phenocrysts yield important pressure information, but the interpretation of the data set is not straightforward. An analysis of the frequency distributions of fluid densities (Fig. 7b) is necessary to place constraints on the conditions of entrapment and re-equilibration of the studied inclusions.

Re-equilibration can occur when changing ambient conditions lead to differences between inclusion fluid pressure and external pressure or change the host mineral composition. Three main types are distinguished here (reviewed by Bodnar 2003): a) Volumetric re-equilibration by stretching changes the inclusion volume and occurs by creep mechanisms (Wanamaker and Evans 1989). b) Re-equilibration by leakage (decrepitation) causes partial or complete loss of fluid. Inclusions showing signs of decrepitation were avoided in our investigations. c) Compositional re-equilibration cause diffusive loss of components from the trapped fluid (e.g. Bakker and Jansen 1991). This process can explain the virtual absence of H₂O in many CO₂-dominated inclusions. We note that in many cases it is not possible to recognize optically that re-equilibration had occurred. As a general rule, fluid inclusions yield minimum pressure estimates of magma stalling because all re-equilibration processes during magma ascent result in decreasing inclusion densities.

Observation 1: Olivine-hosted fluid inclusions show higher densities – and hence pressures - in phonotephrites (0.67-0.82 g/cm³, 320-470 MPa; n=38) than in basanites (0.58-0.77 g/cm³, 270-440 MPa; n=181). This appears counterintuitive because the phonotephrites were erupted before the basanites, and should have ascended from a similar or shallower depth. However, the different densities can be plausibly explained by different rates of re-equilibration of the inclusions during magma ascent to the surface. Stretching and diffusive loss of H₂O from the trapped fluid must have occurred because both processes occur at high rates that are strongly temperature-dependent. Even if olivine-hosted inclusions in both magma types had the same initial density distribution, a shift to lower densities upon rapid decompression would be larger for the basanites than for the significantly cooler phonotephrites. Because the temperatures for the phonotephrites inferred by clinopyroxene-melt thermometry are well below 1100

°C, the effect of stretching is small if they ascended to the surface in no more than a few hours (Wanamaker and Evans 1989). The limited effect of stretching is also reflected by the overlap of pressures obtained from olivine-hosted inclusions and clinopyroxene-melt barometry of phonotephrites (Fig. 8). With two different petrological approaches yielding similar pressures, this is a robust observation.

Observation 2: Fluid densities are higher in olivine-hosted than in clinopyroxene-hosted inclusions (Fig. 7b) even in the same rock type. This is most intriguing for the phonotephrites, where measured inclusion densities for clinopyroxene ($0.51\text{-}0.66 \text{ g/cm}^3$, 200-310 MPa; $n = 104$) and olivine ($0.67\text{-}0.82 \text{ g/cm}^3$, 320-470 MPa) phenocrysts show no overlap. The only plausible explanation for this observation are re-equilibration processes. Apparently, re-equilibration of fluid inclusions during magma ascent occurred faster and/or more complete in clinopyroxene than in olivine, in accordance with previous studies claiming that olivine is the better fluid container (Hansteen et al. 1998; Galipp et al. 2006). Clinopyroxene-hosted fluid inclusions may thus yield better approximations for the pressures of short-term re-equilibration.

Observation 3: The density distributions for clinopyroxene- and olivine-hosted inclusions are well-defined and show a sharp cut-off at 0.51 and 0.67 g/cm^3 (200 and 320 MPa), respectively. They are also not skewed towards lower densities, (Fig. 7b), in contrast to observed density distributions of fluid inclusions after gradual decompression and re-equilibration (e.g., Vityk and Bodnar 1998). The implications of this observation are two-fold. First, final magma ascent to the surface must have occurred in a short time (a few hours, see below) so that re-equilibration of inclusions was limited. Second, the data indicate two distinct levels of magma stagnation: a deeper level (400-470 MPa at least) that is mainly reflected by olivine-hosted inclusions, and a shallower level (around 220-300 MPa) where stagnation was long enough for most clinopyroxene-hosted inclusions to re-equilibrate, but not for olivine-hosted ones. Pressures between these levels are believed to reflect incomplete re-equilibration in most cases.

2.6.2. Depths of magma stagnation and fractionation

A distinctive feature of our barometric data is the very little overlap of calculated pressures for fluid inclusions (220-470 MPa) and for clinopyroxene-melt-equilibrium (460-680 MPa; Fig. 8). A similar tendency to lower pressures of fluid inclusion data has

been recognized in previous studies at different localities (Hansteen et al. 1998; Nikogosian et al. 2002; Schwarz et al. 2004; Galipp et al. 2006).

There are some possible causes for the distinct pressure ranges obtained by both barometric methods. 1) The model temperature used to obtain pressures from calculated isochores may be inappropriate. This is rather unlikely; because of the isochores' little $\Delta P/\Delta T$, the model temperatures would have to be unreasonably high (e.g., 1150 °C for the phonotephrite) for a complete overlap with the clinopyroxene-melt equilibrium data. 2) The barometer of Putirka et al. (2003) may yield inaccurate pressures for highly alkalic Si-undersaturated melts. This effect appears to be limited because of the wide range of melt compositions used for calibration and because calculated pressures for alkalic magmas are consistent with other observations (cf. Klügel et al. 2005). The systematic error of our calculated pressures is believed to be within 130 MPa (derived for a test data set; Putirka et al. 2003). 3) Compared to clinopyroxene-melt equilibria, fluid inclusions respond much faster, and by different mechanisms, to decompression during magma ascent. Volumetric or compositional re-equilibration of fluid inclusions at magmatic temperatures can occur during hours to days (summarized in Bodnar 2003; Hansteen and Klügel 2008), which is too short to be recorded by clinopyroxene equilibrating with a melt. For example, the growth of a 5-10 µm wide clinopyroxene rim at near-equilibrium conditions, or the diffusive re-equilibration along 5-10 µm (the distance used for the microprobe measurements), would require several months (Putirka 1997; Cashman 1990).

Taking together these considerations and the pressure distributions shown in Fig. 8, a consistent scenario arises. We interpret the pressure range of 460-680 MPa obtained by clinopyroxene-melt-thermobarometry as upper and lower bounds for the level where clinopyroxene and olivine phenocrysts crystallized before eruption, probably in a small magma reservoir. Corresponding depths are ~16-24 km, in the uppermost mantle just below the Moho (12-14 km depth; Pim et al. 2008; Lodge and Helffrich 2006). The weak tendency of the phonotephrites for lower pressures may reflect slightly shallower storage depth, or a bias due to the evolved melt composition, or the small number of data points. The pressures indicated by olivine-hosted fluid inclusions in phonotephrites (400-470 MPa) are fully consistent with the clinopyroxene-melt data when considering that some re-equilibration of inclusions must have occurred. A mere correction for a complete loss of e.g. 10 mole% of H₂O from the inclusions would shift the range to 400-620 MPa (cf. Hansteen and Klügel 2008).

The fluid inclusion data indicate the existence of a shallower level (around 220-310 MPa, 8-11 km depth) where the ascending magmas briefly stagnated before reaching the surface. Stagnation periods were probably on the order of a few hours to days, too short to be reflected by clinopyroxene-barometry but long enough for re-equilibration of fluid inclusions in clinopyroxene phenocrysts and, to a lesser degree, in olivine. This depth range is probably within the lower, intrusive oceanic crust (Pim et al. 2008); it may be closer to the Moho depth than indicated by the data if effects of re-equilibration are accounted for. The cause for ascending magmas to stagnate at this level is probably related to the density change at the Moho. We note that a similar depth range for magma ponding is inferred for the active Cumbre Vieja volcano on La Palma (Canary Islands), supported by the common occurrence of gabbro xenoliths from the lower crust (Klügel et al. 2005).

The third maximum around 340-460 MPa displayed in Fig. 8 is not interpreted as another stagnation level for ascending magmas, as this would require too much special pleading. This pressure range rather reflects the effect of incomplete re-equilibration of olivine-hosted inclusions as discussed above, although the former interpretation cannot be ruled out completely. It should be emphasized here that our data do not provide any evidence for shallow magma storage in the crust or within the volcanic edifice. Our clinopyroxene-melt barometry data support the inference by Amelung and Day (2002), based on InSAR data and a simple deformation model, that the 1995 magma chamber was located at >16.5 km depth. They also overlap partly with the rather large pressure range of 22-42 km estimated by Munhá et al. (1997) for wehrlite xenoliths. In contrast, the depth of origin of pyroxenite xenoliths obtained by these authors is significantly shallower (13 ± 3 km). This difference may indicate that the pyroxenites were not cognate to the 1995 eruption but represent cumulates from older magma batches that were picked up by the 1995 magmas. We note that this scenario is supported by our implication for a short-term stagnation level in the lower crust where remaining magma batches would ultimately form cumulates.

2.6.3. Constraints on magma ascent rates

The observed rim zonations of olivine phenocrysts are interpreted to reflect a short-term disequilibrium with the ascending host melt, caused by rapid decompression, degassing and crystal growth. Our best estimate for the duration of this disequilibrium is around 1-3 hours for sample Fogo14 and 2-12 hours for Fogo15 (Fig. 10), which allows

placing constraints on the ascent velocity of the magma. It is not known, however, at which depth the degassing-induced crystal growth initiated the diffusion clock. The fluid inclusions indicate that the magma was vapor-saturated at >440 MPa, thus an ascent from these depths inevitably causes degassing. During progressive depressurisation, degassing - and hence undercooling of the melt - strongly increases at <200 MPa due to the non-linear dependence of H₂O solubility on pressure (Dixon 1997).

We conclude that most of the olivine zonations formed during the final ascent from the stalling level in the lower crust (220 MPa or 8 km depth). In this case the average magma ascent rate would be on the order of 0.7-2.2 m/s for sample Fogo14 and 0.2-1.1 m/s for Fogo15. These are minimum values because diffusion had continued in the cooling lava flows for some time after eruption, and because the effect of crystal growth on the zoning profiles may have been underestimated. Interestingly, the sample from the main lava flow yields faster ascent rates than the sample from the late pahoehoe flow, which is consistent with decreasing activity towards the end of the eruption (Réffega et al. 1997).

Alternatively, if the diffusion clock were initiated when the magma began to ascend from the inferred reservoir in the mantle, the average ascent rates indicated by sample Fogo14 would range from 1.5-4.4 m/s (beginning at 16 km depth) to 2.2-6.7 m/s (beginning at 24 km). The duration of magma stagnation in the lower crust and re-equilibration of fluid inclusions would be limited to 1-3 hours, and peak ascent rates would be higher. Altogether we render this scenario as less likely.

2.6.4. Differentiation of the 1995 magmas

Even the most primitive basanites of the 1995 eruption are relatively differentiated with Ni contents of \leq 65 ppm and MgO <7 wt.%, which requires considerable olivine and clinopyroxene fractionation in mantle reservoirs. Although the basanites are inferred to be cogenetic with the earlier erupted phonotephrites, both are unlikely to have co-existed in a single zoned magma reservoir for a long period of time. Assuming H₂O contents of 1 wt.% in both magma types and temperatures of 1100°C and 1030°C, respectively, calculated viscosities range from 90 to 120 Pa s for the basanites and 1670 to 2590 Pa s for phonotephrites (Hui and Zhang 2007). Had the melts co-existed in a stratified magma chamber, these low viscosities and the large temperature difference would certainly have resulted in significant mixing and not in a bimodal suit of erupted

magmas as observed. We thus envisage a geometrically complex magma reservoir for the 1995 eruption with a small magma pocket having limited connection to the main chamber (Fig. 11). Such a geometry could result in a higher cooling rate of the small pocket resulted in a higher grade of crystal fractionation and formation of phonotephrite, and could inhibit convective mixing of the different melts. The magma ascent preceding the eruption started with the phonotephrite in the partially separated pocket and continued with the major magma batch of basanitic to tephritic composition. This model is consistent with the chemical and mineralogical zonation of the erupted lavas, with the little mixing of both melt types observed, and with similar pressure ranges for both magmas indicated by clinopyroxene-melt equilibria.

2.6.5. Is there a deep connection between Fogo and Brava?

The suggestion of a possible relation of the 1995 eruption to the magma plumbing system of Brava (Heleno 2003) was based on the unusual orientation of eruptive fissures, the unusual occurrence of evolved lavas, and the observed seismicity between both islands in 1994. This scenario, which would involve lateral magma movement at probably 2-7 km depth beneath the Fogo-Brava platform, is not supported by our combined petrological, geochemical and isotopic data. First, if lateral flow of magma had occurred at 2-7 km depth (~50-180 MPa) over considerable distances, this pressure should be reflected in some of the investigated fluid inclusions at least. Not a single inclusion, however, indicated a pressure less than 200 MPa despite careful study. Second, the major and trace element data indicate derivation of the 1995 phonotephrites from the basanites and rule out significant involvement of Brava material. Third, the isotopic fingerprints of recent Brava phonolites and basanites differ significantly from those of the 1995 Fogo eruption and other historic and prehistoric Fogo samples (Fig. 5) which indicates distinct regions of partial melting in the mantle for both islands.

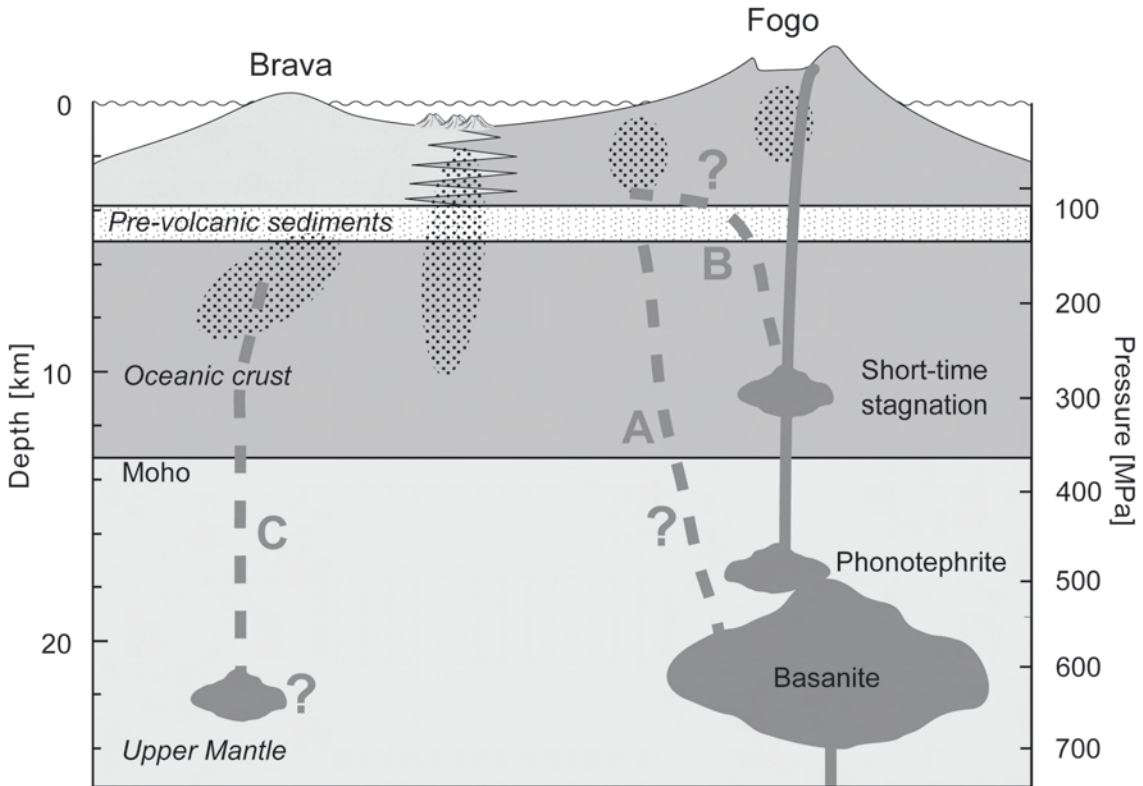


Fig. 11 Schematic model of the magma plumbing system of the 1995 Fogo eruption (thicknesses of crustal layers after Pim et al. (2008)). Fractional crystallization prior to eruption took place between 16 and 24 km depth in the uppermost lithospheric mantle. Early erupted phonotephrites are cogenetic with the subsequently erupted basanites and are interpreted to have evolved in a small pocket with limited connection to the main magma chamber. The ascending magma stalled briefly in the lower crust. Dotted areas mark the positions of hypocenters during the small seismic crisis of 1994 (Heleno da Silva et al. 1997; Heleno and Fonseca 1999), which may have been caused by propagating dikes preceding the 1995 eruption (dikes A and B) and/or dikes related to a plumbing system beneath Brava (C).

We thus conclude that magma ascent of the 1995 eruption occurred along the established magma plumbing system beneath Fogo without any interaction with the magma feeding system of Brava (Fig. 11). The evolved character of the zoned eruption appears to be fortuitous. Although our data suggest that short-term stagnation of ascending magma had occurred within the lower crust, possibly combined with some lateral movement, subhorizontal magma transport within the upper crust over larger distances can be ruled out. The SW-orientation of the 1995 eruptive fissures towards Brava merely reflects the local stress field near the surface. The feeder dike was found to be a planar, steeply NW-dipping sheet with a strike of ~60° that extended to a depth of 4 km at least (Heleno da Silva et al. 1999); there have been no indicators for lateral dike propagation from the SW prior to eruption. The seismic crisis below Brava and between the two islands in early 1994 was probably caused by one or more propagating dikes that did not reach the surface; possible interpretations are marked in Fig. 11.

Hypothetical dikes A and B are related to the magma batch that later fed the 1995 eruption, C is fed by a hypothetical reservoir below Brava and is independent from Fogo magmatism. The seismicity between Fogo and Brava was probably related to the morphologically young volcanic cones in this area (Le Bas et al. 2007), but so far nothing is known about the respective source.

2.7. Conclusions

1. Geochemical data and modeling of crystal fractionation shows that basanites and phonotephrites of the bimodal 1995 Fogo eruption are cogenetic. Differentiation of phonotephrites probably occurred in a smaller magma pocket with limited connection to the main magma chamber.
2. Clinopyroxene-melt barometry and fluid inclusion data provide insight into the magma plumbing system of the 1995 eruption. Before eruption the magma was stored within 460-680 MPa, corresponding to 16-24 km depth, in the uppermost mantle. During the eruption, the ascending magma stagnated for a short time at 220-310 MPa (8-11 km depth).
3. During the eruption the magma passed through the crust within less than twelve hours, probably 1-4 hours. Stagnation in the lower crust was restricted to periods of a few hours. Our data provide no evidence for prolonged magma storage at shallow levels (<200 MPa) or lateral magma movements within the Fogo-Brava platform.
4. Pre-eruptive seismicity on Brava and below the channel between Fogo and Brava in 1994 was probably caused by a propagating dike, which may have been related to the later 1995 eruption, or to a group of active submarine volcanoes in the channel.
5. Magma ascent of the 1995 eruption occurred along the established magma plumbing system of Fogo without interaction with the plumbing system near Brava. A seismic crisis in the channel between Brava and Fogo does not necessarily herald a new eruption on Fogo.

2.8. Acknowledgements

Our field work on Fogo would not have been possible without the support by Simon Day, Bruno Faria, José Antonio, and the Cape Verde Ministério do Ambiente e Agricultura / Parque Natural do Fogo. We thank Thor Hansteen, Sandra Heleno da Silva, Thomas Kokfelt, Ricardo Ramalho and Simon Day for stimulating discussions and help, and Mario Thöner and Heike Anders for analytical support. This study was supported by the Deutsche Forschungsgemeinschaft (DFG grants KL1313/9 and HA2100/12)

Electronic supplementary material

The electronic supplementary material of this paper is presented in the printed Appendix of the thesis (A1-A7).

2.9. References

- Amelung F, Day S (2002) InSAR observations of the 1995 Fogo, Cape Verde, eruption: implications for the effects of collapse events upon island volcanoes. *Geophys Res Lett* 29(12):GL013760
- Andersen T, Neumann E (2001) Fluid inclusions in mantle xenoliths. *Lithos* 55:301-320
- Angus S, Armstrong B, de Reuck K, Altunin V, Gadetskii O, Chapela G, Rowlinson J (1976) International Tables of Fluid State, Carbon dioxide, vol 3. Pergamon Press, Oxford, 1-385
- Bakker R, Jansen J (1991) Experimental post-entrapment water loss from synthetic CO₂-H₂O inclusions in natural quartz. *Geochim Cosmochim Acta* 55:2215-2230
- Barker AK, Holm PM, Peate DW, Baker JA (2009) Geochemical stratigraphy of submarine lavas (3-5 Ma) from the Flamengos Valley, Santiago, Southern Cape Verde Islands. *J Petrol* 50(1):169-193
- Bodnar RJ (2003) Re-equilibration of fluid inclusions. In: Samson I, Anderson A, and Marshall D (eds) *Fluid Inclusions: Analysis and Interpretation*. Mineral Assoc Can, Short Course Ser. 32:213-230
- Bottinga Y, Richet P (1981) High pressure and temperature equation of state and calculation of the thermodynamic properties of gaseous carbon dioxide. *Am J Sci* 281(5):615-660
- Brum da Silveira A, Madeira J, Serralheiro A, Torres P, Silva L, Mendes M (1997) O controlo estrutural da erupção de abril de 1995 na Ilha do Fogo, Cabo Verde. In: Réffega A et al. (eds) *A Erupção Vulcanica de 1995 na Ilha do Fogo, Cabo Verde*. Ministério da Ciencia e da Tecnologia; Instituto de Investigação Científica Tropical, Lisbon, pp 51-61
- Cashman KV (1990) Textural constraints on the kinetics of crystallization of igneous rocks. *Rev Mineral Geochem* 24(1):259-314
- Cashman KV (1990) Textural constraints on the kinetics of crystallization of igneous rocks. In: Nicholls J, Russell JK (ed) *Modern methods of igneous petrology: understanding magmatic processes*, Rev Mineral 24:259-314
- Chatterjee N, Bhattacharji S, Fein C (2005) Depth of alkalic magma reservoirs below Kolekole cinder cone, Southwest rift zone, East Maui, Hawaii. *J Volcanol Geotherm Res* 145:1-22
- Coogan L, Hain A, Stahl S, Chakraborty S (2005) Experimental determination of the diffusion coefficient for calcium in olivine between 900°C and 1500°C. *Geochim Cosmochim Acta* 69(14):3683-3694
- Correia E, Costa F (1995) Breve notícia da recente erupção na Ilha do Fogo e suas consequências. *Finisterra* XXX(59-60):165-175
- Costa F, Chakraborty S (2004) Decadal time gaps between mafic intrusion and silicic eruption obtained from chemical zoning patterns in olivine. *Earth Planet Sci Lett* 227(3-4):517-530
- Crank J (1975) *The mathematics of diffusion*. Oxford University Press, London, 1-414
- Day SJ, Heleno da Silva S, Fonseca J (1999) A past giant lateral collapse and present-day flank instability of Fogo, Cape Verde Islands. *J Volcanol Geotherm Res* 94:191-218
- Dixon JE (1997) Degassing of alkalic basalts. *American Mineralogist* 82:368-378
- Dohmen R, Chakraborty S (2007) Fe-Mg diffusion in olivine II: point defect chemistry, change of diffusion mechanisms and a model for calculation of diffusion coefficients in natural olivine. *Phys Chem Miner* 34:409-430
- Doucelance R, Escrig S, Moreira M, Gariepy C, Kurz M (2003) Pb-Sr-He isotope and trace element geochemistry of the Cape Verde Archipelago. *Geochim Cosmochim Acta* 67(19):3717-3733
- Duggen S, Hoernle KA, Hauff F, Klügel A, Bouabdellah M, Thirlwall M (2009) Flow of Canary mantle plume material through a subcontinental lithospheric corridor beneath Africa to the Mediterranean. *Geology* 37:283-286
- Duke J (1976) Distribution of the Period Four Transition Elements among Olivine, Calcic Clinopyroxene and Mafic Silicate Liquid: Experimental Results. *J Petrol* 17(4):499-521

- Escrig S, Doucelance R, Moreira M, Allègre C (2005) Os isotope systematics in Fogo Island: Evidence for lower continental crust fragments under the Cape Verde Southern Islands. *Chem Geol* 219:93-113
- Foeken J, Day S, Stuart F (2009) Cosmogenic ^{3}He exposure dating of the Quaternary basalts from Fogo, Cape Verdes: Implications for rift zone and magmatic reorganisation. *Quat Geochronol* 4:37-49
- Frezzotti M, Andersen T, Neumann E, Simonsen S (2002) Carbonatite melt- CO_2 fluid inclusions in mantle xenoliths from Tenerife, Canary Islands: a story of trapping, immiscibility and fluid-rock interaction in the upper mantle. *Lithos* 64:77-96
- Galipp K, Klügel A, Hansteen TH (2006) Changing depths of magma fractionation and stagnation during the evolution of an oceanic island volcano: La Palma (Canary Islands). *J Volcanol Geotherm Res* 155(3-4):285-306
- Garcia MO, Ho RA, Rhodes JM, Wolfe EW (1989) Petrologic constraints on rift-zone processes; results from episode 1 of the Puu Oo eruption of Kilauea Volcano, Hawaii. *Bull Volcanol* 52(2):81-96
- Geist D, White W, Naumann T, Reynolds R (1999) Illegitimate magmas of the Galápagos: Insights into mantle mixing and magma transport. *Geology* 27(12):1103-1106
- Grevemeyer I, Helffrich G, Faria B, Booth-Rea G, Schnabel M, Weinrebe W (2010) Seismic activity at Cadamosto seamount near Fogo Island, Cape Verdes - formation of a new ocean island? *Geophys J Int* 180:552-558
- Hansteen TH, Klügel A (2008) Fluid inclusion thermobarometry as a tracer for magmatic processes. In: Putirka K, Tepley III F (eds) Minerals, Inclusions and Volcanic Processes, *Rev Mineral* 69:142-177
- Hansteen TH, Klügel A, Schmincke H-U (1998) Multi-stage magma ascent beneath the Canary Islands: evidence from fluid inclusions. *Contrib Mineral Petrol* 132:48-64
- Hart SR (1984) A large-scale isotopic anomaly in the southern hemisphere mantle. *Nature* 309:753-757
- Heleno S (2003) O Vulcão do Fogo - Estudo Sismológico. Ph.D. thesis, Instituto Português de Apoio ao Desenvolvimento, Lisbon, pp 1-464
- Heleno SIN, Fonseca JFBD (1999) A seismological investigation of the Fogo Volcano, Cape Verde Islands: preliminary results. *Volc and Seis* 20:199-217
- Heleno da Silva S, Day SJ, Fonseca J (1999) Fogo Volcano, Cape Verde Islands: seismicity-derived constraints on the mechanism of the 1995 eruption. *J Volcanol Geotherm Res* 94:219-231
- Heleno da Silva S, Foulger G, Barros I, Querido A, Walker A, Fonseca J (1997) Seismic activity in Fogo and Brava Islands, Cape Verde. In: Réffega A et al. (eds) A Erupção Vulcânica de 1995 na Ilha do Fogo, Cabo Verde. Ministério da Ciencia e da Tecnologia; Instituto de Investigação Científica Tropical, Lisbon, pp 79-91
- Helffrich G, Heleno SIN, Faria B, Fonseca JFBD (2006) Hydroacoustic detection of volcanic ocean-island earthquakes. *Geophys J Int* 167:1529-1536
- Hoernle K, Tilton G (1991) Sr-Nd-Pb isotope date for Fuerteventura (Canary Islands) basal complex and subaerial volcanics: applications to magma genesis and evolution. *Schweiz Miner Petrog* 71:5-21
- Hoernle K, Abt DL, Fischer KM, Nichols H, Hauff F, Abers GA, van den Bogaard P, Heydolph K, Alvarado G, Protti M, Strauch W (2008) Arc-parallel flow in the mantle wedge beneath Costa Rica and Nicaragua. *Nature* 451:1094-1097
- Hoernle K, Hauff F, Kokfelt TF, Haase KM, Garbe-Schönberg D, Werner R, (2010) Interaction of a Weak Ascension Plume with the South Mid-Atlantic Ridge and Long-term Evolution of the Plume. *Earth Planet Sci Lett* (in review)
- Hollister L (1990) Enrichment of CO_2 in fluid inclusions in quartz by removal of H_2O during crystal-plastic deformation. *J Struct Geol* 12(7):895-901

- Holloway JR (1981) Volatile interactions in magmas. In: Newton R, Navrotsky A, Wood B (eds) *Thermodynamics of minerals and melts*. Springer, New York, pp 273-293
- Holm PM, Grandvoinet T, Friis J, Wilson R, Barker AK, Plesner S (2008) An 40Ar-39Ar study of the Cape Verde hot spot: Temporal evolution in a semistationary plate environment. *J Geophys Res* 113:B08201, doi:10.1029/2007JB005339
- Hui H, Zhang Y (2007) Toward a general viscosity equation for natural anhydrous and hydrous silicate melts. *Geochim Cosmochim Acta* 71(2):403-416
- Kerrick DM, Jacobs GK (1981) A modified Redlich-Kwong Equation for H_2O , CO_2 , and $\text{H}_2\text{O}-\text{CO}_2$ mixtures at elevated pressures and temperatures. *Am J Sci* 281(6):735-767
- Klügel A, Hansteen TH, Galipp K (2005) Magma storage and underplating beneath Cumbre Vieja volcano, La Palma (Canary Islands). *Earth Planet Sci Lett* 236:211-226
- Klügel A, Hoernle KA, Schmincke HU, White JDL (2000) The chemically zoned 1949 eruption on La Palma (Canary Islands): Petrologic evolution and magma supply dynamics of a rift-zone eruption. *J Geophys Res* 105(B3):5997-6016
- Kokfelt T (1998) A geochemical and isotopic study of the Island of Fogo, the Cape Verde Islands. PhD thesis. University of Copenhagen, pp 164
- Kress V, Carmichael I (1991) The compressibility of silicate liquids containing Fe_2O_3 and the effect of composition, temperature, oxygen fugacity and pressure on their redox state. *Contrib Mineral Petrol* 108:82-92
- Le Bas T, Masson D, Holtom R, Grevemeyer I (2007) Slope failures of the flanks of the southern Cape Verde Islands. In: Lykousis V, Sakellariou D, Locat J (eds) *Submarine mass movements and their consequences*. Springer, Berlin pp 337-345
- Lodge A, Helffrich G (2006) Depleted swell root beneath the Cape Verde Islands. *Geology* 34:449-452
- Mackwell SJ, Kohlstedt DL (1990) Diffusion of Hydrogen in olivine - implications for water in the mantle. *J Geophys Res-Solid* 95(B4):5079-5088
- Madeira J, Mata J, Mourão C, Brum da Silveira A, Martins S, Ramalho R, Hoffmann DL (2010) Volcano-stratigraphic and structural evolution of Brava Island (Cape Verde) based on 40Ar/39Ar, U-Th and field constraints. *Journal of Volcanology and Geothermal Research* 196(3-4):219-235
- Munhá J, Mendes M, Palácios T, Silva L, Torres P (1997) Petrologia e Geoquímica da Erupção de 1995 e de Outras Lavas Históricas na Ilha do Fogo, Cabo Verde. In: Réffega A et al. (eds) *A Erupção Vulcânica de 1995 na Ilha do Fogo, Cabo Verde*. Ministério da Ciencia e da Tecnologia, Instituto de Investigação Científica Tropical, Lisbon, pp 171-186
- Nikogosioan I, Elliott T, Touret J (2002) Melt evolution beneath thick lithosphere: a magmatic inclusion study of La Palma, Canary Islands. *Chem Geol* 183(169-193)
- Pan Y, Batiza R (2002) Mid-ocean ridge magma chamber processes: constraints from olivine zonation in lavas from the East Pacific Rise at $9^{\circ}30'\text{N}$ and $10^{\circ}30'\text{N}$. *J Geophys Res* 107: 10.1029/2001JB000435
- Peccerillo A, Frezzotti ML, De Astis G, Ventura G (2006) Modeling the magma plumbing system of Vulcano (Aeolian Islands, Italy) by integrated fluid-inclusion geobarometry, petrology, and geophysics. *Geology* 34:17-20
- Pim J, Peirce C, Watts A, Grevemeyer I, Krabbenhoft A (2008) Crustal structure and origin of the Cape Verde Rise. *Earth Planet Sci Lett* 272:422-428
- Putirka K (1997) Magma transport at Hawaii: Inferences based on igneous thermobarometry. *Geology* 25(1):69-72
- Putirka K (1999) Clinopyroxene + liquid equilibria to 100 kbar and 2450 K. *Contrib Mineral Petrol* 135:151-163

- Putirka K, Mikaelian H, Ryerson F, Shaw H (2003) New clinopyroxene-liquid thermobarometers for mafic, euvolcanic, and volatile-bearing lava compositions, with applications to lavas from Tibet and the Snake River Plain, Idaho. *American Mineralogist* 88:1542-1554
- Réffega A, Figueiredo M, Silva L, Costa F, Mendes M, Torres P, da Silva T, Correia E (1997) A Erupção Vulcânica de 1995 na Ilha do Fogo, Cabo Verde. Ministério da Ciencia e da Tecnologia, Instituto de Investigação Científica Tropical, Lisbon, p 422
- Rhodes JM, Wenz KP, Neal CA, Sparks JW, Lockwood JP (1989) Geochemical evidence for invasion of Kilauea's plumbing system by Mauna Loa magma. *Nature* 337(6204):257-260
- Roedder E (1984) Fluid Inclusions, *Rev Mineral* 12:644
- Schwarz S, Klügel A, Wohlgemuth-Ueberwasser C (2004) Melt extraction pathways and stagnation depths beneath the Madeira and Desertas rift zones (NE Atlantic) inferred from barometric studies. *Contrib Mineral Petrol* 147:228-240
- Silva L, Mendes M, Torres P, Palácios T, Munhá J (1997) Petrografia e Mineralogia das Formações Vulcanicas da Erupção da 1995 na Ilha do Fogo, Cabo Verde. In: Réffega A et al. (eds) A Erupção Vulcânica de 1995 na Ilha do Fogo, Cabo Verde. Ministério da Ciencia e da Tecnologia, Instituto de Investigação Científica Tropical, Lisbon, pp 165-170
- Span R, Wagner W (1996) A new equation of state for Carbon dioxide covering the fluid region from the Triple-point temperature to 1100 K at pressures up to 800 MPa. *J Phys Chem Ref Data* 25(6):1509-1596
- Sparks R, Pinkerton H (1978) Effect of degassing on rheology of basaltic lava. *Nature* 276(23):385-386
- Stern S, Pitzer K (1994) An equation of state for carbon dioxide valid from zero to extreme pressures. *Contrib Mineral Petrol* 117:362-374
- Stroncik NA, Klügel A, Hansteen TH (2009) The magmatic plumbing system beneath El Hierro (Canary Islands): constraints from phenocrysts and naturally quenched basaltic glasses in submarine rocks. *Contrib Mineral Petrol* 157:593-607
- Sun S-s, McDonough W (1989) Chemical and isotopic systematics of oceanic basalts: implications for mantle composition and processes. In: Saunders A, Norry M (eds) Magmatism in the Ocean Basins, Geological Society, London, Special Publications 42:313-345
- Torres P, Madeira J, Silva L, Brum da Silveira A, Serralheiro A, Mota Gomes A (1997) Carta Geológica das erupções históricas da Ilha do Fogo: Revisão e actualização. In: Réffega A, Figueiredo M, Silva L, Costa F, Mendes M, Torres P, da Silva T, Correia E (eds) A Erupção Vulcânica de 1995 na Ilha do Fogo, Cabo Verde. Ministério da Ciencia e da Tecnologia, Instituto de Investigação Científica Tropical, Lisbon, pp 119-132
- van den Kerkhof A (1990) Isochoric phase diagrams in the systems CO₂-CH₄ and CO₂-N₂: Application to fluid inclusions. *Geochim Cosmochim Acta* 54:621-629
- Vityk MO, Bodnar RJ (1998) Statistical microthermometry of synthetic fluid inclusions in quartz during decompression reequilibration. *Contrib Mineral Petrol* 132(2):149-162
- Wanamaker B, Evans B (1989) Mechanical re-equilibration of fluid inclusions in San Carlos olivine by power-law creep. *Contrib Mineral Petrol* 102:102-111
- Wolff J, Turbeville B (1985) Recent pyroclastic deposits on Brava, Cape Verde Islands. (abs). *Eos, Trans Amer Geophys Union* 66(46):1152

III

Barometry of lavas from the 1951 eruption of Fogo, Cape Verde Islands: implications for historic and prehistoric magma plumbing systems

Elliot Hildner¹, Andreas Klügel¹, Thor H. Hansteen²

¹Universität Bremen, Fachbereich Geowissenschaften, Bremen, Germany

²IFM-GEOMAR, Leibniz Institute of Marine Sciences, Germany

Submitted to Journal of Volcanology and Geothermal Research

Received: 29.07.2011



View from the Bordeira to the south showing numerous allying 1951 lava flows from several vents at the northwestern flank of Pico do Fogo

Abstract

Fogo is one of the most active oceanic volcanoes in the world. The island was affected by a prehistoric giant lateral collapse that cut off the summit of the former Monte Amarelo volcano. Subsequent volcanism has partly filled the collapse scar and built up the present-day Cha das Caldeiras plain and the Pico do Fogo stratovolcano. We have conducted a thermobarometric study of historic and prehistoric, basanitic to tephritic rocks in order to gain insight into the island's magma plumbing system and the impact of the collapse event on fractionation depths. A main focus was set onto the penultimate 1951 eruption, which produced basanites to tephrites (5.0 - 8.2 wt.% MgO) at two sites south and northwest of Pico do Fogo. Clinopyroxene-melt barometry of phenocrysts yields a well-confined pressure range of 480-650 MPa for the final crystallization level. Microthermometric data of CO₂-dominated fluid inclusions in olivine and clinopyroxene phenocrysts yield systematically lower pressures of 250-430 MPa. Inclusions in cumulate xenoliths yield pressures of 100-290 MPa. The combined data indicate pre-eruptive magma storage in the uppermost mantle between 17 and 22 km depth and syn-eruptive short-term magma stalling within the lower crust in 8-13 km depth. The lower pressures revealed by fluid inclusions in xenoliths may indicate that they originate from pre-1951 magma pulses that stalled and crystallized at variable levels in the crust. There is, however, no petrologic evidence for persistent crustal magma chambers. Clinopyroxene-melt barometric data of other historic and prehistoric eruptions indicate that magma storage and differentiation occurred in the uppermost mantle at pressures between 420 and 870 MPa (15-30 km depth) throughout the subaerial evolution of Fogo. Our data indicate that fractionation depths decreased significantly during a period of about 100 ka representing a strong growth phase of Fogo edifice leading up to the Monte Amarelo giant flank collapse at 123-62 ka. This trend seems to have been interrupted by the flank collapse, as early post-collapse magmas stagnated at deeper levels than late pre-collapse ones. Historic eruptions show shallower and broader pressure ranges, indicating an increase in complexity of the magma storage systems. Thus petrologic data indicate that flank collapse events may significantly influence deep-seated magma plumbing systems beneath ocean islands.

Keywords: Fogo, Cape Verde, thermobarometry, fluid inclusions, magma plumbing, flank collapse

3.1. Introduction

For our understanding of magmatic processes before and during volcanic eruptions, insights into the magma plumbing systems and the depths of magma storage and differentiation are essential. Besides geophysical observations of active volcanoes, petrologic investigations of erupted products are the main tool in gaining information about magma evolution and ascent dynamics. This approach has been carried out for various intra-plate oceanic island volcanoes. Hawaiian Islands in the shield-building stage commonly show major magma stagnation and differentiation in shallow summit reservoirs in 3-4 km depth that feed well-developed rift-zones by lateral magma transport (e.g. Garcia et al., 1989; Tilling and Dvorak, 1993). During sustained eruptions subsequent emptying of the conduit system below the summit reservoir was observed at Kilauea, indicating supplementary magma storage over a range of depths (~12-25 km) within the lithosphere (Putirka, 1997). Volcanoes of the Canary Islands and the Madeira Archipelago in their shield building stage commonly feature major magma fractionation at multiple levels within the lithospheric mantle in depth ranges of 12-45 km (Hansteen et al., 1998; Klügel et al., 2000; Schwarz et al., 2004; Galipp et al., 2006; Longpré et al., 2008; Stroncik et al., 2009). Short-term magma stagnation within the lower crust (8-10 km depth) during eruption has been demonstrated for Madeira archipelago and La Palma (Canary Islands), but seems to play only a subordinate role for magma differentiation (Schwarz et al., 2004; Galipp et al., 2006).

For La Palma a trend to shallower magma stagnation levels during the island's evolution was observed which may have been temporarily interrupted by a giant lateral collapse at 560 ka (Galipp et al., 2006). Large flank and summit collapses can dramatically affect the topography of volcanic edifices. Evidence for large destructive events especially on oceanic volcanic systems was found in various settings like Hawaii and Canary Islands (e.g. McGuire, 1996; Masson et al., 2002). Most studies have focused on possible mechanisms triggering large collapse events, which include magmatic intrusions, reactivation of basement faults, and hydrothermal alteration (e.g. Voight and Elsworth, 1997; Elsworth and Day, 1999; Vidal and Merle, 2000). In recent years studies dealing with impacts of collapse events onto the magma plumbing systems were conducted. A common observation is that large flank collapses were followed by preferred eruption of dense and crystal-rich lavas, which has been attributed to the

accompanying disturbance of the magma plumbing system (e.g. Presley et al., 1997; Longpré et al., 2009; Manconi et al., 2009).

On Fogo, the only Cape Verde island showing volcanic activity in historic time, a giant lateral collapse had occurred between 62 and 123 ka (Foeken et al., 2009). Amelung and Day (2002) postulated the existence of a shallow magma chamber that was removed by the collapse. However, nothing is known so far about the existence of persistent shallow magma chambers within the crust or the volcanic edifice during the evolution of Fogo, especially before the giant collapse event. Main goals of our study are therefore to verify the hypothesis of Amelung and Day (2002) and to shed light into the evolution of the magma plumbing system of Fogo and the influence of the collapse by studying several historic and prehistoric eruption products. Until now, only for the most recent 1995 eruption information of magma storage and differentiation depths are existent and disclose that this eruption was fed by a magma chamber in the uppermost mantle in 16-24 km depth (Munhá et al., 1997; Amelung and Day, 2002; Hildner et al., 2011). A major concern of this study is the penultimate Fogo eruption of 1951, that is well-documented but little investigated (Ribeiro, 1960; Day et al., 2000); few geochemical data can be found in Kokfelt (1998) and Escrig et al. (2005). The chronological sampling of almost all eruptive phases of 1951 allows a detailed comparison with the in many aspects distinct 1995 eruption. The north-south orientation of the 1951 eruption fissures is in accordance with those of previous historic eruptions, whereas the 1995 eruption fissure shows a southwest-northeast orientation (Day et al., 1999). The few published data of the 1951 eruption suggest chemical homogeneity, whereas the 1995 eruption was characterized by a distinctive bimodality in chemistry and mineralogy (Hildner et al. 2011).

In order to improve our knowledge about Fogo's magma plumbing system, we conducted a detailed barometric and geochemical study of prehistoric and historic eruption products with a focus on the penultimate 1951 eruption. The key points of this study are (1) to determine the depths of magma storage and differentiation of the 1951 eruption, (2) a well-grounded comparison of the magma histories of the in many kinds distinct 1951 and 1995 eruptions; (3) to gain insight into the temporal evolution of Fogo's magma plumbing system and the possible establishment of shallow crustal magma chambers and (4) the probable impacts of the giant lateral collapse. The results improve our knowledge of the magma plumbing system of this highly active and potentially hazardous volcanic island and therefore support the ongoing geophysical

monitoring. The methods of choice are clinopyroxene-melt thermobarometry, microthermometry of CO₂-dominated fluid inclusions in phenocrysts and xenoliths, and geochemical investigations.

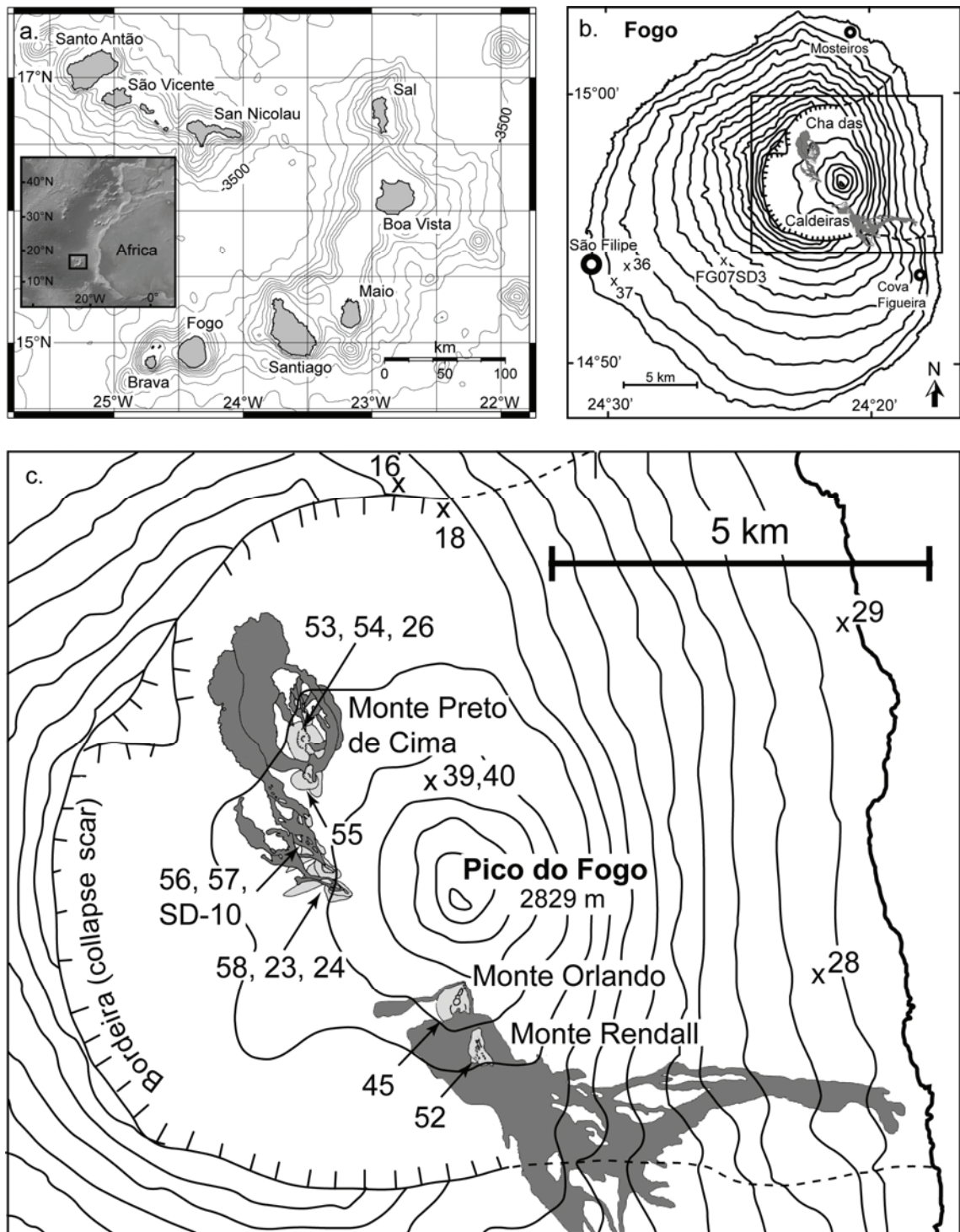


Fig. 1 **a** Location (inset) and overview map of the Cape Verde Islands with 500 m bathymetric contours. **b** Map of Fogo with 200 m topographic contours. Numbers mark sample localities, lavas of the 1951 eruption are plotted in gray, inset marks position of Fig. 1c. **c** Detailed map of the Cha das Caldeiras area, representing the infill of the Monte Amarelo collapse scar showing the spatter/ scoria cones (light gray) and lavas (dark gray) of the 1951 eruption and sample localities. 1951 lava flows and scoria cones are redrawn from Brum da Silveira et al. (1997) and Torres et al. (1997).

3.2. Geological Setting

The Cape Verde Islands are located in the North Atlantic, ~500-800 km west of the African coast between 15° and 17° N, and consist of nine inhabited islands and several islets (Fig. 1). They represent the top of the Cape Verde swell, the largest geoid and bathymetric seafloor anomaly on earth. All islands are of volcanic origin. The archipelago is associated with the Cape Verde mantle plume and shows a broadly decreasing age progression from east to west (summarized in Holm et al., 2008). Magmatism is dominated by silica-undersaturated alkaline melts of basanitic to tephritic composition, but phonolites and carbonatites also occur on some islands.

3.2.1. Geology of Fogo

Fogo is one of the most active volcanic islands in the world with almost 30 eruptions since 1500 AD. The island has a diameter of ~25 km and features a prominent horseshoe-shaped scar to the east formed by a prehistoric summit collapse. The scar was subsequently refilled by the present-day Cha das Caldeiras plain and Pico do Fogo volcano, the island's and the archipelago's highest elevation with 2829 m asl (Fig. 1). The geological evolution of Fogo can be subdivided into four distinct phases according to Day et al. (1999) and Foeken et al. (2009): 1.) the uplifted seamount series (~4.5 Ma) is composed of carbonatites and alkaline basalts. 2.) The Monte Barro Group includes the first subaerial lavas that unconformably overlie the carbonatites. So far there are no absolute age determinations for this group. 3.) The Monte Amarelo Group unconformably overlies the Monte Barro Group and formed after a period of cliff building. It represents a period of intense volcanism with deposits reaching a total thickness of 2-3 km. They consist mainly of highly alkaline basic to intermediate lavas and scoria cones, probably entirely of Quaternary age. The Monte Amarelo phase ended with the giant lateral Monte Amarelo summit collapse between 123 and 62 ka (Foeken et al., 2009), forming the present-day up to 1 km high Bordeira wall (Fig. 1c). 4.) The post-collapse Cha das Caldeiras Group (62 ka to present) is primarily represented by an up to 2 km thick sequence infilling the collapse scar (Cha das Cladeiras plain and Pico do Fogo) and by subordinate discontinuous lava sequences on the outer flanks of the island that are mainly of basanitic to tephritic composition.

3.2.2. Historic activity

Since the beginning of European settlement around ~1500 AD, the volcanic activity of Fogo was noticed. Around 30 historic eruptions are known, but for the first 300 years the descriptions are incomplete and imprecise. The most detailed work about Fogo and a summary of the historic volcanic activity is found in Ribeiro (1960) and contains an explicit description of the penultimate 1951 eruption. Until 1785 persistent and frequent volcanic activity was almost restricted to the Pico do Fogo summit itself, although periods of repose or relative quiescence seem to have prevailed from 1500 to 1564 and 1604 to 1662 (Day et al., 2000). The 1785 eruption was the only historic eruption with simultaneously active vents inside and outside the collapse scar, and the last one showing eruptive activity at the Pico summit. After 1785, the activity changed to predominantly N-S-oriented fissure-fed eruptions at the flanks of Pico, and the periods of repose became longer with an average of about 50 years.

The 1951 eruption started on June 12th and ended on August 21st. The erupted lava volume is $\sim 1.1 \times 10^7 \text{ m}^3$ (Global Volcanism Program, Smithsonian Institute). Activity began in the area south of Pico do Fogo building up the scoria cones of Monte Orlando and Monte Rendall (Fig. 1c), and due to northwestern propagation of the feeder dike, further vents opened west of Pico and finally at the pre-existing Monte Preto de Cima scoria cone during the first days of the eruption (Ribeiro, 1960; Torres et al., 1997; Day et al., 2000). The subsequent activity was limited to Monte Orlando and Monte Preto de Cima. When the activity of Monte Rendall ceased, the scoria cone became partly eroded by lava flows from Monte Orlando (Fig. 1c). The eruption was Strombolian to Hawaiian in style and fed several lava flows that destroyed parts of a village and cultivated area in Cha das Caldeiras. Especially in the very late phase of the eruption large amounts of xenoliths and amphibole megacrysts were erupted at Monte Preto de Cima.

The last eruption of Fogo lasted from April 2nd to May 26th 1995 and was fed by two fissures on the southwestern flank of Pico do Fogo. The eruption was chemically and mineralogically zoned with phonotephrites in the very first days followed by basanites to tephrites. The erupted lava volume is $2.9 \pm 0.7 \times 10^6 \text{ m}^3$ (Global Volcanism Program, Smithsonian Institution). Geochemical and geothermobarometric data are presented in Munhá et al. (1997), Kokfelt (1998), and Hildner et al. (2011).

3.3. Sampling and petrography

For our petrologic approach, we have taken samples of several historic and prehistoric eruptions within the Cha das Caldeiras area and the Bordeira wall, and from the eastern and western slopes of Fogo (Fig. 1b and c). An overview and chemical data of representative samples used in this study are given in Table 1. Ten lava samples (Fogo 23, 45, 52-58, FG01SD10) from various vents northwest and south of Pico do Fogo were taken in order to cover the whole temporal and geochemical range of the 1951 eruption. In addition, several ultramafic xenoliths and amphibole megacrysts (≤ 15 cm) of 1951 were sampled predominantly in late eruption products of Monte Preto de Cima. Further samples include two lavas from the 1785 AD eruption (Fogo 39+40), two lavas and one lapilli sample from the 1694 or other early post-1680 eruptions (Fogo 18, 28+29), one lava of early post-collapse age (FG07SD3, Monte Zambuda Member; Day personal communication 2007; Foeken et al., 2009), and two lavas and one lapilli sample of pre-collapse age (Fogo 16, 36, 37). The lava flow from which sample Fogo 37 was taken has been dated to 123 ± 5.2 ka (Foeken et al., 2009).

The porphyritic lavas of 1951 are predominantly tephrites with normative olivine contents of 6.8 to 9.9 wt.% (using $\text{Fe}^{3+}/\text{Fe}^{2+} = 0.25$ based on FeO and Fe_2O_3 analyses of Kokfelt, 1998). One sample (Fogo 52) is a basanite with 12.3 wt.% normative olivine. The phenocryst phases are euhedral Ti-rich clinopyroxene (5-30 vol.%), olivine (1-5 vol.%), Ti-Mg-Al-rich magnetite (1-5 vol.%) and kaersutitic amphibole (0-5 vol.%). Two samples contain ~ 1 vol.% of plagioclase. Various types of clinopyroxene occur with euhedral crystals with embayed or rounded cores and distinct rim zonations being most abundant. Hourglass zonations are common in all samples, whereas clinopyroxenes with green cores are very rare. Microcrystalline groundmass consists of clinopyroxene, magnetite, \pm olivine, \pm nepheline and \pm plagioclase.

Samples from older eruptions comprise lavas of basanitic, tephritic and foiditic whole-rock and/ or melt compositions (Tables 1 and 2). The two samples of the 1785 eruption (Fogo 39+40) contain 20-40 vol.% Ti-rich euhedral clinopyroxene and 20-30 vol.% olivine phenocrysts; the groundmass consists of fresh glass with varying amounts of microlites. Fogo 28 and 29 contain 20-40 vol.% clinopyroxene and 5-10 vol.% of magnetite but almost lack olivine. Microlite phases are clinopyroxene, magnetite, and subordinate amounts of amphibole. FG07SD3 is a foidite that contains ~ 30 vol.% clinopyroxene ~ 3 vol.% hauyne and $\sim 3\%$ magnetite phenocrysts. Fogo 16 is an

Table 1 Major (wt.%) and trace element (ppm) analyses of the studied rock samples. Major elements and trace elements denoted by * or italic values were analyzed by XRF, all others by ICP-MS. Mg# corresponds to a $\text{Fe}_2\text{O}_3/\text{FeO} = 0.25$ based on FeO and Fe_2O_3 analyses of Kokfelt (1998). sp. = spatter.

Sample	Fogo 23	Fogo 45	Fogo 52	Fogo 53	Fogo 54	Fogo 55	Fogo 56	Fogo 57	Flow 58	FG07SD3	Fogo 16	Fogo 37
Rock type	tephrite	tephrite	basanite	tephrite	tephrite	tephrite	tephrite	tephrite	tephrite	foideite	basanite	tephrite
Description	bomb	bomb	sp. bomb	sp. bomb	sp. bomb	sp. bomb	sp. bomb	sp. bomb	lava	lapilli	lava	
Chronology	1951 early N	1951 late S	1951 early S	1951 late N	1951 late N	1951 late N	1951 early N	1951 early N	early post-collapse	late pre-collapse	late pre-collapse	
Lati (N)	14°57.310'	14°55.742'	14°55.600'	14°58.418'	14°58.254'	14°58.101'	14°57.758'	14°57.612'	14°57.418'	14°53.950'	14°59.76'	14°53.32'
Long (W)	24°21.220'	24°20.664'	24°20.416'	24°21.506'	24°21.437'	24°21.457'	24°21.419'	24°21.425'	24°21.279'	24°24.769'	24°20.96'	24°29.18'
<i>Major elements</i>												
SiO_2	43.90	44.64	42.10	42.65	42.34	42.00	42.73	42.47	42.51	41.32	42.14	42.62
TiO_2	3.22	3.18	3.67	3.58	3.69	3.73	3.66	3.71	3.69	3.47	3.14	4.21
Al_2O_3	16.22	16.82	13.96	15.29	14.78	14.06	15.34	14.86	15.15	15.55	12.41	14.89
$\text{Fe}_2\text{O}_3\text{t}$	11.24	10.50	12.87	12.17	12.54	12.79	12.17	12.59	12.26	12.11	13.37	13.76
MnO	0.21	0.19	0.19	0.20	0.19	0.19	0.19	0.19	0.20	0.26	0.21	0.2
MgO	5.37	5.00	8.24	6.25	6.88	7.59	6.43	6.80	6.57	5.15	9.79	6.77
CaO	10.76	10.29	12.05	11.70	11.96	12.73	11.71	12.08	12.03	11.85	12.96	11.65
Na_2O	4.32	4.60	3.06	3.76	3.43	3.17	3.63	3.46	3.55	5.43	1.87	3.71
K_2O	2.95	3.23	2.22	2.59	2.43	2.20	2.57	2.46	2.50	3.2	1.08	2.65
P_2O_5	1.02	0.95	0.86	1.03	0.92	0.86	0.96	0.95	0.98	1.18	0.78	0.84
H_2O	0.16	0.22	0.31	0.23	0.17	0.15	0.21	0.26	0.17	0.46	2.18	0.25
CO_2	0.03	0.04	0.03	0.08	0.05	0.03	0.04	0.06	0.05	n.a.	n.a.	n.a.
Total	99.40	99.66	99.56	99.53	99.38	99.50	99.64	99.89	99.66	99.98	99.92	101.55
Mg#	51.60	51.50	58.80	53.40	55.00	56.90	54.10	54.40	51.30	64.60	54.90	
<i>Trace elements</i>												
Li	9.87	10.23	7.00	8.80	8.91	7.72	8.62	7.94	8.19	n.a.	n.a.	n.a.
Sc	17.21	16.73	32.94	21.98	29.73	33.66	24.33	27.88	25.41	29	29	32
V	314.1	307.2	393.9	362.4	408.1	410.2	372.7	385.6	375.9	300	290	336
Cr	56.1	24.9	150.3	74.5	111.2	160.2	86.3	91.4	73.7	12	397	75
Co	34.30	32.20	50.08	41.24	46.70	48.71	42.66	43.50	41.99	35	53	48
Ni	28.33	25.26	79.44	40.26	59.11	74.29	41.76	52.18	42.01	36	160	64
Cu	45.18	59.68	71.03	55.13	70.15	82.87	61.30	67.71	56.77	50	77	83
Zn	116.73	111.09	114.06	115.13	120.28	110.59	114.44	117.13	111.55	144	93	114
Ga	25.18	25.36	23.78	25.15	25.99	24.49	25.17	24.71	25.08	21	12	19
Rb	77.54	86.56	57.40	67.00	66.39	57.44	66.20	63.82	64.27	92	25	50
Sr*	1143	1233	897	1083	1003	911	1071	1010	1054	1545	878	970
Y	31.99	31.22	28.72	32.13	31.53	29.39	31.41	30.51	31.50	44	27	24
Zr*	432	450	344	402	379	359	403	389	401	499	232	391
Nb	109.59	114.18	84.09	99.32	97.33	83.74	97.44	94.33	96.86	147	62	93
Cs	0.83	0.94	0.67	0.72	0.73	0.64	0.74	0.70	0.69	n.a.	n.a.	n.a.
Ba*	878	968	713	791	736	674	797	759	791	1177	696	820
La	66.25	69.07	51.85	60.87	57.40	51.25	58.63	56.19	58.10	117	63	49
Ce	138.67	140.24	112.37	130.38	123.97	110.88	126.63	120.80	124.67	162	111	86
Pr	16.43	16.38	13.84	15.78	15.11	13.65	15.43	14.75	15.37	n.a.	n.a.	n.a.
Nd	62.54	61.82	55.00	61.51	58.73	53.92	59.82	58.01	59.99	66	44	41
Sm	12.59	12.12	11.50	12.48	12.13	11.33	12.05	11.85	12.61	n.a.	n.a.	n.a.
Eu	3.68	3.60	3.51	3.83	3.69	3.53	3.80	3.61	3.79	n.a.	n.a.	n.a.
Gd	10.38	9.91	10.21	10.68	10.35	9.81	10.82	10.34	10.64	n.a.	n.a.	n.a.
Tb	1.33	1.29	1.27	1.39	1.31	1.27	1.33	1.30	1.36	n.a.	n.a.	n.a.
Dy	6.89	6.73	6.66	7.28	7.07	6.69	7.01	6.77	7.06	n.a.	n.a.	n.a.
Ho	1.25	1.19	1.20	1.31	1.28	1.18	1.25	1.17	1.25	n.a.	n.a.	n.a.
Er	3.08	2.97	2.87	3.16	3.18	2.94	3.04	2.91	3.14	n.a.	n.a.	n.a.
Tm	0.42	0.39	0.39	0.44	0.41	0.40	0.41	0.40	0.39	n.a.	n.a.	n.a.
Yb	2.28	2.30	2.03	2.24	2.11	2.02	2.19	2.06	2.14	n.a.	n.a.	n.a.
Lu	0.34	0.33	0.30	0.34	0.32	0.31	0.32	0.29	0.32	n.a.	n.a.	n.a.
Hf	8.64	8.40	8.02	8.59	8.37	7.89	8.68	8.16	8.54	n.a.	n.a.	n.a.
Ta	6.33	6.30	4.92	5.72	5.47	4.85	5.69	5.40	5.64	n.a.	n.a.	n.a.
Pb	2.44	4.08	3.63	3.08	3.07	2.97	3.10	3.32	1.92	9	2	1
Th	4.93	5.44	3.78	4.19	3.88	3.58	4.11	3.90	4.00	21	17	16
U	1.19	1.33	0.94	1.02	0.96	0.88	1.01	0.95	0.97	2	5	1

ankaramitic basanite with a phenocryst content of ~20 vol.% each of clinopyroxene and olivine and ~2 vol.% magnetite. Fogo 36 is a basanite with 30-40 vol.% clinopyroxene and 5-10 vol.% magnetite phenocrysts. Fogo 37 is an ankaramitic tephrite with 30 vol.% of each clinopyroxene and olivine phenocrysts and 5 vol.% magnetite.

Table 2 Compositions of melts used for clinopyroxene-melt thermobarometry calculated by crystal fractionation modeling of observed phenocryst and microlite phases and (*) directly determined by EMP (c = collapse).

Melt	Used for	Age	SiO ₂	TiO ₂	Al ₂ O ₃	FeO(t)	MnO	MgO	CaO	Na ₂ O	K ₂ O	P ₂ O ₅	Total
Fogo 23	Fogo 23	1951	45.47	2.89	17.62	10.26	0.21	4.04	9.83	5.01	3.45	1.21	100.00
Fogo 45	Fogo 45, SD-10	1951	46.11	2.89	18.16	9.46	0.19	3.78	9.31	5.26	3.73	1.10	100.00
Fogo 52	Fogo 52	1951	46.03	2.76	17.07	10.74	0.19	4.08	9.38	4.77	3.60	1.40	100.01
Fogo 53	Fogo 53	1951	45.33	2.83	17.58	10.17	0.21	4.28	9.55	5.05	3.55	1.46	100.00
Fogo 55	Fogo 55	1951	45.91	3.01	17.18	10.33	0.21	3.93	9.36	5.01	3.62	1.43	100.00
Fogo 56	Fogo 56	1951	45.66	2.95	18.37	9.70	0.19	3.78	8.91	5.20	3.79	1.45	100.00
Fogo 57	Fogo 57	1951	45.84	3.01	17.76	10.01	0.20	3.85	9.29	4.98	3.65	1.41	100.00
Fogo 58	Fogo 58	1951	45.59	3.00	17.74	10.24	0.21	3.86	9.35	4.96	3.59	1.46	100.00
Fogo 39	Fogo 39	1785	42.99	4.00	15.78	12.74	0.19	4.90	12.13	4.59	2.01	0.69	100.00
Fogo 40	Fogo 40	1785	44.36	2.99	16.92	12.44	0.21	4.46	9.22	4.99	3.52	0.91	100.00
Fogo 28	Fogo 28	p.1680	44.43	3.06	18.00	10.30	0.18	4.04	9.69	5.61	3.89	0.81	100.02
Fogo 29	Fogo 29	p.1680	43.93	3.38	17.12	11.23	0.17	4.38	10.55	5.00	3.38	0.85	100.00
FG07SD3	FG07SD3	post-c	43.50	2.78	17.64	9.71	0.29	3.64	9.64	7.02	4.22	1.56	100.00
Fogo 16	Fogo 16	pre-c	45.69	3.35	16.07	11.25	0.27	4.56	13.19	2.74	1.67	1.20	100.00
Fogo 18*	Fogo 18	pre-c	42.95	3.17	16.27	11.49	0.21	4.38	11.98	5.05	2.90	0.97	99.36
Fogo 37	Fogo 37	pre-c	43.79	4.12	16.40	11.25	0.21	4.33	11.21	4.39	3.17	1.01	99.89
Fogo 36	Fogo 36	pre-c	42.84	3.49	17.82	10.68	0.21	4.18	9.94	5.18	4.89	0.79	100.00

3.3.1. Xenolith samples

Fogo 24 (1951 eruption) is a clinopyroxenite mesocumulate consisting of ~85 % euhedral to subhedral clinopyroxene, ~5 % spinel and 10 % of interstitial vesicular glass. The texture suggests that the glass represents a residual melt and/ or intruded host melt. Spinel occurs predominantly within clinopyroxene interstices. Amphibole occurs exclusively as inclusions in clinopyroxene. The clinopyroxenes contain some melt and fluid inclusions; intercrystalline trails cross-cutting more than one crystal were not observed. The open cumulate texture with euhedral crystals indicates that the xenolith was not completely crystallized when it was picked up by the 1951 magma.

Fogo 26 (1951 eruption) is a complex composite xenolith where a dunite fragment is embedded in a heterogeneous ultramafic cumulate consisting of varying amounts of clinopyroxene, amphibole, olivine, spinel, and glass. The dunite contains abundant fluid and melt inclusions and some veins consisting of dominantly clinopyroxene and minor amphibole. Dunite olivines are up to 4 mm in size, anhedral, and show strong intracrystalline deformation. Towards the cumulate it shows a ca. 0.5 mm wide reaction zone of relatively fine-grained clinopyroxene (<0.5 mm) and spinel. The cumulate partly consists of euhedral to subhedral clinopyroxene (<0.5 – 2 mm), spinel, poikilitic amphibole (up to 10 mm), and interstitial glass with vesicles showing a locally open texture. Other parts of the cumulate consist of large poikilitic amphibole hosting many rounded small olivines (<0.5 mm), and domains of vesicular glass with many euhedral olivines of similar size. The dunite may represent a mantle fragment that has experienced considerable overprinting by surrounding and infiltrating melts, probably

related to the entrainment of the fragment into a magma from which the cumulate formed. The locally open textures suggest that the cumulate was not completely crystallized when it was picked up by the 1951 magma.

Fogo 22 (1785 eruption or earlier) is a wehrlite with a dense texture that consists of almost monomineralic domains of anhedral clinopyroxene (<0.5 – 1 mm) and anhedral olivine (<0.5 – 5 mm) that are partly interconnected. Both minerals show strong intracrystalline deformation. Subordinate spinel occurs locally in interstices between olivine and / or clinopyroxene and as inclusions in olivine. Various trails of fluid and melt inclusion crosscut the xenolith. In one fine-grained domain anhedral olivine and clinopyroxene (<0.5 mm) occur admixed and show less intracrystalline deformation. This domain may represent a reaction zone between the xenolith and intruded host melt. Based on its texture and mineral assemblage this xenolith is interpreted as a cumulate.

Fogo 25 (1785 eruption or earlier) is a wehrlite xenolith consisting of ~70-80 % anhedral olivine (>0.5 – 5 mm), ~20 % clinopyroxene, and subordinate spinel, phlogopite and interstitial glass. It is cut by several veins containing vesicular brown glass indicating infiltration by a host melt. Crystals in contact with the interstitial glass show either straight or rounded crystal faces, which indicates that both crystal resorption and crystal growth occurred shortly before eruption. Fluid inclusions occur in olivine and clinopyroxene in different generations of trails that are restricted to individual crystals or crosscut crystal borders. We interpret the rock as a cumulate that was not completely crystallized when it was picked by the host melt that brought the xenolith to the surface.

Fogo 17 is a pyroxenite xenolith found in an ankaramitic lava flow (Fogo 16) of late pre-collapse age (Day, personal communication 2007) consisting of 85% anhedral clinopyroxene (1-10 mm), 10 % spinel (0.1-5 mm)w, and 5% amphibole. Clinopyroxenes show sieve textures; interstitial glass and smaller (0.1-1 mm) euhedral clinopyroxenes occur in one domain near the rim of the xenolith. Amphibole commonly shows reaction rims where it is replaced by phlogopite and clinopyroxene. Fluid inclusions occur as secondary trails often cross-cutting crystal boundaries of clinopyroxene and amphibole. Several open cracks crosscut the xenolith. The rock is interpreted as a cumulate that has experienced partial melting and cracking during transport to the surface.

3.3.2. Occurrence of fluid inclusions

The investigated CO₂-rich fluid inclusions occur in some olivine and clinopyroxene phenocrysts of the 1951 lavas and, more abundantly, in xenoliths of 1951 and older eruptions (Fig. 2). Many of these inclusions are associated with melt inclusions. Both primary inclusions, incorporated during mineral growth, and secondary inclusions, grouped in trails due to incorporation in healed cracks (Roedder, 1984), were investigated. Primary inclusions are oval to spherical or resemble the host-crystal shape, and occur isolated or clustered in small groups. Secondary inclusions are spherical to negatively crystal-shaped and arranged in trails crosscutting the mineral faces or, in case of xenoliths, sometimes even grain boundaries. Several generations of secondary fluid inclusion trails crosscutting each other occur in some parts of the xenoliths. Inclusion sizes vary between $\leq 1 \mu\text{m}$ and $16 \mu\text{m}$ with the vast majority around $2\text{-}6 \mu\text{m}$. Reaction products of interactions between fluid inclusions and their host mineral were not observed. A few inclusions show evidence for partial decrepitation in form of small crystallographically oriented cracks or trails of micro-inclusions radiating from larger inclusions. Those were excluded from our investigations.

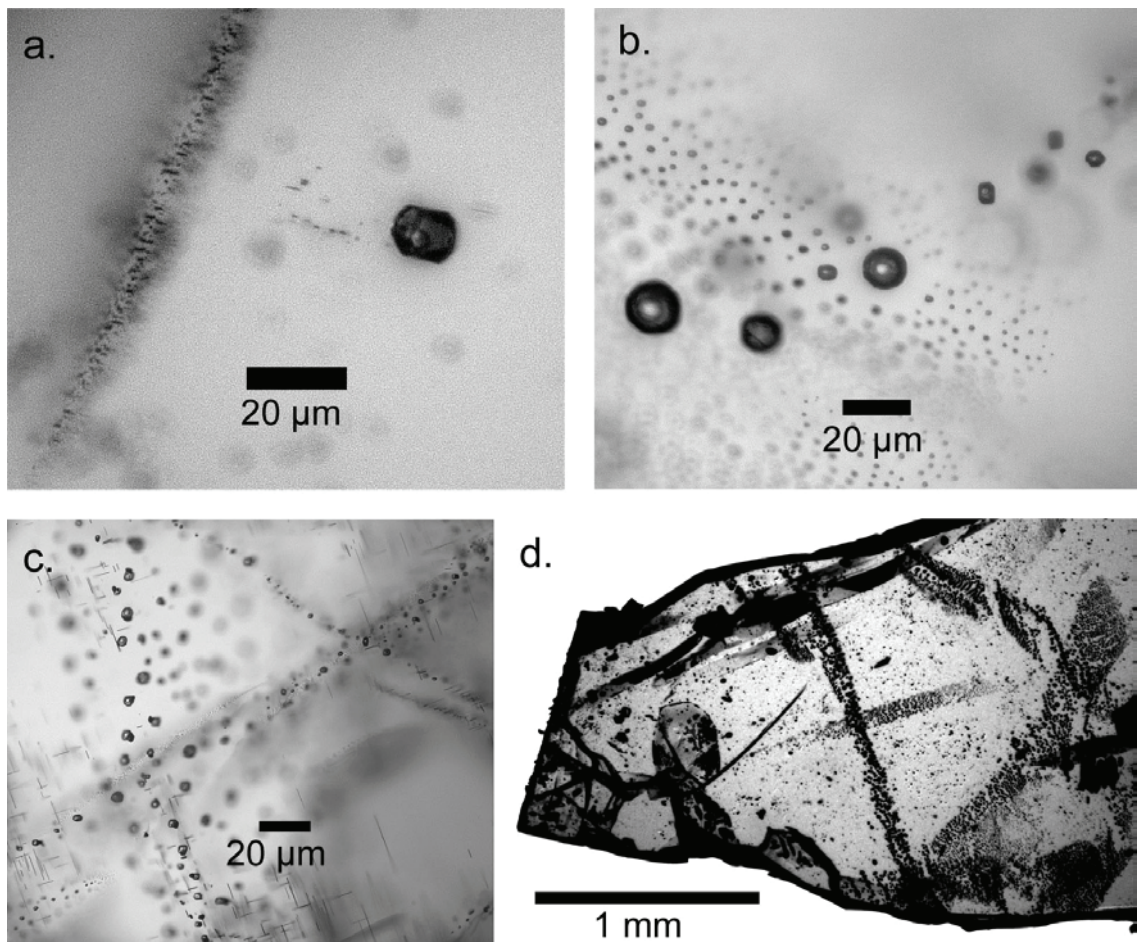


Fig. 2 Photomicrographs of fluid inclusions (FI) in studied phenocrysts and xenoliths. **a.** Primary FI resembling the crystal shape with visible CO₂ bubble in an olivine phenocryst of the 1951 eruption (Fogo 54). On the left side a trail of smaller melt inclusions crosscuts the mineral. **b.** Group of spherical primary FI with visible CO₂ bubbles in a clinopyroxene of a pyroxenite xenolith (Fogo 17), crosscut by a trail of smaller secondary FI. **c.** Various trails of secondary FI of different maturities in clinopyroxene of a xenolith (Fogo 17). FIs of mature trails resemble the crystal shape and show visible CO₂ bubbles. **d.** Diverse generations of secondary FI trails crosscut an olivine grain of a wehrlite xenolith (Fogo 22).

3.4. Analytical Methods

Fluid inclusions were examined in 100 µm thick doubly-polished sections. Microthermometric measurements were carried out using a Linkam® THMSG 600 heating-cooling stage at the Department of Geosciences, University of Bremen, calibrated with SYNFLINC® synthetic fluid inclusion standards at -56.6 °C (triple point of CO₂), 0.0 °C and 374.1 °C (H₂O). Accuracy of CO₂ triple-point measurements, and reproducibility of melting and homogenization temperatures, are better than ± 0.2 °C.

Densities of CO₂ inclusions were calculated using the auxiliary equations 3.14 and 3.15 of Span and Wagner (1996); the results closely match those obtained after Angus et al. (1976). Isochores and pressures were computed implementing the Sterner and Pitzer (1994) equation of state (EOS) for the CO₂-H₂O system. This EOS yields pressures almost identical to the frequently used EOS by Kerrick and Jacobs (1981) for densities below 0.8 g/cm³, see Hansteen and Klügel (2008).

Major element analyses of minerals and glasses were performed with a JEOL JXA 8200 electron microprobe (EMP) at IFM-GEOMAR, Kiel. Analytical conditions included a focused beam with a current of 10-20 nA for mineral phases at an acceleration voltage of 15 kV. Glasses were analyzed with a defocused beam of 5-10 µm and a current of 10 nA. Analytical precision and accuracy were monitored by regular analyses of standard reference materials; see Table A1 in the electronic supplementary material.

Whole-rock analyses of major elements, Sr, Ba and Zr of samples from the 1951 eruption were performed at IFM-GEOMAR using a Philips X'Unique PW 1480 X-ray fluorescence spectrometer; H₂O and CO₂ were analyzed with a Rosemount CSA 5003 infrared spectrometer. For all other samples XRF analyses were carried out at University of Hamburg using a Panalytical Magix PRO PW 2540 VCR wavelength dispersive X-ray spectrometer; other trace elements were analyzed with a Thermo Finnigan Element2 ICP-MS at the Department of Geosciences, University of Bremen following the procedure outlined in Geldmacher et al. (2008). See Tables A2 and A3 (electronic supplementary material) for standard reference material measurements accompanying the whole rock analyses.

3.5. Results

3.5.1. Whole-rock geochemistry

Major and trace element data of representative whole-rock analyses are reported in Table 1. The data show a well-defined liquid line of descent within the basanite/ tephrite field in the total alkali versus silica diagram (Fig. 3). Two of the prehistoric samples depart from this trend, plotting in the foidite field and at the border between basanite and picrite fields.

1951 eruption

The rocks of the 1951 eruption are basanites to tephrites (Fig. 3) with MgO contents varying between 5.0 and 8.2 wt.%. Bivariate plots of major elements (Figs. 3 and 4) display a well-defined liquid line of descent. The low concentrations of MgO, Ni (<75 ppm) and Cr (<160 ppm) of the 1951 rocks indicate that they do not represent primitive magma, and significant olivine \pm clinopyroxene fractionation must have occurred at depth. Trace element concentrations are very homogeneous for the 1951 samples (Fig. 5). The pattern is remarkably identical to those of the basanites of the 1995 Fogo eruption (Hildner et al., 2011). The slight compositional variations of the 1951 samples do not correlate with the eruption chronology; for example, the most magnesian sample (Fogo 52) is from the initial eruption phase of Monte Rendall, whereas the least magnesian one (Fogo 45) is from the late eruption phase at Monte Orlando (Fig. 1). The compositional heterogeneity of the 1951 lavas in conjunction with the little heterogeneity of the respective matrix compositions indicates highly variable phenocryst contents, which is in accordance with the petrographic observations. This conclusion is also confirmed by least square mass balance calculations; for example, the composition of Fogo 52 (MgO 8.2 wt.%) can be transformed into that of Fogo 45 (MgO 5.0 wt.%) by subtracting 22.7 wt.% clinopyroxene, 4.5 wt.% olivine, and 4.6 wt.% magnetite with a sum of squared residuals of only 0.087. The larger variability of highly incompatible (~40 % for Cs) compared to less incompatible trace elements (~10 % for Lu) (Table 1, Fig. 5) is also consistent with phenocryst accumulation. We thus conclude that all 1951 lavas from both northwest and south of Pico do Fogo arose from a single but slightly zoned magma batch.

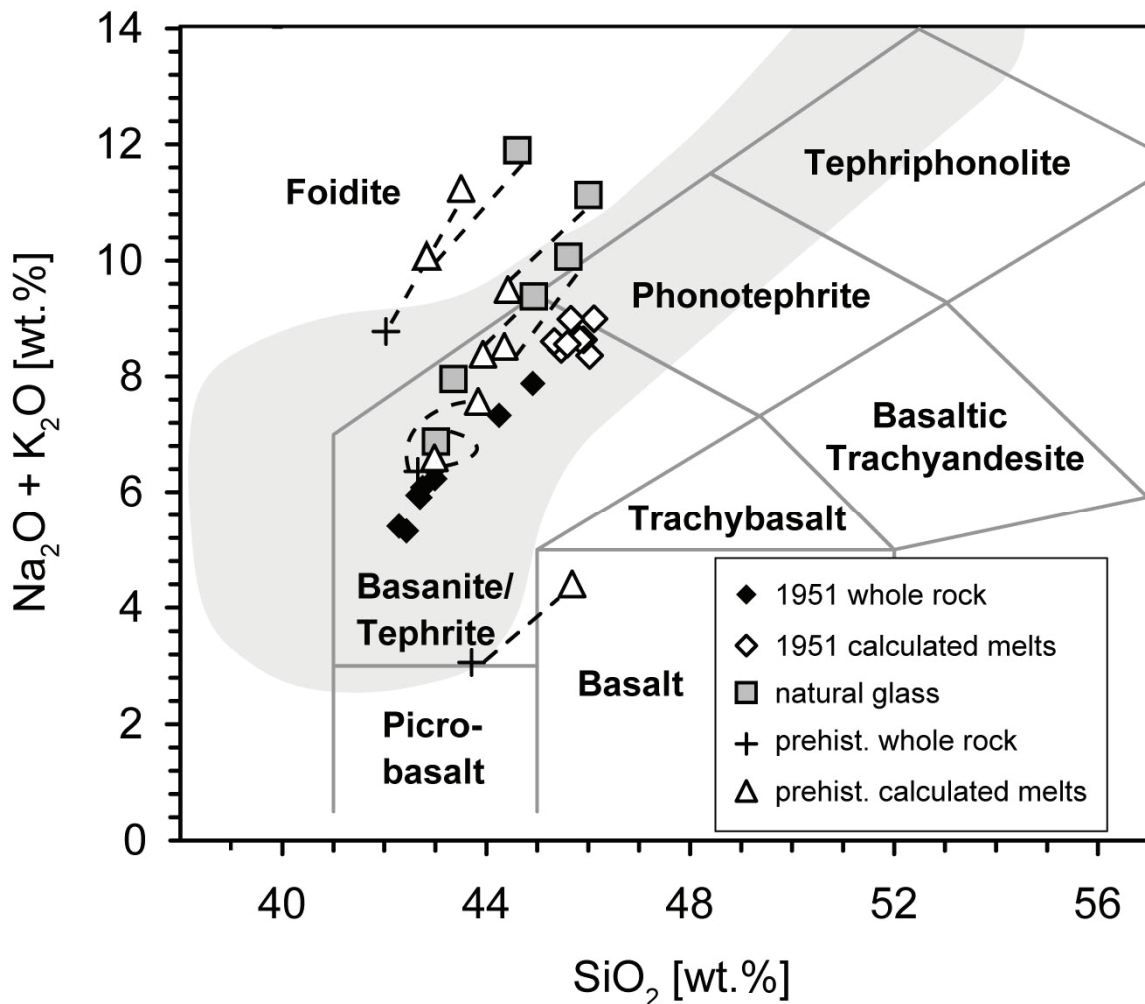


Fig. 3 Total alkali vs. silica diagram of whole-rock-, natural glass- and calculated glass compositions of the studied samples. Dashed lines connect whole-rock – melt pairs. Shaded: array of published Fogo data (Gerlach et al., 1988; Munhá et al., 1997; Kokfelt, 1998; Doucelance et al., 2003; Escrig et al., 2005; Hildner et al., 2011).

Prehistoric eruptions

Major and trace element data of two rock samples of late pre-collapse age (Fogo 16, basanite, MgO 9.8 wt.%; Fogo 37, tephrite, MgO 6.8 wt.%) and of one of early post-collapse age (FG07SD3, foidite, MgO = 5.2 wt.%) are similar to the 1951 data (Table 1, Figs. 3 and 4). Fogo 16 is slightly more primitive, and remarkably low in alkalis (Na_2O = 1.87 wt.%, K_2O = 1.08 wt.%) which may be due to slight alteration indicated by an increased H_2O content (2.18 wt.%).

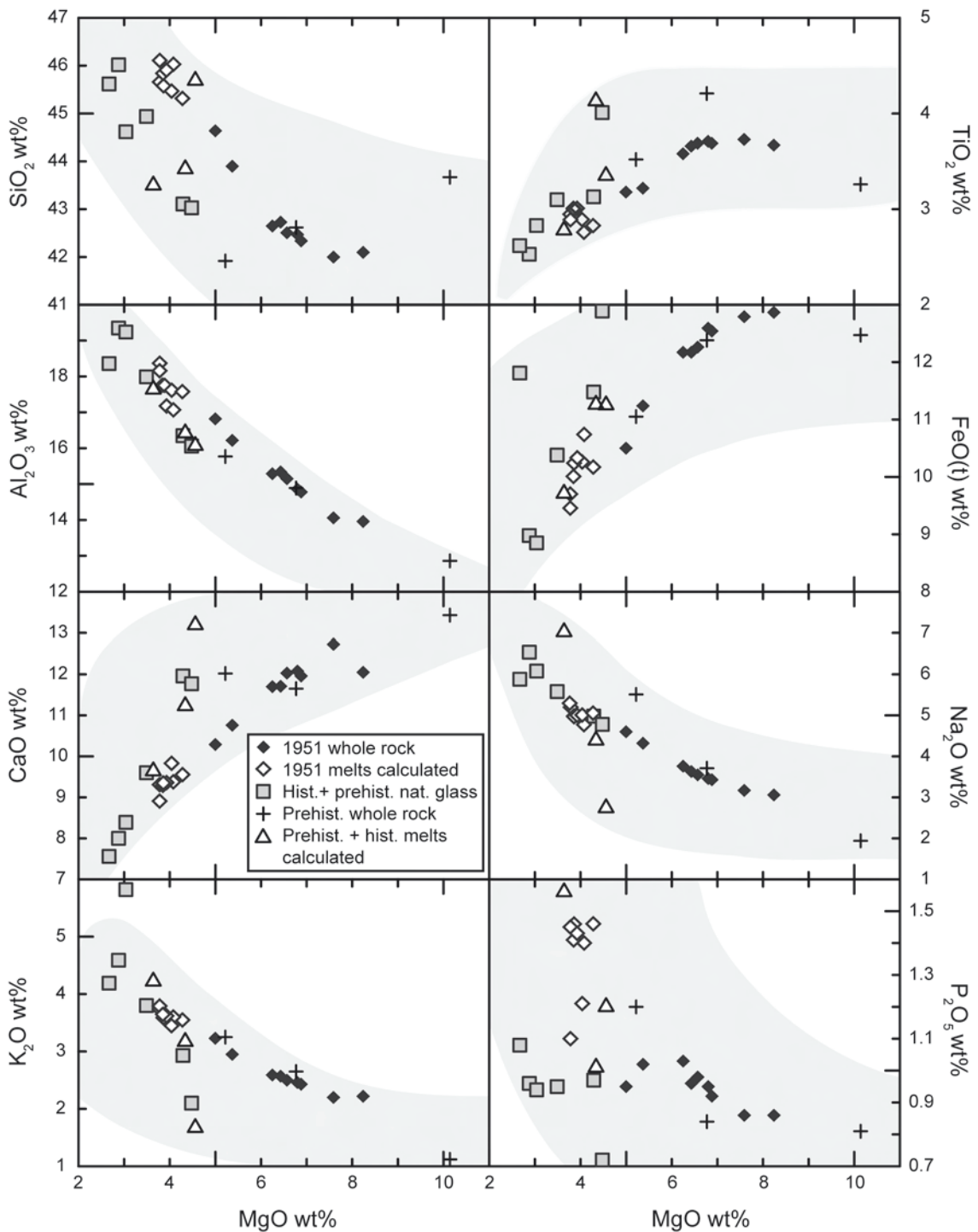


Fig. 4 Bivariate MgO plots of major elements including XRF whole rock data of 1951 and three prehistoric eruptions, calculated melt compositions of 1951 and various historic and prehistoric eruptions, and EMP-data of natural glasses of historic and prehistoric eruptions. Shaded: array of published Fogo data (Gerlach et al., 1988; Munhá et al., 1997; Kokfelt, 1998; Doucelance et al., 2003; Escrig et al., 2005; Hildner et al., 2011).

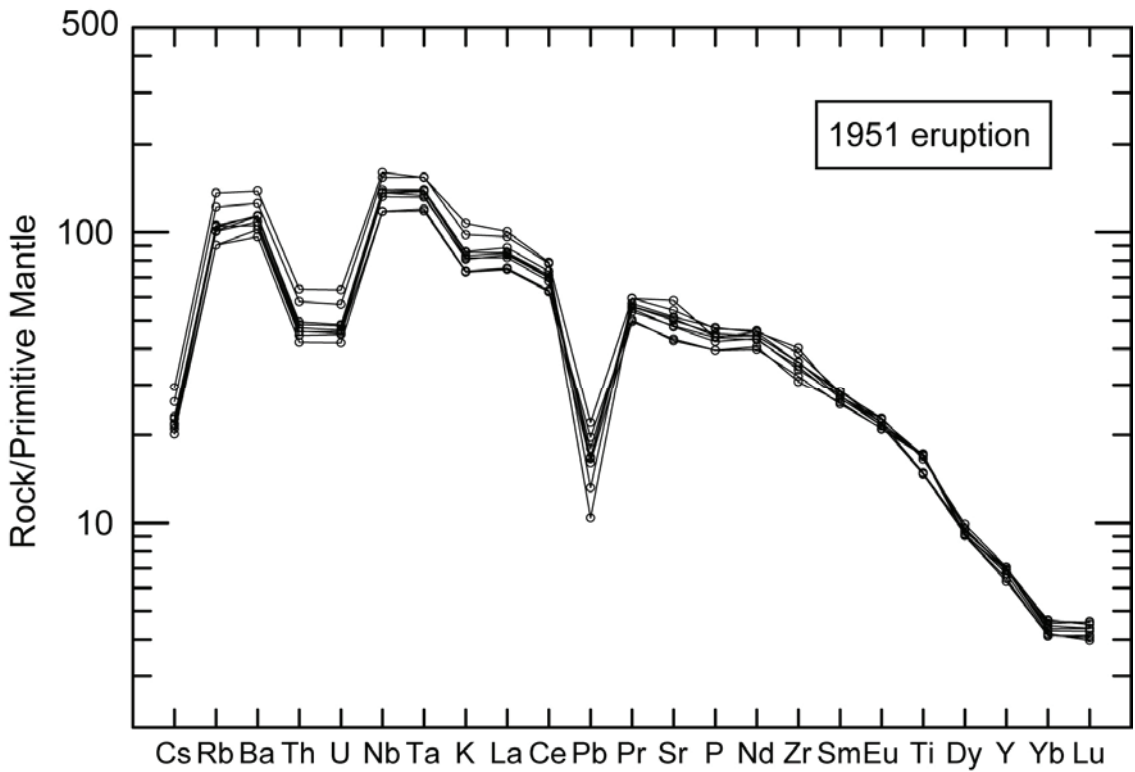


Fig. 5 Incompatible element diagram of investigated lavas of the 1951 eruption, normalized to primitive mantle (Sun and McDonough 1989). The distribution is congruent with this of the basanites erupted during the 1995 Fogo eruption (Hildner et al., 2011).

3.5.2. Clinopyroxene-melt geothermobarometry

Temperatures and pressures of crystallization of clinopyroxene phenocrysts were calculated by applying the clinopyroxene-melt geothermobarometer of Putirka et al. (2003), which is based on jadeite crystallization and jadeite – diopside+hedbergite exchange equilibria. The standard errors of estimate derived from a test data set are ± 33 K and ± 170 MPa.

Clinopyroxene compositions (Table 3) were determined by averaging 4-20 microprobe analyses from a distance of 5-10 μm to the rim of euhedral phenocrysts. Clinopyroxenes exhibiting sector zoning were avoided. The glass composition of sample Fogo 18 was analyzed directly with the microprobe. For all 1951 samples and for Fogo 16, Fogo 37 and FG07SD3 having a microcrystalline or microlite-rich matrix, the melt compositions were calculated by mass balance using the observed amount of phenocrysts and the respective whole rock compositions (Tables 2 and 4). For sample FG01SD-10, the calculated composition of Fogo 45 melt was used, because no whole-rock data are available and all 1951 glasses/ melts show little compositional variability. For samples Fogo 28, 29, 39, 40 and 36 containing fresh glass with microlites,

micropore glass analyses were corrected by adding the composition of observed microlite phases (Fig. 3).

In order to test whether melt compositions are in chemical equilibrium with the respective clinopyroxene rim compositions, the following criteria were applied:

1) Test of Fe-Mg exchange equilibrium between clinopyroxene and melt. This test is not straightforward because $K_d = X(\text{Fe}^*/\text{Mg})_{\text{Cpx}} / X(\text{Fe}^*/\text{Mg})_{\text{liq}}$ was highly variable in the calibration data of the thermobarometer (X are molar fractions and Fe^* denotes total iron content). In addition, $f\text{O}_2$ and $\text{Fe}^{3+}/\text{Fe}^{2+}$ in experimental and natural clinopyroxene-melt pairs may differ strongly from each other. As suggested by Putirka et al. (2003), we used a constant K_d of 0.275 for the equilibrium test. Another test was made using the empirical relation after Duke (1976):

$$\log\left(\frac{X_{\text{Fe}}}{X_{\text{Mg}}}\right)_{\text{Cpx}} = -0.564 + 0.755 * \log\left(\frac{X_{\text{Fe}}}{X_{\text{Mg}}}\right)_{\text{liq}}.$$

Clinopyroxene analyses with a discrepancy between the measured and both calculated Fe/Mg ratios of $>5\%$ were discarded (32 out of 169 samples).

2) Test whether measured clinopyroxene components (DiHd, EnFs, Jd, CaTs) match those predicted by the clinopyroxene saturation model of Putirka (1999) within the $\pm 2\sigma$ level; cf. Putirka et al. (2003). Clinopyroxenes outside this range were discarded (1 out of 169; Fig. 6).

The effect of analytical uncertainties on calculated P and T is generally smaller than the prediction error of the thermobarometer (Klügel et al., 2005). For the current data set, the pressure and temperature uncertainties due to analytical errors are ± 48 MPa and $\pm 8^\circ\text{C}$ (2σ), estimated for a test data set of 500 random numbers by using the relative standard deviation of micropore analyses of reference materials.

Table 3 Compositions of clinopyroxene rims used for clinopyroxene-melt thermobarometry. Each sample comprises the mean value of 5-20 analyzed points of one clinopyroxene phenocryst. P and T calculated after Putirka et al. (2003).

Sample #	SiO ₂	TiO ₂	Al ₂ O ₃	FeO	MnO	MgO	CaO	Na ₂ O	Cr ₂ O ₃	Total	Mg#	P [MPa]	T [°C]
Fogo 23_08	43.66	3.86	9.59	8.06	0.18	11.48	22.42	0.48	0.01	99.77	71.75	570	1107
Fogo 23_09	43.08	3.99	10.42	8.03	0.19	10.87	22.02	0.55	0.00	99.20	70.71	650	1116
Fogo 23_16	42.58	4.10	10.80	8.28	0.17	10.91	22.26	0.52	0.01	99.65	70.13	620	1114
Fogo 23_23	45.80	3.01	8.09	7.71	0.18	12.22	22.42	0.46	0.01	99.95	73.87	540	1103
Fogo 23_37	43.50	3.60	9.97	8.18	0.16	11.18	22.19	0.54	0.01	99.37	70.90	630	1113
Fogo 23_39	46.77	2.68	7.24	7.64	0.21	12.63	22.03	0.47	0.01	99.74	74.66	550	1103
Fogo 45_08	42.99	4.15	10.85	7.80	0.16	11.07	22.37	0.50	0.01	99.93	71.69	580	1101
Fogo 45_10	45.12	3.51	9.02	7.57	0.13	12.15	22.75	0.44	0.00	100.70	74.10	500	1090
Fogo 45_17	42.91	4.17	10.75	7.81	0.15	11.03	22.23	0.51	0.01	99.59	71.58	590	1102
Fogo 45_19	43.28	4.07	10.80	7.74	0.12	11.18	22.49	0.52	0.01	100.23	72.01	590	1101
Fogo 45_25	42.64	4.32	10.80	7.89	0.15	10.91	22.61	0.53	0.01	99.87	71.16	600	1101
Fogo 45_28	43.16	4.01	10.37	7.85	0.14	11.37	22.54	0.48	0.00	99.93	72.08	550	1097
Fogo 45_29	43.48	4.02	10.26	7.74	0.15	11.36	22.45	0.50	0.01	100.01	72.36	570	1099
Fogo 52_03	41.46	4.72	11.41	8.04	0.11	10.79	22.47	0.45	0.00	99.49	70.52	580	1113
Fogo 52_04	41.49	4.72	11.36	8.23	0.12	10.81	22.48	0.46	0.02	99.71	70.08	590	1114
Fogo 52_05	42.01	4.82	11.73	8.00	0.14	10.85	22.51	0.47	0.01	100.56	70.73	600	1116
Fogo 52_07	41.59	4.84	11.60	8.16	0.12	10.72	22.50	0.46	0.00	100.03	70.08	590	1115
Fogo 52_12	41.57	4.89	11.64	8.25	0.14	10.63	22.46	0.49	0.01	100.12	69.68	620	1117
Fogo 52_13	41.85	4.60	11.41	8.08	0.09	10.91	22.57	0.45	0.00	100.00	70.64	580	1113
Fogo 52_15	42.98	4.19	10.66	7.84	0.11	11.29	22.58	0.44	0.01	100.12	71.98	560	1110
Fogo 52_16	41.71	4.77	11.58	8.27	0.11	10.71	22.49	0.47	0.01	100.15	69.78	600	1115
Fogo 52_17	41.70	4.58	11.11	8.16	0.12	10.72	22.59	0.47	0.01	99.48	70.07	600	1113
Fogo 52_19	41.85	4.50	11.17	8.07	0.13	10.99	22.45	0.46	0.00	99.66	70.82	590	1114
Fogo 53_01b	45.78	2.94	8.17	7.20	0.13	12.69	22.69	0.41	0.00	100.02	75.86	540	1102
Fogo 55_02	41.86	3.79	11.28	8.13	0.11	10.70	23.38	0.45	0.00	99.73	70.11	550	1103
Fogo 55_03	42.30	3.65	11.15	7.94	0.12	10.81	23.35	0.44	0.01	99.78	70.80	530	1101
Fogo 55_06	41.93	3.78	11.35	8.05	0.12	10.64	23.40	0.47	0.01	99.76	70.20	570	1104
Fogo 55_07	41.68	4.01	11.30	8.26	0.12	10.58	23.46	0.47	0.01	99.90	69.55	570	1104
Fogo 55_08	42.65	3.73	10.68	7.93	0.07	11.06	23.57	0.45	0.00	100.16	71.32	540	1100
Fogo 56_07	44.44	3.29	9.56	8.52	0.14	11.79	21.91	0.47	0.00	100.15	71.16	590	1092
Fogo 56_09	44.46	3.41	9.72	8.55	0.12	11.72	21.88	0.45	0.00	100.33	70.97	570	1092
Fogo 56_13	46.57	2.53	7.44	7.92	0.16	12.82	21.74	0.40	0.01	99.61	74.27	510	1083
Fogo 56_22	44.77	3.11	8.59	8.42	0.13	12.15	21.67	0.41	0.00	99.28	72.02	520	1086
Fogo 57_01	41.54	4.17	11.71	8.02	0.14	10.40	23.22	0.51	0.00	99.73	69.81	600	1103
Fogo 57_04	42.43	3.89	10.65	7.95	0.12	10.87	23.42	0.46	0.01	99.82	70.92	550	1096
Fogo 57_05	41.78	4.02	11.04	8.05	0.13	10.73	23.44	0.46	0.00	99.66	70.38	550	1097
Fogo 57_09	41.49	4.17	11.23	8.06	0.12	10.60	23.48	0.48	0.00	99.65	70.11	570	1099
Fogo 57_10	41.66	4.02	11.46	7.93	0.14	10.33	23.36	0.50	0.00	99.44	69.89	600	1101
Fogo 58_01	45.32	2.65	7.91	7.55	0.17	12.18	23.29	0.43	0.00	99.51	74.21	490	1087
Fogo 58_02	42.25	3.63	10.63	8.00	0.12	10.94	23.40	0.47	0.01	99.46	70.90	560	1096
Fogo 58_04	42.18	3.75	10.60	8.10	0.12	10.93	23.32	0.49	0.01	99.53	70.64	580	1098
Fogo 58_07	41.53	3.79	11.19	8.23	0.15	10.54	23.31	0.52	0.01	99.29	69.54	610	1101
Fogo 58_08	42.30	3.69	10.40	8.07	0.13	11.08	23.35	0.48	0.02	99.53	70.99	570	1097
Fogo 58_09	42.10	3.75	10.73	8.30	0.13	10.86	23.31	0.48	0.01	99.68	69.99	580	1098
SD10_01	42.52	4.31	10.74	8.01	0.12	11.04	22.41	0.46	0.01	99.64	71.05	540	1097
SD10_09	44.41	3.63	9.31	7.71	0.13	11.92	22.51	0.42	0.01	100.07	73.37	480	1090
SD10_10	46.29	2.30	7.79	7.81	0.16	12.37	22.33	0.43	0.00	100.26	73.85	490	1088
SD10_13	42.34	4.36	11.04	8.07	0.14	10.86	22.52	0.47	0.01	99.84	70.58	550	1098
SD10_15	42.21	4.43	11.27	8.09	0.13	10.77	22.39	0.50	0.01	99.82	70.35	590	1102
Fogo 36_01	44.12	3.93	9.81	7.33	0.15	11.33	22.97	0.55	0.01	100.21	73.4	810	1102
Fogo 36_02	42.42	4.67	11.29	7.34	0.12	10.73	22.99	0.54	0.01	100.15	72.3	810	1105
Fogo 36_03	42.72	4.47	11.13	7.38	0.13	10.74	22.77	0.60	0.00	99.96	72.2	870	1110
Fogo 36_04	41.82	4.91	11.49	7.27	0.13	10.67	22.98	0.55	0.00	99.84	72.4	820	1106
Fogo 36_06	41.76	4.96	11.55	7.45	0.13	10.63	22.99	0.56	0.01	100.05	71.8	830	1107
Fogo 36_07	41.90	4.93	11.71	7.39	0.13	10.51	23.02	0.55	0.01	100.17	71.7	830	1107
Fogo 36_08	41.63	4.70	11.83	7.58	0.11	10.54	22.93	0.58	0.01	99.93	71.3	850	1109
Fogo 36_09	40.62	5.66	12.31	7.53	0.14	10.07	22.92	0.57	0.01	99.86	70.5	850	1110
Fogo 36_10	41.69	4.99	11.69	7.34	0.11	10.57	22.85	0.55	0.01	99.83	72.0	830	1108
Fogo 36_11	41.99	4.73	11.61	7.45	0.12	10.68	22.91	0.57	0.01	100.08	71.9	840	1108
Fogo 37_01	41.93	5.16	11.42	7.96	0.11	10.68	22.81	0.46	0.01	100.58	70.5	600	1131
Fogo 37_02	42.64	4.75	11.00	7.59	0.11	10.78	22.91	0.47	0.01	100.27	71.7	600	1130
Fogo 37_03	41.94	5.03	11.18	7.80	0.12	10.78	22.78	0.44	0.01	100.08	71.1	580	1129
Fogo 37_04	42.44	4.72	10.88	7.69	0.11	10.80	22.70	0.46	0.01	99.83	71.5	600	1130
Fogo 37_05	41.63	5.26	11.50	7.80	0.10	10.58	22.85	0.44	0.01	100.19	70.7	580	1129
Fogo 37_06	42.10	5.07	11.18	7.63	0.12	10.69	23.02	0.46	0.02	100.30	71.4	600	1129
Fogo 37_07	44.07	4.19	9.95	7.55	0.13	11.27	23.00	0.46	0.02	100.65	72.7	580	1126
Fogo 37_08	40.82	5.32	11.52	8.02	0.09	10.46	22.83	0.49	0.02	99.58	69.9	630	1133
Fogo 37_09	42.18	4.80	11.02	7.81	0.10	10.76	22.86	0.48	0.00	100.03	71.1	610	1131
Fogo 37_10	42.69	4.80	11.05	7.62	0.11	10.70	22.87	0.47	0.01	100.33	71.4	600	1130
Fogo 37_11	41.33	5.29	11.56	7.90	0.12	10.43	22.66	0.48	0.01	99.80	70.2	630	1133

Table 3 (continued)

Sample #	SiO ₂	TiO ₂	Al ₂ O ₃	FeO	MnO	MgO	CaO	Na ₂ O	Cr ₂ O ₃	Total	Mg#	P [MPa]	T [°C]
Fogo 37_12	42.48	4.57	10.79	7.71	0.09	11.12	22.73	0.45	0.01	99.96	72.0	590	1129
Fogo 37_14	42.31	4.91	11.18	8.05	0.12	10.56	22.76	0.49	0.01	100.43	70.0	630	1133
Fogo 37_15	41.47	5.30	11.59	7.81	0.10	10.50	22.66	0.47	0.01	99.91	70.6	610	1132
Fogo 37_16	43.88	4.17	10.40	7.62	0.12	11.00	22.81	0.48	0.01	100.52	72.0	610	1130
Fogo 37_17	43.16	4.52	10.81	7.69	0.10	10.79	22.78	0.49	0.01	100.36	71.4	630	1132
Fogo 37_18	45.25	3.69	8.48	7.25	0.13	12.03	22.94	0.42	0.01	100.20	74.7	530	1119
Fogo 16_01	43.79	3.67	10.20	7.60	0.10	11.56	23.12	0.51	0.01	100.57	73.1	540	1173
Fogo 16_02	44.62	3.42	10.09	7.50	0.10	11.52	23.24	0.50	0.02	101.01	73.2	520	1172
Fogo 16_05	42.89	4.25	11.27	7.85	0.11	10.72	23.13	0.52	0.01	100.77	70.9	560	1177
Fogo 16_07	44.66	3.59	9.76	7.77	0.13	11.29	23.13	0.56	0.01	100.92	72.1	580	1175
Fogo 16_09	44.52	3.40	9.81	7.44	0.10	11.79	23.22	0.49	0.01	100.81	73.9	510	1170
Fogo 16_11	44.31	3.40	9.85	7.41	0.11	11.73	23.18	0.46	0.20	100.66	73.8	490	1169
Fogo 16_12	45.99	2.95	8.49	7.02	0.11	12.38	23.27	0.45	0.01	100.69	75.9	450	1163
Fogo 16_13	44.45	3.47	10.00	7.65	0.11	11.64	23.16	0.51	0.01	100.99	73.1	530	1172
Fogo 18_01	45.45	3.07	8.57	7.61	0.12	11.98	23.06	0.40	0.05	100.32	73.7	420	1114
Fogo 18_03	43.98	3.38	9.95	7.63	0.09	11.46	22.92	0.42	0.16	100.02	72.8	470	1121
Fogo 18_04	42.56	4.16	11.08	8.27	0.09	10.78	22.99	0.44	0.09	100.46	69.9	500	1125
Fogo 18_05	43.31	4.04	10.29	8.21	0.11	11.04	22.90	0.44	0.06	100.41	70.6	480	1122
Fogo 18_07	42.24	4.13	11.19	8.09	0.10	10.72	22.83	0.45	0.01	99.78	70.3	510	1126
Fogo 18_10	41.99	4.51	11.63	8.29	0.11	10.41	22.94	0.47	0.01	100.38	69.1	530	1128
Fogo 18_11	42.35	4.20	11.26	8.32	0.12	10.66	22.92	0.46	0.05	100.35	69.5	520	1127
Fogo 18_12	42.18	4.47	11.76	8.32	0.11	10.54	22.94	0.44	0.05	100.82	69.3	500	1127
FG07SD3_01	42.54	4.64	10.12	7.53	0.15	10.97	23.02	0.60	0.00	99.60	72.2	700	1084
FG07SD3_02	42.62	4.76	10.33	7.67	0.15	10.92	23.06	0.58	0.01	100.11	71.7	690	1084
FG07SD3_03	41.67	5.09	10.79	7.79	0.17	10.67	23.07	0.61	0.02	99.90	70.9	710	1086
FG07SD3_04	43.80	4.21	9.42	7.53	0.15	11.34	23.12	0.60	0.01	100.21	72.9	690	1082
FG07SD3_07	42.54	4.82	10.65	7.72	0.15	10.84	23.01	0.59	0.02	100.36	71.4	690	1085
FG07SD3_08	42.12	4.99	10.54	7.90	0.16	10.91	23.22	0.57	0.01	100.45	71.1	670	1083
FG07SD3_09	42.13	5.04	10.77	8.09	0.19	10.69	23.10	0.63	0.01	100.66	70.2	730	1087
FG07SD3_10	42.23	4.86	10.40	8.02	0.17	10.75	22.99	0.62	0.02	100.08	70.5	720	1086
FG07SD3_11	42.40	4.84	10.58	7.79	0.14	10.89	23.22	0.58	0.01	100.45	71.4	680	1083
FG07SD3_12	43.04	4.58	9.79	8.01	0.18	11.09	22.94	0.63	0.00	100.28	71.2	720	1086
FG07SD3_13	41.72	5.27	10.90	8.04	0.14	10.69	23.08	0.60	0.00	100.44	70.3	700	1086
FG07SD3_14	42.91	4.66	10.03	7.64	0.15	11.02	23.07	0.60	0.00	100.11	72.0	700	1084
FG07SD3_15	43.11	4.67	10.17	7.68	0.13	11.04	23.17	0.58	0.01	100.58	71.9	680	1083
Fogo 28_01	42.54	4.39	11.54	7.52	0.15	10.67	22.67	0.50	0.01	100.02	71.7	660	1102
Fogo 28_02	41.48	4.55	11.57	7.29	0.16	10.29	22.47	0.50	0.01	98.34	71.6	670	1102
Fogo 28_03	42.68	3.86	9.95	7.03	0.15	11.18	22.57	0.46	0.01	97.94	73.9	620	1095
Fogo 28_06	42.35	3.53	11.18	7.45	0.13	11.01	22.78	0.49	0.01	98.97	72.5	650	1100
Fogo 28_07	42.13	4.18	11.02	7.03	0.13	10.85	22.54	0.48	0.01	98.40	73.3	650	1099
Fogo 28_08	40.26	4.68	12.21	7.47	0.14	9.87	22.48	0.54	0.01	97.69	70.2	710	1106
Fogo 28_09	41.23	4.38	11.63	7.49	0.13	10.58	22.80	0.50	0.01	98.78	71.6	670	1101
Fogo 28_10	42.84	3.95	11.08	7.33	0.14	10.96	22.70	0.51	0.01	99.55	72.7	670	1101
Fogo 28_11	41.76	4.09	11.23	7.23	0.12	10.81	22.65	0.50	0.01	98.43	72.7	660	1100
Fogo 28_12	42.46	3.97	10.98	7.22	0.14	10.90	22.60	0.51	0.01	98.80	72.9	670	1101
Fogo 28_13	40.92	4.48	12.01	7.44	0.14	10.23	22.57	0.50	0.01	98.33	71.0	670	1103
Fogo 28_14	42.14	4.27	11.31	7.27	0.13	10.82	22.76	0.49	0.01	99.23	72.6	650	1100
Fogo 29_01	42.62	3.78	11.32	7.67	0.11	10.64	22.57	0.45	0.01	99.20	71.2	620	1119
Fogo 29_02	42.69	3.85	11.36	7.68	0.12	10.68	22.57	0.46	0.01	99.43	71.3	630	1119
Fogo 29_05	42.99	3.76	11.04	7.60	0.13	10.79	22.69	0.45	0.01	99.47	71.7	610	1117
Fogo 29_06	41.72	4.13	11.87	7.84	0.12	10.28	22.40	0.47	0.01	98.88	70.0	650	1122
Fogo 29_07	43.94	3.34	9.81	7.82	0.13	11.13	22.42	0.45	0.01	99.06	71.7	600	1115
Fogo 29_09	43.31	3.96	11.04	7.54	0.13	10.96	22.65	0.44	0.01	100.08	72.2	600	1117
Fogo 29_11	41.76	4.79	12.11	7.83	0.12	10.29	22.34	0.47	0.01	99.76	70.1	650	1124
Fogo 29_12	42.68	4.28	11.30	7.47	0.12	10.89	22.61	0.44	0.01	99.83	72.2	610	1118
Fogo 39_01	43.72	3.99	10.52	7.37	0.11	11.26	22.55	0.41	0.22	100.18	73.1	560	1143
Fogo 39_06	44.69	3.42	9.74	7.05	0.11	11.78	22.70	0.40	0.28	100.17	74.9	540	1139
Fogo 39_09	43.97	3.71	10.17	7.21	0.09	11.41	22.61	0.40	0.25	99.85	73.8	550	1141
Fogo 39_12	42.01	4.77	11.65	7.94	0.11	10.64	22.34	0.46	0.13	100.05	70.5	630	1150
Fogo 40_01	42.13	4.42	11.21	8.36	0.09	10.72	22.77	0.42	0.00	100.14	69.6	670	1107
Fogo 40_02	41.11	4.79	11.95	8.37	0.12	10.35	22.86	0.44	0.00	100.01	68.8	700	1110
Fogo 40_03	44.90	3.41	9.07	8.00	0.14	11.75	22.82	0.38	0.00	100.48	72.3	610	1098
Fogo 40_04	41.87	4.44	11.34	8.35	0.10	10.58	22.68	0.43	0.00	99.80	69.3	690	1109
Fogo 40_05	41.30	4.69	11.86	8.37	0.13	10.48	22.73	0.44	0.00	100.02	69.1	710	1111
Fogo 40_09	42.57	4.26	11.23	8.23	0.11	10.68	22.85	0.42	0.00	100.36	69.8	680	1107
Fogo 40_10	42.35	4.24	10.99	8.34	0.12	10.77	22.73	0.45	0.00	100.00	69.7	710	1109
Fogo 40_15	42.04	4.35	11.50	8.41	0.12	10.73	22.79	0.44	0.00	100.41	69.5	700	1110

Table 4 Fractions of phenocryst phases used for melt calculations.

Sample	Fractionated phenocryst phases (wt.%)			
	Ol	Cpx	Amph	Mag
Fogo 23	1	10	2	2
Fogo 45	1	10	0	2
Fogo 52	5.5	28	0	4.5
Fogo 53	0	20	5	4
Fogo 55	3.5	30	1	5
Fogo 56	0.75	25	3	4.5
Fogo 57	2.5	25	0	5
Fogo 58	1.5	22	5	4
Fogo 16	11	20	0	2
Fogo 37	4.5	10	0	2
FG07SD3	0	20	0	3

Calculated pressures and temperatures

Historic eruptions

Clinopyroxenes from the 1951 eruption yield a well-defined pressure range of 480-650 MPa (n=49) with 90% of the data between 500 and 640 MPa. Calculated temperatures range between 1080 and 1120 °C (Fig. 7). The two 1785 samples show 540-630 MPa and 1140-1150°C for Fogo 39 (n=4), and 610-710 MPa and 1100-1110 °C for Fogo 40 (n=8). Three samples of early post-1680 eruptions were used for thermobarometry. Fogo 28 and Fogo 29 are presumably from the same eruption (Day, personal communication 2007) and show a data range of 600-710 MPa and 1095-1125 °C (n=20). Fogo 18 (n=8) yields 420-530 MPa and 1115-1130 °C.

Prehistoric eruptions

FG07SD3 of post-collapse age yields a pressure range of 670-730 MPa (n=13) and a temperature distribution of 1080-1090 °C. The three samples predating the collapse event yield following distributions: data from the presumably oldest rock Fogo 36 (n=9) show a pressure range of 810-870 MPa and a temperature range of 1105-1110 °C. The youngest lavas of pre-collapse age, yield 450-580 MPa and 1160-1180 °C for Fogo 16 (n=8) and 530-630 MPa and 1120-1130 °C for Fogo 37 (n=16).

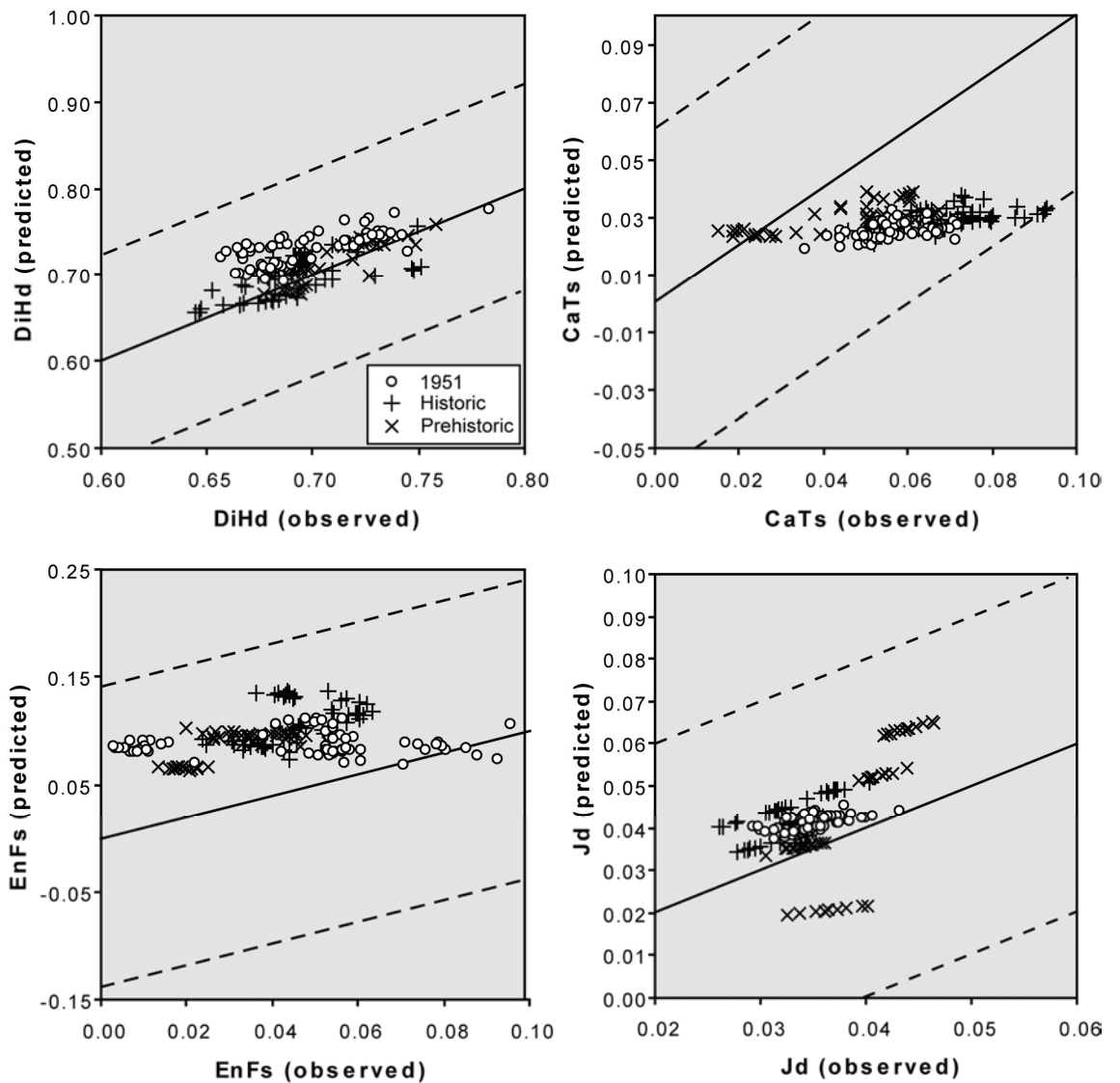


Fig. 6 Observed compositions of clinopyroxene phenocrysts compared to predicted compositions using models 3.1 – 3.7 of Putirka (1999). Clinopyroxene components: DiHd, diopside-hedenbergite; EnFs, enstatite-ferrosilite, CaTs, Ca-Tschermak's; Jd, jadeite. Error ranges of the predicted pyroxene compositions (dashed lines) comprise twice the standard error of estimate of the Putirka (1999) models, i.e. a 2σ uncertainty.

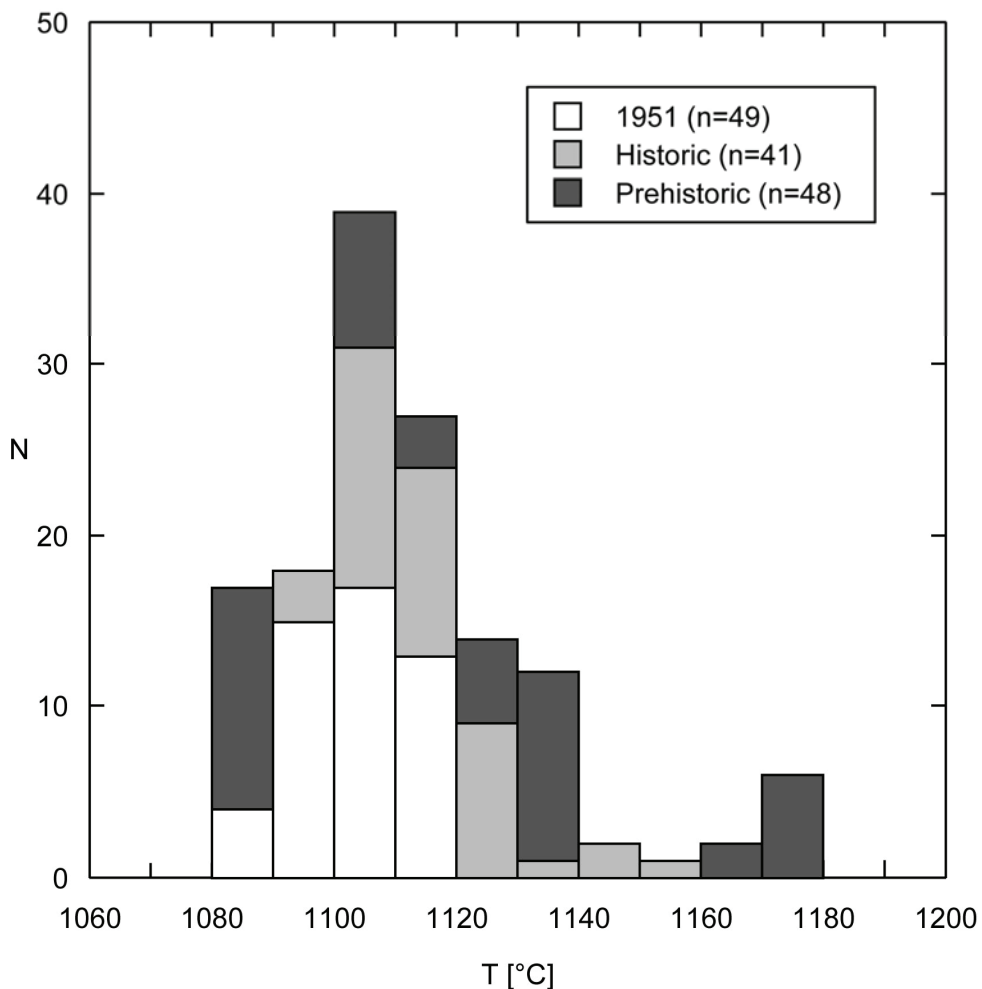


Fig. 7 Temperature distributions derived from clinopyroxene-melt equilibria of the 1951 and of several historic and prehistoric eruptions.

3.5.3. Microthermometry

Fluid inclusion compositions

Fluid inclusions ($n = 733$) were investigated by microthermometry and were selected from olivine and clinopyroxene phenocrysts in six lava samples and in two xenoliths of the 1951 eruption, in two wehrlite xenoliths of the 1785 eruption and in one prehistoric pyroxenite xenolith. All observed fluids froze to aggregates of solid CO_2 and vapor during cooling to between -80 and -100 °C. Further cooling (-190 °C) did not generate other phase transitions. During reheating, melting of solid CO_2 started between -57.4 and -56.4 °C, close to the triple point of CO_2 (-56.6 °C) (Fig. 8). Initial (T_i) and final melting (T_m) coincided in almost all cases; only 5 inclusions showed a melting interval of 0.2 - 0.3 °C. Most inclusions homogenized into the liquid phase below or at the critical point of CO_2 (31.1 °C). Some olivine-hosted inclusions of the two 1951 xenolith

samples homogenized into the vapor phase or showed critical homogenization, but only for a few of them the homogenization temperatures could be measured reliably due to optical limitations.

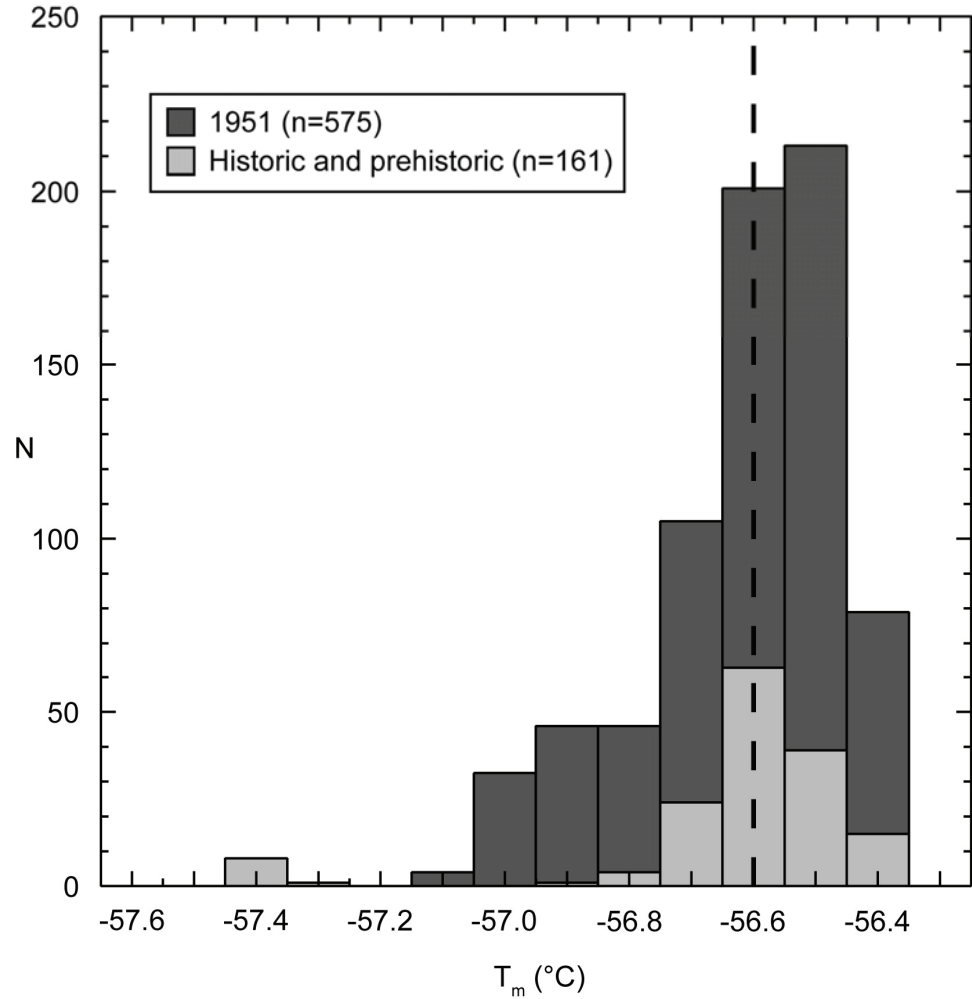


Fig. 8 Measured temperatures of final melting (T_m) of fluid inclusions in olivine and clinopyroxene phenocrysts and xenoliths indicate that most fluids are CO_2 - dominated. Temperatures significantly below the melting temperature of pure CO_2 (-56.6 °C) may indicate the minor presence of components such as N_2 or CH_4 .

Our data indicate that the observed fluid inclusions consist of nearly pure CO_2 . Significant amounts of components other than CO_2 would cause a lowering of T_i and a melting interval rather than a triple point melting (Andersen and Neumann, 2001; Frezzotti et al., 2002). Even if minor amounts of other phases like N_2 or CH_4 were present, these would not significantly affect the interpretation of the PT conditions during fluid trapping (van den Kerkhof, 1990). No evidence for H_2O was found in any observed inclusion although water is expected as a component of volatiles exsolved from basaltic melts (Dixon, 1997). Either former H_2O became lost by hydrogen

diffusion during re-equilibration (Bakker and Jansen, 1991; Hollister, 1990; Mackwell and Kohlstedt, 1990), or reacted with inclusion walls to form secondary minerals (Andersen and Neumann, 2001; Frezzotti et al., 2002). No such reaction rims between fluid inclusions and host mineral could be observed, however.

Homogenization temperatures and densities of fluid inclusions

1951 Eruption

Almost all fluid inclusions ($n = 555$) homogenized into the liquid phase at temperatures between 21.9 and 31.1°C, a few in the dunite fragment of xenolith Fogo 26 ($n = 14$) homogenized into the vapor phase or showed critical homogenization between 28.0 and 31.0° C (Fig. 9a). Systematic differences between primary and secondary inclusion could not be observed, but inclusions in clinopyroxene phenocrysts have a slight trend to higher homogenization temperatures and consequently lower densities than those in olivine phenocrysts (Fig. 9). Similar observations were made in fluid inclusions in rocks of the 1995 Fogo eruption (Hildner et al., 2011) and in volcanic rocks from the Canary Islands (Hansteen et al., 1998; Galipp et al., 2006) and were assigned to olivine being less prone to re-equilibration than clinopyroxene.

Inclusions in olivine phenocrysts from 6 lava samples ($n=217$) homogenized into the liquid phase between 21.9 and 30.7 °C with maxima around 29.0 °C and 25 °C. The homogenization temperatures correspond to a density distribution of 0.55 to 0.75 g/cm³ (90% of data between 0.59 and 0.73 g/cm³). Inclusions in clinopyroxene phenocrysts from 3 lava samples ($n=171$) homogenized into the liquid phase at 26.0 – 30.7 °C, corresponding to a near-Gaussian density distribution between 0.55 and 0.70 g/cm³ with 90% of the data in the narrow range of 0.58-0.69 g/cm³. Compared to phenocrysts, xenolith-hosted inclusions in clinopyroxene ($n=169$) show higher homogenization temperatures between 29.6 and 31.1 °C and lower densities of 0.47-0.61 g/cm³ with 90% of data between 0.51 and 0.59 g/cm³. There is a complete overlap of data for inclusions in clinopyroxene of the dunite and the clinopyroxenite xenolith. Most inclusions in olivine of the dunite xenolith ($n=17$) homogenized into the vapor phase between 28.0 and 31.0 °C; three inclusions homogenized into the liquid phase between 30.4 and 30.8 °C. These temperatures correspond to a density distribution of 0.29-0.58 g/cm³ (Fig. 9b).

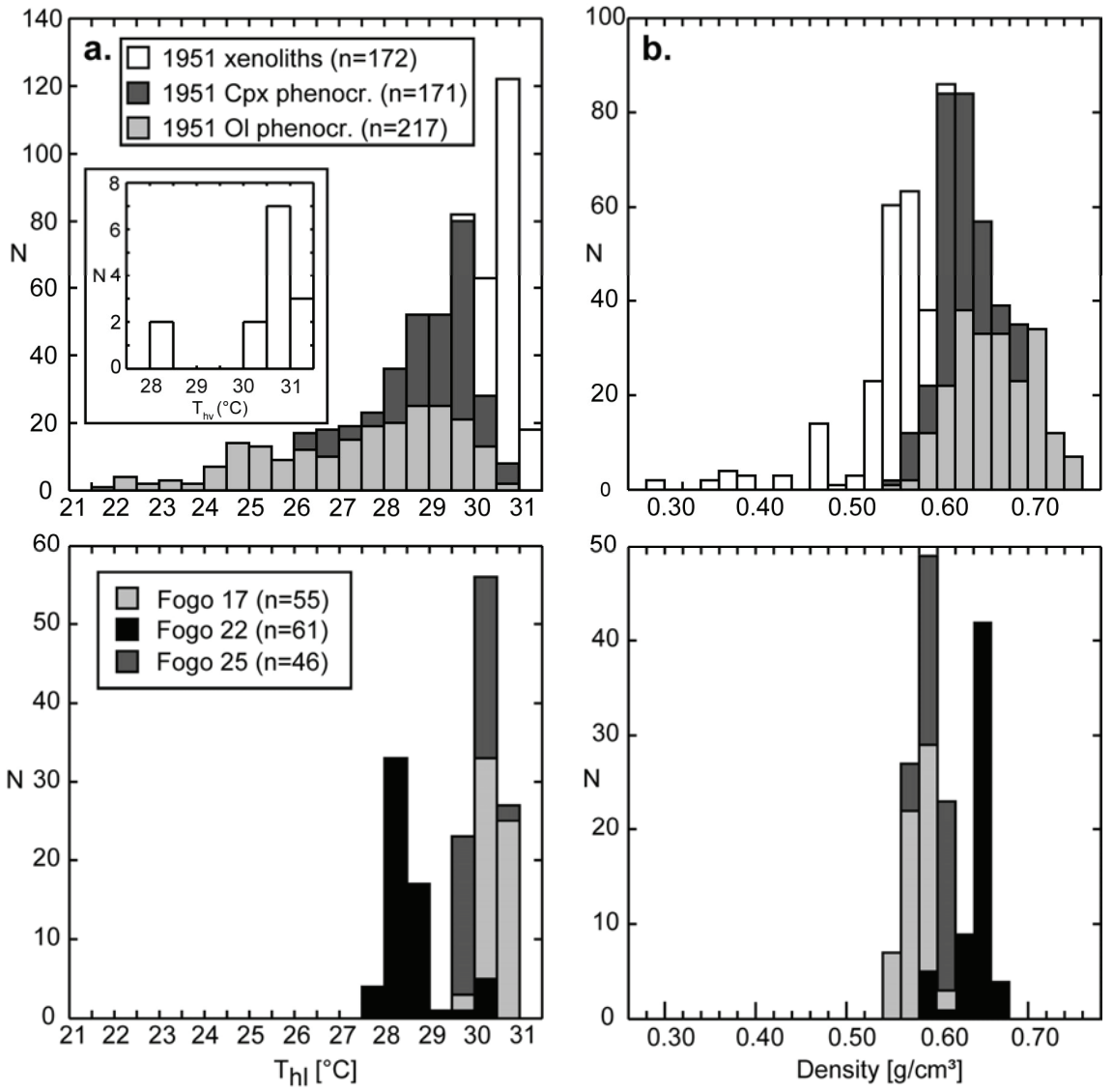


Fig. 9 **a** Measured homogenization temperatures and **b** calculated densities of CO_2 -fluid inclusions. Upper panels show data for olivine and clinopyroxene phenocrysts and xenoliths of the 1951 eruption. Inset in upper left panel shows data of 1951 xenoliths homogenizing into the vapor phase (T_{hv}). Lower panels show data of two xenoliths from the 1785 eruption (Fogo 22 and 25) and from a prehistoric xenolith (Fogo 17). N is the number of studied inclusions.

1785 and prehistoric samples

Primary and secondary fluid inclusions were analyzed in two wehrlite xenoliths (Fogo 22, n=61, and Fogo 25, n=45) from the 1785 eruption, and in one pyroxenite xenolith of near syncollapse age (Fogo 17, n=55). The fluid inclusions of the 1785 xenoliths homogenized into the liquid phase between 27.5 and 30.5 °C corresponding to a narrow density range of 0.57–0.67 g/cm³ (Fig. 9b). No significant difference between inclusions in clinopyroxene and olivine could be observed, but inclusions of Fogo 22 show lower homogenization temperatures and therefore higher densities than those in Fogo 25. Fluid inclusions in clinopyroxene of sample Fogo 17 homogenized between

29.9 and 30.8 °C into the liquid phase, corresponding to densities of 0.54-0.60 g/cm³, with 90% of data in the well-defined range of 0.55-0.59 g/cm³ (Fig. 9b).

Calculated pressures

Pressures of formation or re-equilibration of fluid inclusions were derived from isochores calculated using the equation of state for pure CO₂ of Stern and Pitner (1994). Model temperatures of 1100 °C for all inclusions were chosen, based on the results from clinopyroxene-melt thermometry (Fig. 7). Temperature uncertainties have only minor influence on calculated pressures because of the only moderately positive P-T slopes of the calculated CO₂ isochores. For example, an uncertainty of ± 20 °C would transform into a pressure uncertainty of ± 4-7 MPa for fluid densities between 0.2 and 0.7 g/cm³.

Fluid inclusions in olivine phenocrysts of the 1951 eruption yield a pressure distribution of 250-430 MPa with 90% of data between 270 and 400 MPa (Fig. 10a). Fluid inclusions in clinopyroxene phenocrysts yield a range of 250-370 MPa with 90% of data between 260-360 MPa. Clinopyroxene-hosted inclusions in cumulate xenoliths show a pressure range of 190-290 MPa (90% of data 190-270 MPa), olivine-hosted inclusions yield 100-260 MPa (Fig. 10b).

The fluid inclusion data of the 1951 eruption show that 1) inclusions in olivine phenocrysts yield slightly higher pressures than those in clinopyroxene phenocrysts, although the pressure ranges show a complete overlap; and 2) fluid inclusions in xenoliths yield lower pressures than those in phenocrysts of the host rock. These observations place constraints on the interpretation of fluid inclusion data, as is discussed below.

Fluid inclusions in xenoliths of the 1785 eruption yield a pressure distribution of 260-340 MPa with a range of 260-290 MPa for Fogo 25 and 270-340 MPa for Fogo 22. For the pyroxenite of late pre-collapse age the pressure distribution is 240-280 MPa.

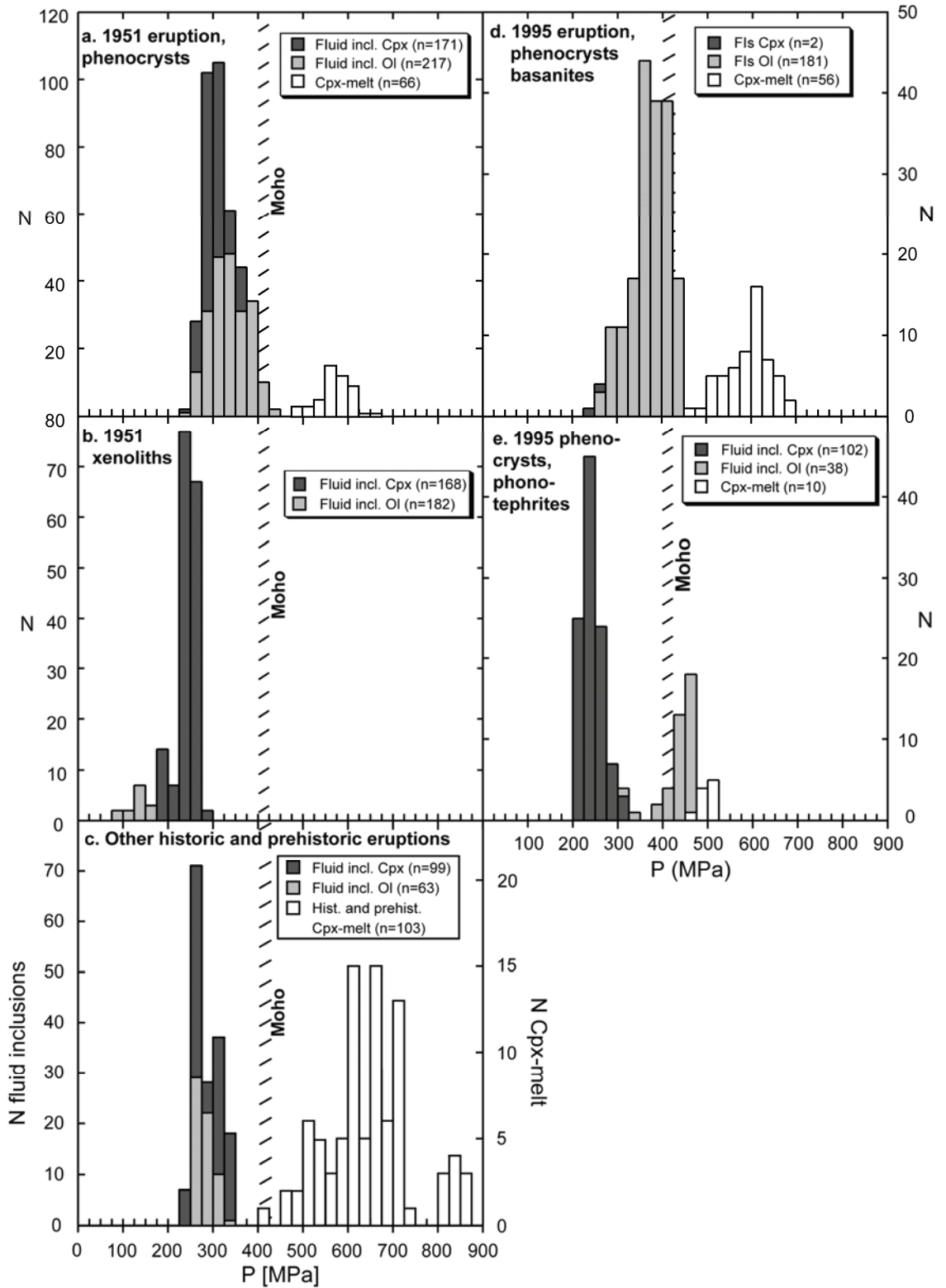


Fig. 10 Calculated pressures derived from fluid inclusion barometry and from clinopyroxene-melt barometry. Each data point of clinopyroxene-melt barometry corresponds to one clinopyroxene phenocryst. **a.** Data of olivine and clinopyroxene phenocrysts of the 1951 eruption. **b.** Xenolith data of 1951. **c.** Data of historic and prehistoric (older than 1680 AD) eruptions. Fluid inclusion data are from clinopyroxene and olivine of xenoliths from 1785 and one of prehistoric age. **d.** and **e.** Data of basanites and phonotephrites of the 1995 eruption (Hildner et al., 2011) for the purpose of comparison. Pressure at Moho depth after the model of Pim et al. (2008).

3.6. Discussion

3.6.1. Interpretation of microthermometric data

Our microthermometric data of fluid inclusions in phenocrysts and xenoliths provide important pressure information but require careful interpretation. The calculated pressures principally represent minimum values for fluid entrapment because post-entrapment modifications during magma ascent (re-equilibration) result in decreasing fluid densities. Re-equilibration can occur in form of stretching, decrepitation (complete or partial leakage), fluid-host mineral reactions, or diffusive loss (summarized in Bodnar, 2003). With the large amount of data for the 1951 eruption, an analysis of the frequency distribution of fluid inclusions (Fig. 9), allows to place constraints on entrapment and re-equilibration conditions.

Observation 1: For phenocrysts of the 1951 eruption, fluid inclusions in olivine yield identical minimum densities as inclusions in clinopyroxene (0.55 g/cm^3), but a broader distribution that extends to higher densities (Fig. 9b). The most plausible explanation for different density distributions of inclusions in co-existing phenocryst phases is different rates of re-equilibration processes. Obviously, re-equilibration of clinopyroxene-hosted inclusions occurred faster and/or more complete than of olivine-hosted inclusions. Similar observations have been made for the lavas from the 1995 Fogo eruption (Hildner et al., 2011), and for lavas from La Palma, Canary Islands (Hansteen et al., 1998; Galipp et al., 2006).

Observation 2: Fluid densities in olivine and clinopyroxene phenocrysts show symmetric, almost Gaussian density distributions. They are not skewed to lower densities (Fig. 9b), as would be expected for inclusion populations that re-equilibrated during comparatively slow decompression (e.g., Vityk and Bodnar, 1998). The data thus indicate magma stalling at a depth represented by the distribution maximum around $0.60\text{-}0.65 \text{ g/cm}^3$ (250-350 MPa; Fig. 10a), where most inclusions could equilibrate to the ambient pressure. Densities above 0.65 g/cm^3 are regarded as incomplete re-equilibration of inclusions formed at higher pressures. Final magma ascent from this stagnation level to the surface must have occurred in a short time, so that re-equilibration of fluid inclusions was limited.

Observation 3: Fluid inclusions observed in clinopyroxenes and olivines of xenoliths from the 1951 eruption yield significantly lower densities and pressures (0.29-0.61

g/cm^3 ; 100-290 MPa) than phenocryst-hosted ones (0.55-0.75 g/cm^3 ; 250-430 MPa). Their density distribution is strongly skewed toward low values, and the maximum around $\sim 0.55 \text{ g}/\text{cm}^3$ coincides with the lowest densities of the phenocrysts. The implications of this observation are discussed in section 6.2.

3.6.2. Depths of stagnation and differentiation of the 1951 magmas

A pronounced feature of our barometric data is the bimodality of pressures calculated by clinopyroxene-melt-barometry (480-650 MPa) and pressures deduced from fluid inclusion microthermometry (250-350 MPa; Fig. 10a). A similar trend to lower pressures of fluid inclusion data has been recognized for the 1995 Fogo eruption (Fig. 10d; Hildner et al., 2011) and by previous studies at other localities (Hansteen et al., 1998; Nikogosian et al., 2002; Schwarz et al., 2004; Klügel et al., 2005). Although fluid inclusion barometry principally yields minimum pressures and this bimodality could thus reflect a systematic bias between the two methods, we interpret this distribution as reflecting real pressure differences for the following reasons:

(1) Uncertainties in the selected model temperature (1100°C) for calculating pressures from fluid inclusion isochores are too small to possibly cause this bias. For a complete overlap with the clinopyroxene-melt barometry data, the model temperatures would have to be unrealistic ($>1500^\circ\text{C}$).

(2) The apparent pressure discrepancy between both methods is outside the prediction error of the clinopyroxene-melt barometer of 130 MPa (derived for a test data set, Putirka et al., 2003). In addition, the reliability of the clinopyroxene-melt barometer for mafic alkaline melts has been demonstrated (Klügel et al., 2005).

(3) A reduction of the original inclusion densities by diffusive loss of H_2O is plausible but cannot cause the observed bias. By correcting for an original H_2O content of 10 mol%, a value typical for fluids exsolved from basaltic melts at 600 MPa (Dixon, 1997; Sachs and Hansteen, 2000), the actual inclusion densities would be 4.5 % higher than the observed (Hansteen and Klügel, 2008). The effect on the calculated pressures would be an increase by mere 20 to 40 MPa.

The main cause for the observed bimodality appears to be the much faster response of fluid inclusions to decompression during magma ascent than clinopyroxene-melt equilibria. Fluid inclusions can re-equilibrate during hours to days at magmatic temperatures (Wanamaker et al., 1990) whereas clinopyroxene rims would require month to years to adapt to changing pressures (Cashman, 1990; Putirka, 1997). For a

magma that experienced prolonged crystal fractionation in the mantle and short-time stagnation at shallower levels during ascent, the two barometric methods would be expected to yield different pressure ranges.

We therefore interpret the pressure range of 480-650 MPa obtained by clinopyroxene-melt barometry to reflect a major fractionation level for the 1951 magmas, characterized by cotectic crystallization of clinopyroxene and olivine phenocrysts. The according depths are 17-22 km, which is in the uppermost lithospheric mantle beneath the Moho (12-14 km, Lodge and Helffrich, 2006; Pim et al., 2008). Our data represent the equilibrium conditions between clinopyroxene rims and host melt, but not necessarily the growth conditions of the often complexly zoned cores. Deeper fractionation levels that are not indicated by the clinopyroxene rims are therefore possible and likely.

The fluid inclusion data of phenocrysts indicate a shallower level around 250-350 MPa (9-13 km depth), where the ascending magma must have stagnated briefly before reaching the surface. This stagnation was presumably on the order of hours to a few days, which was long enough for fluid inclusions in clinopyroxenes (and to a lesser degree in olivines) to re-equilibrate to the reduced pressures, but apparently too short to become recorded by the clinopyroxene rims.

Pressures derived from fluid inclusions in the cumulate xenoliths show little overlap with the postulated stagnation level but extend to significantly shallower levels (100-290 MPa, 4-11 km). The skewness of the density and pressure distributions to lower values (Fig. 9b and 10b) indicates significant but incomplete re-equilibration of the fluid inclusions. The xenoliths most probably have been formed or deposited in the lower crust by earlier magma pulses, and later picked up and brought to the surface by the 1951 magma. We note that the partly pre-deformed and strained xenoliths are more prone to cracking and re-equilibration during decompression than xenocrysts and phenocrysts due to the resulting numerous lattice defects, and the internal stresses developing in crystal aggregates (Hansteen et al., 1998). Some inclusions in xenoliths were therefore able to partly re-equilibrate during final magma ascent to the surface, in contrast to the inclusions in phenocrysts. A co-magmatic origin of the xenoliths in the 1951 magma chamber in the upper mantle appears to be unlikely, because in this case (1) at least a few fluid inclusions should thus indicate appropriate pressures, and (2) inclusions in olivine, regarded to be less prone to re-equilibration than clinopyroxene, should not indicate lower pressures than those in clinopyroxene, as was observed.

3.6.3. Comparison of the 1951 and 1995 magma plumbing systems

A comparison of the pressure distributions derived for the 1951 and 1995 eruptions (Hildner et al., 2011) manifests some apparent similarities (Fig. 10a and d). The pressure ranges obtained by clinopyroxene-melt-barometry for tephrites/ basanites are essentially identical (480-650 MPa and 460-680 MPa for 1951 and 1995, respectively), as are the temperatures (1080-1120 °C and 1070-1125°C). This demonstrates that pre-eruptive crystal fractionation of the 1951 and 1995 magmas occurred at the same depths, possibly but not necessarily in the same reservoir.

The fluid inclusion data show similar results. Inclusions in olivine phenocrysts yield perfect overlap for both 1951 and 1995 basanites (250-430 MPa and 265-440 MPa, respectively), implying similar depths and durations of magma stalling during the 1951 and 1995 eruptions. We conclude that the 1995 and 1951 magma plumbing systems are essentially similar, which may indicate well-established and stable magma pathways from the upper mantle to the surface in recent time.

A distinct feature of the 1951 eruption is the abundance of various cumulate xenoliths and amphibole megacrysts especially during the end of the eruption, which contrasts with the almost complete lack of xenoliths in the 1995 eruption products (Hildner et al., 2011). The well-developed crystal faces of the amphibole megacrysts clearly indicate that they could grow freely in a melt or a crystal mush zone. They most probably represent xenocrysts because they differ in mineralogy and size from the mineral assemblage of the 1951 magma, and are regarded to have grown in a separate, more evolved magma pocket that was disrupted but the late 1951 magma.

3.6.4. Temporal evolution of the magma plumbing system

The clinopyroxene-melt barometric data of pre-1951 lavas show pressure distributions of 420-710 MPa and 450-870 MPa for historic and prehistoric eruptions, respectively (Fig. 10c). These pressures reflect the last equilibrium between clinopyroxene phenocrysts and their host melts. Thus for the investigated eruptions, and probably throughout the entire subaerial evolution of Fogo, the main fractionation levels prior to eruption were located in the uppermost mantle at 15-30 km depth. Even the relatively evolved phonotephrites from the 1995 eruption indicate formation by crystal fractionation in the uppermost mantle (Hildner et al., 2011). The petrologic data thus do

not indicate the former or present existence of long-lived magma chambers within the crust or within the volcanic edifice itself.

A diagram showing the range of inferred fractionation pressures in chronologic order (Fig. 11) depict possible systematic changes in the evolution of Fogo's magma plumbing system. The oldest sample (Fogo 36), an ankaramitic lava flow near the airport of São Filipe, yields the highest pressures (810-870 MPa) of the entire data set. Fogo 37, one of the youngest flows prior to the Monte Amarelo collapse (123 ka; Foeken et al., 2009) and located directly above Fogo 36, yields significantly lower pressures of 530-630 MPa, as does Fogo 16 (450-590 MPa) also of late pre-collapse age. This apparent tendency to shallower fractionation levels seems to be interrupted by the Monte Amarelo flank collapse, because a sample of early post-collapse age indicates comparatively high pressures of 670-730 MPa. The data for historic eruptions cover wider pressure ranges than older eruptions and have a tendency to extend to slightly shallower levels of ~420-500 MPa.

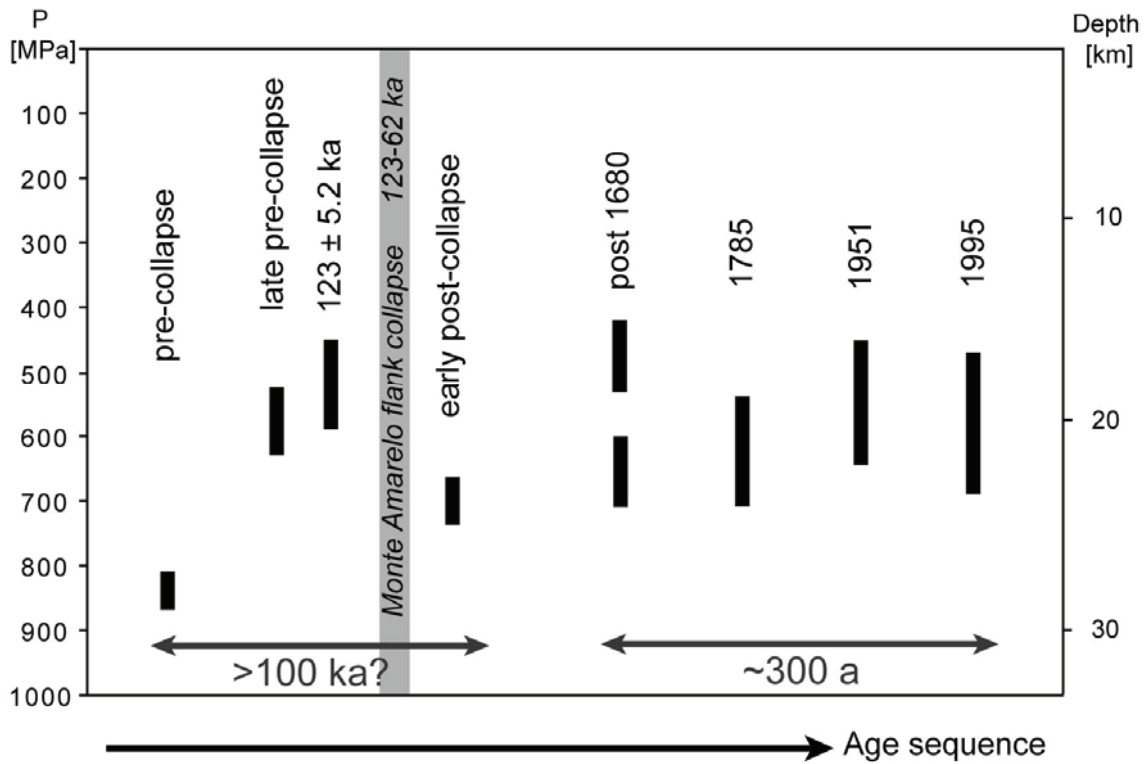


Fig. 11 Pressures calculated by clinopyroxene-melt-barometry arranged in sequential order. Each line represents the calculated pressure range for phenocrysts of one or several samples of the same or similar age. The gray bar marks the Monte Amarelo lateral collapse at 123-62 ka (Foeken et al., 2009). Samples with unknown eruption ages are arranged in stratigraphical order based on field observations. Data of 1995 are from Hildner et al. (2011). Note that the sequential order is not linear in time.

Clinopyroxene phenocrysts also testify to changes in Fogo's magma plumbing system over time: clinopyroxenes of historic eruptions, in particular of the two most recent ones, are more complexly zoned than those of prehistoric eruptions, and more often feature rounded or embayed cores overgrown by equilibrium clinopyroxene. These textures indicate temporary disequilibria between clinopyroxene and host melt, which is most probably caused by mixing of distinct melts and/ or disruption of crystal mush by invading melts. In summary, it appears that the depths of the magma reservoirs feeding Fogo eruptions became slightly shallower and more complex over time. We propose that each Fogo eruption was fed by a relatively small magma pocket in the uppermost mantle rather than by a single persisting magma chamber (Fig. 12). This interpretation is supported by the relatively small volumes of individual eruptions (ca. 0.003-0.01 km³, based on the eruptions of 1951 and 1995). The small sizes of these reservoirs facilitates magma cooling and crystal fractionation, consistent with the low MgO contents of <10 wt.% of most basanites. We suggest that the presumably increased eruption frequency in historic times led to increased formation of ephemeral magma chambers in the uppermost mantle, enabling magma mixing and crystal exchange. Especially the occurrence of resorbed clinopyroxene cores in the historic lavas strongly indicate multi-stage magma evolution including temporary clinopyroxene-melt disequilibrium followed by renewed cotectic clinopyroxene-olivine crystallization. This is in line with investigations of young olivine-nephelinites and olivine-melilitites from the submarine flanks of Fogo, containing abundant green-core pyroxenes interpreted to originate from melts more evolved than the host melts (A. Dürkefälden, T. Hansteen and A. Klügel, unpubl. data.). Similar magma plumbing models have been proposed for the islands of Madeira, La Palma and El Hierro (Schwarz et al., 2004; Galipp et al., 2006; Stroncik et al., 2009). It seems to be a common feature of intraplate volcanic islands in their shield-building stage that the main magma differentiation occurs in the uppermost mantle, unless the magma supply rate is very high as e.g. on Hawaii. Shallow magma chambers can only persist when high supply rates balance cooling and prevent freezing of the magma (Clague and Dixon, 2000). For Fogo and the aforementioned islands, magma storage in the lower crust is limited to brief stalling during eruptions, and plays only a subordinate role for the magma evolution. The stagnation of magma in the lower crust is probably associated with the establishment of a large intrusive complex that has overprinted and partly replaced the pre-existing oceanic crust. Klügel et al. (2005) have proposed a model of magmatic underplating for

La Palma in form of an intrusive complex within the lowermost crust, that is responsible for the observed extensive uplift of the island. Intrusion-related uplift is also regarded to play a major role during the evolution of many Cape Verde islands (Ramalho et al., 2010). Although evidence for significant uplift of Fogo is still lacking, magmatic underplating may be expected, but needs to be tested by future studies of xenoliths and of potential uplift markers.

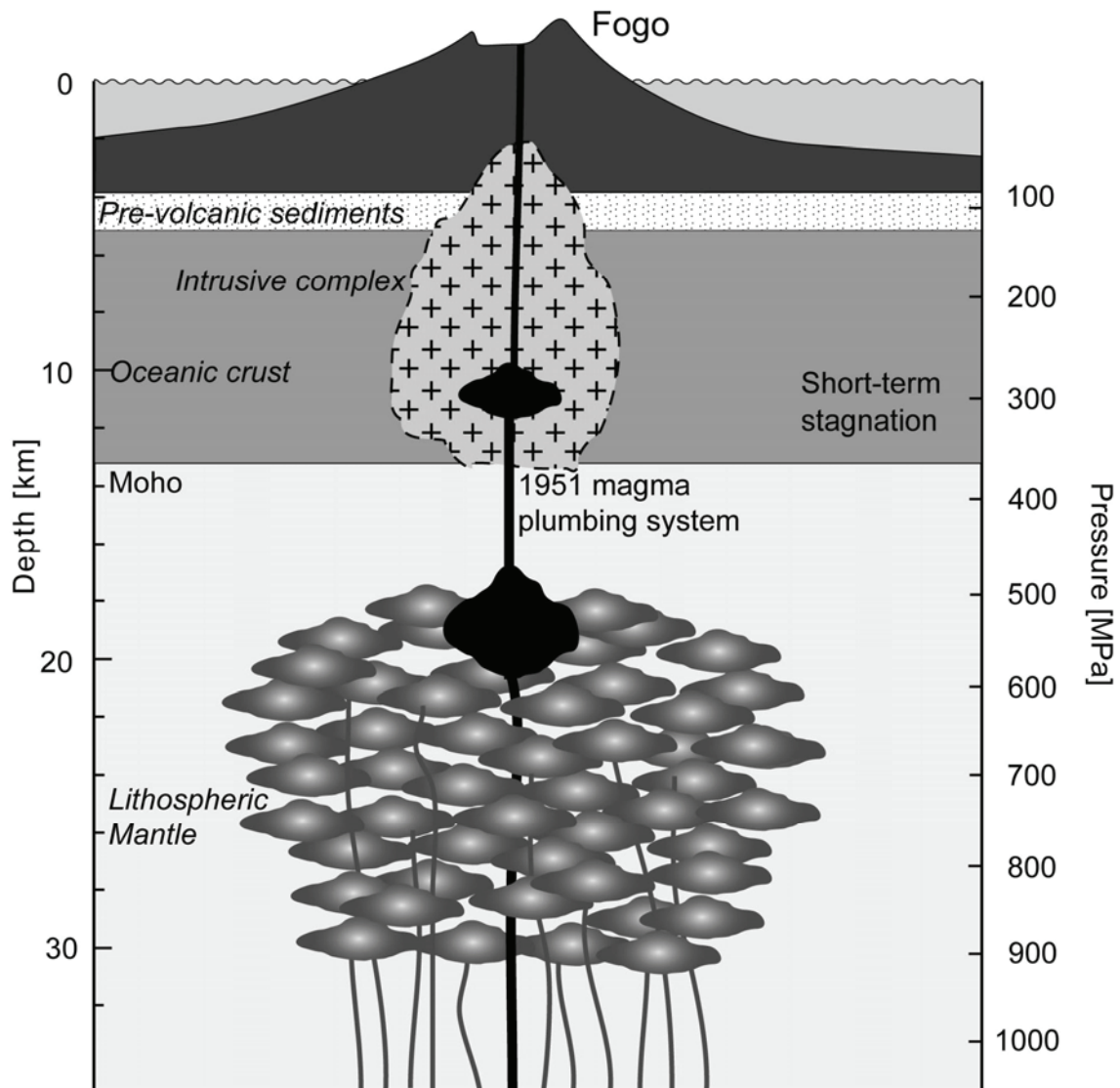


Fig. 12 Model of the plumbing system of the 1951 Fogo eruption. Fractional crystallization prior to eruption took place in 17–22 km depth in the uppermost mantle. Short-time stagnation during final ascent occurred in the lower crust in 9–13 km. A major intrusive body within the crust generated by Fogo-related magmatism is indicated by xenoliths picked up by Fogo magmas in the level of short-time stagnation and above. Fractionation levels of observed historic and prehistoric magmas are located between 15 and 30 km depth. Thicknesses of crustal layers after Pim et al. (2008).

A comparison between Fogo and La Palma (Canary Islands) is worthwhile because they share some apparent similarities: (1) both islands are of similar age, and the historically

most active islands of the respective archipelagos. (2) The Moho is located at similar depths, and the depths of pre-eruptive magma reservoirs are similar (Fogo: 15-30 km, La Palma: 15-34 km). La Palma also shows a trend to shallower reservoirs over time (Galipp et al., 2006). (3) A large lateral collapse ($\sim 200 \text{ km}^3$, Carracedo et al., 2001), comparable to the Monte Amarelo collapse on Fogo, may have interrupted this upward migration trend of fractionation levels on La Palma at 560 ka (Galipp et al., 2006). (4) The younger eruptions on La Palma have a tendency to cover wider pressure ranges (Galipp et al., 2006) as was also observed on Fogo. (5) The lavas of the post-collapse units are on average more differentiated than the older ones on both islands (Kokfelt, 1998; Galipp et al., 2006). (6) Ankaramitic lava flows are common in the units preceding the collapse events on both islands, but seem to lack in the post-collapse units (for Fogo we have to admit that the youngest post-collapse lavas are rarely accessible due to the subsequent infill of the collapse scar). This observation is in contrast to findings for Tenerife and El Hierro, where large lateral collapses were followed by the preferential eruption of more primitive, crystal-rich and denser volcanic rocks (Longpré et al., 2008; Manconi et al., 2009). (7) Ultramafic and mafic cumulate xenoliths, partly hauyne- and titanite-bearing, are common on both islands. However, a major difference between both islands is the common occurrence of phonolites on La Palma but their lack on Fogo.

Large flank collapses such as the Monte Amarelo collapse may sustainably disturb the magma plumbing systems of oceanic island volcanoes even down to upper-mantle depths, e.g. by removal of shallow reservoirs and/ or by disarranging the thermal and mechanical equilibrium of the edifice (Manconi et al., 2009; Amelung and Day 2002). Amelung and Day (2002) found that some volcanic systems having undergone giant collapse events lack shallow magma reservoirs (e.g., Fogo, Piton de la Fournaise) whereas others that exhibit shallow reservoirs lack giant destructive events like e.g. Galápagos Islands (but there are considerable exceptions, like Hawaii and Tenerife, that have experienced large collapses and exhibit shallow magma reservoirs). Their conclusion for Fogo is that the present lack of a current shallow reservoir is largely a consequence of the Monte Amarelo flank collapse; the time period after this event was not long enough to re-establish shallow reservoirs. Our data, however, provide no evidence for Fogo having ever established a persistent magma chamber within the crust or the edifice – neither prior to nor after the flank collapse. Field evidence for ancient shallow magma chambers in form of intrusive complexes is also lacking. We conclude

that the long-time magma supply rate of Fogo is not high enough for a shallow reservoir to establish and persist. Although Fogo, La Palma and the Galápagos Islands have magma supply rates of the same order (Amelung and Day, 2002), they differ in the occurrence of shallow reservoirs and collapse events. We propose that this difference is largely a consequence of the different ages of the oceanic crust underlying the islands and its thermomechanical properties. The Mesozoic crust beneath Fogo (125 Ma, Courtney and White, 1986) and La Palma (ca. 155 Ma; Verhoef et al., 1991) is significantly cooler than the <5 Ma old crust beneath the Galápagos Archipelago (White et al., 1993), which results in stronger heat removal of ascending magmas. For Fogo and La Palma, therefore, significantly higher magma supply rates would be required for the establishment of enduring shallow magma chambers than for Galápagos volcanoes.

3.7. Conclusions

1. Clinopyroxene-melt barometry and CO₂-fluid inclusion data of the 1951 eruption show that major magma fractionation took place at 480-650 MPa, corresponding to 17-22 km depth, in the uppermost mantle. During the eruption the ascending magma temporarily stalled in the lower crust at 250-350 MPa (9-13 km).
2. The magma plumbing system of the 1951 eruption is similar to that of the 1995 eruption. The depths of pre-eruptive magma storage and fractionation, and of short-term stagnation during eruption, are essentially identical.
3. Clinopyroxene-melt barometry of historic and prehistoric Fogo eruptions indicates pre-eruptive magma fractionation in the uppermost mantle at 420-870 MPa (15-30 km). Magmas were stored in the mantle presumably throughout the entire subaerial evolution of Fogo; there is no petrologic evidence for shallow magma chambers in the crust or the volcanic edifice, neither prior to nor after the Monte Amarelo giant flank collapse. The lack of a shallow persistent magma chamber, despite relatively high rates of magma supply, may be a consequence of the cold Mesozoic crust and thick lithosphere beneath Fogo.
4. The evolution of Fogo's magma plumbing system seems to be characterized by a temporal trend to shallower fractionation levels. Fractionation depths in the uppermost mantle decreased significantly during a period of about 100 ka representing a strong growth phase of the Fogo edifice leading up to the Monte Amarelo flank collapse at 123-62 ka. This depth decrease with time seems to have been interrupted by the flank

collapse, as early post-collapse magmas stagnated at deeper levels than late pre-collapse ones. Historic eruptions fractionated at shallower levels and show broader pressure ranges, indicating an increase in complexity of the magma storage systems, probably related to increased eruption frequencies in historical times.

3.8. Acknowledgements

Our field work on Fogo would not have been possible without the support by Simon Day, Bruno Faria, José Antonio, and the Cape Verde Ministério do Ambiente e Agricultura / Parque Natural do Fogo. We thank Simon Day, Thomas Kokfelt, Ricardo Ramalho and Abigail Barker for stimulating discussions and help, and Mario Thöner, Heike Anders, Daniel Schwander, Stefan Jung and Elisabeth Thun for analytical support. This study was supported by the Deutsche Forschungsgemeinschaft (DFG grants KL1313/9 and HA2100/12)

Electronic supplementary material

The electronic supplementary material of this paper is presented in the printed Appendix of the thesis (A1-A3).

3.9. References

- Amelung, F. and Day, S., 2002. InSAR observations of the 1995 Fogo, Cape Verde, eruption: implications for the effects of collapse events upon island volcanoes. *Geophys. Res. Lett.* 29(12). doi: 10.1029/2001GL013760.
- Andersen, T. and Neumann, E., 2001. Fluid inclusions in mantle xenoliths. *Lithos* 55, 301-320.
- Angus, S., Armstrong, B., de Reuck, K., Altunin, V., Gadetskii, O., Chapela, G. and Rowlinson, J., 1976. International tables of fluid state, vol. 3, carbon dioxide. Pergamon Press, Oxford, pp. 1-385.
- Bakker, R. and Jansen, J., 1991. Experimental post-entrapment water loss from synthetic CO₂-H₂O inclusions in natural quartz. *Geochim. Cosmochim. Acta* 55, 2215-2230.
- Bodnar, R., 2003. Re-equilibration of fluid inclusions. In: Samson, I., Anderson, A. and Marshall, D. (Eds.), *Fluid inclusions: analysis and interpretation*. Mineral. Assoc. Can., Short Course Ser. 32, 213-230.
- Brum da Silveira, A., Madeira, J. and Serralheiro, A., 1997. A estrutura da Ilha do Fogo, Cabo Verde. In: Réffega, A., Figueiredo, M., Silva, L., Costa, F., Mendes, M., Torres, P., da Silva, T. and Correia, E. (Eds.), *A erupção vulcânica de 1995 na Ilha do Fogo, Cabo Verde*. Ministério da Ciencia e da Tecnologia, Instituto de Investigação Científica Tropical, Lisbon, pp. 63-78.
- Carracedo, J.C., Badiola, E., Guillou, H., de la Nuez, J. and Pérez Torrado, F., 2001. Geology and volcanology of La Palma and El Hierro, Western Canaries. *Estudios Geol.* 57, 175-273.
- Cashman, K.V., 1990. Textural constraints on the kinetics of crystallization of igneous rocks. *Rev. Mineral.* 24, 259-314.
- Clague, D.A. and Dixon, J.E., 2000. Extrinsic controls on the evolution of Hawaiian ocean island volcanoes. *Geochem. Geophys. Geosyst.* 1(4), 1-9.
- Courtney, R.C. and White, R.S., 1986. Anomalous heat-flow and geoid across the Cape-Verde rise - evidence for dynamic support from a thermal plume in the mantle. *Geophys. J. Int.* 87(3), 815-867.
- Day, S.J., Carracedo, J., Guillou, H., Pais Pais, F., Rodriguez Badiola, E., Fonseca, J. and Heleno da Silva, S., 2000. Comparison and cross-checking of historical, archaeological and geological evidence for the location and type of historical and sub-historical eruptions of multiple-vent oceanic island volcanoes. In: McGuire, W., Griffiths, D., Hancock, P. and Stewart, I. (Eds.), *The archaeology of geological catastrophes*. Geological Society, London, Special Publications, London, pp. 281-306.
- Day, S.J., Heleno da Silva, S. and Fonseca, J., 1999. A past giant lateral collapse and present-day flank instability of Fogo, Cape Verde Islands. *J. Volcanol. Geotherm. Res.* 94, 191-218.
- Dixon, J., 1997. Degassing of alkalic basalts. *Am. Mineral.* 82, 368-378.
- Doucelance, R., Escrig, S., Moreira, M., Gariepy, C. and Kurz, M., 2003. Pb-Sr-He isotope and trace element geochemistry of the Cape Verde Archipelago. *Geochim. Cosmochim. Acta* 67(19), 3717-3733.
- Duke, J., 1976. Distribution of the period four transition elements among olivine, calcic clinopyroxene and mafic silicate liquid: experimental results. *J. Petrol.* 17(4), 499-521.
- Elsworth, D. and Day, S.J., 1999. Flank collapse triggered by intrusion: the Canarian and Cape Verde Archipelagoes. *J. Volcanol. Geotherm. Res.* 94, 323-340.
- Escríg, S., Doucelance, R., Moreira, M. and Allègre, C., 2005. Os isotope systematics in Fogo Island: evidence for lower continental crust fragments under the Cape Verde southern islands. *Chem. Geol.* 219, 93-113.

- Foeken, J., Day, S. and Stuart, F., 2009. Cosmogenic ^{3}He exposure dating of the Quaternary basalts from Fogo, Cape Verdes: implications for rift zone and magmatic reorganisation. *Quat. Geochronol.* 4, 37-49.
- Frezzotti, M., Andersen, T., Neumann, E. and Simonsen, S., 2002. Carbonatite melt- CO_2 fluid inclusions in mantle xenoliths from Tenerife, Canary Islands: a story of trapping, immiscibility and fluid-rock interaction in the upper mantle. *Lithos* 64, 77-96.
- Galipp, K., Klügel, A. and Hansteen, T.H., 2006. Changing depths of magma fractionation and stagnation during the evolution of an oceanic island volcano: La Palma (Canary Islands). *J. Volcanol. Geotherm. Res.* 155(3-4), 285-306.
- Garcia, M.O., Ho, R.A., Rhodes, J.M. and Wolfe, E.W., 1989. Petrologic constraints on rift-zone processes. *Bull. Volcanol.* 52(2), 81-96.
- Geldmacher, J., Hoernle, K., Van Den Bogaard, P., Hauff, F. and Klügel, A., 2008. Age and geochemistry of the Central American forearc basement (DSDP Leg 67 and 84): insights into Mesozoic arc volcanism and seamount accretion on the fringe of the Caribbean LIP. *Journal of Petrology*, 49(10), 1781-1815.
- Gerlach, D., Cliff, R., Davies, G., Norry, M. and Hodgson, N., 1988. Magma sources of the Cape Verdes archipelago: Isotopic and trace element constraints. *Geochim. Cosmochim. Acta* 52, 2979-2992.
- Hansteen, T.H., Klügel, A. and Schmincke, H.-U., 1998. Multi-stage magma ascent beneath the Canary Islands: evidence from fluid inclusions. *Contrib. Mineral. Petrol.* 132, 48-64.
- Hansteen, T.H. and Klügel, A., 2008. Fluid inclusion thermobarometry as a tracer for magmatic processes. In: Putirka, K. and Tepley III, F. (Eds.) Minerals, inclusions and volcanic processes. *Rev. Mineral.* 69, 142-177.
- Hildner, E., Klügel, A. and Hauff, F., 2011. Magma storage and ascent during the 1995 eruption of Fogo, Cape Verde Archipelago. *Contrib. Mineral. Petrol.* doi: 10.1007/s00410-011-0623-6.
- Hollister, L., 1990. Enrichment of CO_2 in fluid inclusions in quartz by removal of H_2O during crystal-plastic deformation. *J. Struct. Geol.* 12(7), 895-901.
- Holm, P.M., Grandvoinet, T., Friis, J., Wilson, J.R., Barker, A.K. and Plesner, S., 2008. An $40\text{Ar}-39\text{Ar}$ study of the Cape Verde hot spot: temporal evolution in a semistationary plate environment. *J. Geophys. Res.* 113(B8), B08201.
- Kerrick, D.M. and Jacobs, G.K., 1981. A modified Redlich-Kwong equation for H_2O , CO_2 , and $\text{H}_2\text{O}-\text{CO}_2$ mixtures at elevated pressures and temperatures. *Am. J. Sci.* 281(6), 735-767.
- Klügel, A., Hoernle, K.A., Schmincke, H.-U. and White, J.D.L., 2000. The chemically zoned 1949 eruption on La Palma (Canary Islands): petrologic evolution and magma supply dynamics of a rift zone eruption. *J. Geophys. Res.* 105(B3), 5997-6016.
- Klügel, A., Hansteen, T.H. and Galipp, K., 2005. Magma storage and underplating beneath Cumbre Vieja volcano, La Palma (Canary Islands). *Earth Planet. Sci. Lett.* 236, 211-226.
- Kokfelt, T., 1998. A geochemical and isotopic study of the Island of Fogo, the Cape Verde Islands, University of Copenhagen, Copenhagen, 164 pp.
- Lodge, A. and Helffrich, G., 2006. Depleted swell root beneath the Cape Verde Islands. *Geology* 34, 449-452.
- Longpré, M.-A., Troll, V. and Hansteen, T.H., 2008. Upper mantle magma storage and transport under a Canarian shield-volcano, Teno, Tenerife (Spain). *J. Geophys. Res.* 113(B08203).
- Longpré, M.-A., Troll, V.R., Walter, T.R. and Hansteen, T.H., 2009. Volcanic and geochemical evolution of the Teno massif, Tenerife, Canary Islands: some repercussions of giant landslides on ocean island magmatism. *Geochem. Geophys. Geosyst.* 10(12), Q12017.

- Mackwell, S.J. and Kohlstedt, D.L., 1990. Diffusion of hydrogen in olivine - implications for water in the mantle. *J. Geophys. Res. Solid* 95(B4), 5079-5088.
- Manconi, A., Longpré, M.-A., Walter, T.R., Troll, V.R. and Hansteen, T.H., 2009. The effects of flank collapses on volcano plumbing systems. *Geology* 37(12), 1099-1102.
- Masson, D., Watts, A., Gee, M., Urgeles, R., Mitchell, N., Le Bas, T. and Canals, M., 2002. Slope failures on the flanks on the western Canary Islands. *Earth Sci. Rev.* 57, 1-35
- McGuire, W.J., 1996. Volcano instability: a review of contemporary themes. Geological Society, London, Special Publications, 110(1), 1-23.
- Munhá, J., Mendes, M., Palácios, T., Silva, L. and Torres, P., 1997. Petrologia e geoquímica da erupção de 1995 e de outras lavas históricas na Ilha do Fogo, Cabo Verde. In: Réffega, A., Figueiredo, M., Silva, L., Costa, F., Mendes, M., Torres, P., da Silva, T. and Correia, E. (Eds.), A erupção vulcânica de 1995 na Ilha do Fogo, Cabo Verde. Ministério da Ciencia e da Tecnologia, Instituto de Investigação Científica Tropical, Lisbon, pp. 171-186.
- Nikogosian, I., Elliott, T. and Touret, J., 2002. Melt evolution beneath thick lithosphere: a magmatic inclusion study of La Palma, Canary Islands. *Chem. Geol.* 183, 169-193.
- Pim, J., Peirce, C., Watts, A., Grevemeyer, I. and Krabbenhoeft, A., 2008. Crustal structure and origin of the Cape Verde rise. *Earth Planet. Sci. Lett.* 272, 422-428.
- Presley, T.K., Sinton, J.M. and Pringle, M., 1997. Postshield volcanism and catastrophic mass wasting of the Waianae volcano, Oahu, Hawaii. *Bull. Volcanol.* 58(8), 597-616.
- Putirka, K., 1997. Magma transport at Hawaii: inferences based on igneous thermobarometry. *Geology* 25(1), 69-72.
- Putirka, K., 1999. Clinopyroxene + liquid equilibria to 100 kbar and 2450 K. *Contrib. Mineral. Petrol.* 135, 151-163.
- Putirka, K., Mikaelian, H., Ryerson, F. and Shaw, H., 2003. New clinopyroxene-liquid thermobarometers for mafic, evolved, and volatile-bearing lava compositions, with applications to lavas from Tibet and the Snake River Plain, Idaho. *Am. Mineral.* 88, 1542-1554.
- Ramalho, R., Helffrich, G., Schmidt, D. and Vance, D., 2010. Tracers of uplift and subsidence in the Cape Verde archipelago. *J. Geol. Soc. London* 167, 1-19.
- Ribeiro, O., 1960. A Ilha do Fogo e as suas erupções, 2nd edn (The island of Fogo and its eruptions). Memorias, serie geographica I. Junta de Investigacões do Ultramar, Ministerio do Ultramar, Lisbon.
- Roedder, E., 1984. Fluid inclusions. *Rev. Mineral.* 12, 644 Washington.
- Sachs, P. and Hansteen, T.H., 2000. Pleistocene underplating and metasomatism of the lower continental crust: a xenolith study. *J. Petrol.* 41(3), 331-356.
- Schwarz, S., Klügel, A. and Wohlgemuth-Ueberwasser, C., 2004. Melt extraction pathways and stagnation depths beneath the Madeira and Desertas rift zones (NE Atlantic) inferred from barometric studies. *Contrib. Mineral. Petrol.* 147, 228-240.
- Span, R. and Wagner, W., 1996. A new equation of state for carbon dioxide covering the fluid region from the triple-point temperature to 1100 K at pressures up to 800 MPa. *J. Phys. Chem. Ref. Data* 25(6), 1509-1596.
- Sterner, S. and Pitzer, K., 1994. An equation of state for carbon dioxide valid from zero to extreme pressures. *Contrib. Mineral. Petrol.* 117, 362-374.
- Sun, S.-s. and McDonough, W., 1989. Chemical and isotopic systematics of oceanic basalts: implications for mantle composition and processes. In: Saunders, A. and Norry M. (Eds.), Magmatism in the ocean basins, pp. 313-345.

- Stroncik, N., Klügel, A. and Hansteen, T., 2009. The magmatic plumbing system beneath El Hierro (Canary Islands): constraints from phenocrysts and naturally quenched basaltic glasses in submarine rocks. *Contrib. Mineral. Petrol.* 157(5), 593-607.
- Tilling, R.I. and Dvorak, J.J., 1993. Anatomy of a basaltic volcano. *Nature* 363(6425), 125-133.
- Torres, P., Madeira, J., Silva, L., Brum da Silveira, A., Serralheiro, A. and Mota Gomes, A., 1997. Carta geológica das erupções históricas da Ilha do Fogo: revisão e actualização. In: Réffega, A., Figueiredo, M., Silva, L., Costa, F., Mendes, M., Torres, P., da Silva, T. and Correia, E. (Eds.), A erupção vulcânica de 1995 na Ilha do Fogo, Cabo Verde. Ministério da Ciencia e da Tecnologia, Instituto de Investigação Científica Tropical, Lisbon, pp. 119-132.
- van den Kerkhof, A., 1990. Isochoric phase diagrams in the systems CO₂-CH₄ and CO₂-N₂: application to fluid inclusions. *Geochim. Cosmochim. Acta* 54, 621-629.
- Verhoef, J., Collette, B.J., Dañobeitia, J.J., Roeser, H.A. and Roest, W.R., 1991. Magnetic anomalies off West-Africa (20–38° N). *Mar. Geophys. Res.* 13(2), 81-103.
- Vidal, N. and Merle, O., 2000. Reactivation of basement faults beneath volcanoes: a new model of flank collapse. *J. Volcanol. Geotherm. Res.* 99(1-4), 9-26.
- Vityk, M.O. and Bodnar, R.J., 1998. Statistical microthermometry of synthetic fluid inclusions in quartz during decompression reequilibration. *Contrib. Mineral. Petrol.* 132(2), 149-162.
- Voight, B. and Elsworth, D., 1997. Failure of volcano slopes. *Geotechnique* 47(1), 1-31.
- Wanamaker, B., Wong, T.-F. and Evans, B., 1990. Decrepitation and crack healing of fluid inclusions in San Carlos olivine. *J. Geophys. Res.* 95(B10), 15623-15641.
- White, W.M., McBirney, A.R. and Duncan, R.A., 1993. Petrology and geochemistry of the Galápagos Islands: portrait of a pathological mantle plume. *J. Geophys. Res.*, 98(B11), 19533-19563.

IV Synthesis and Outlook

Synthesis

The present thesis provides insight into the magma plumbing systems of Fogo and represents the first comprehensive barometric approach for a volcanic system of the Cape Verde Archipelago. Clinopyroxene-melt barometric data show that major magma differentiation before eruption takes place in the uppermost mantle in 15-30 km depth throughout the subaerial evolution of Fogo. Syn-eruptive short-term magma stagnation occurs in the lower crust in 8-13 km depth as indicated by fluid inclusion barometric data for the two most recent eruptions of 1995 and 1951. Short-term magma stagnation may be induced by density contrasts caused by intrusive complexes and crystal mush zones within the crust that are suggested by cumulate xenoliths in historic lavas. The magma plumbing systems of 1951 and 1995 appear essentially identical. The differences in the locations and especially the orientations of the eruption fissures appear to be related to changing properties of the regional stress field of the steep volcanic edifice rather than to deep-seated features of the magma plumbing systems.

Several geophysical hypotheses regarding the 1995 eruption and the evolution of the magma plumbing system were tested successfully: (1) The determined depth >16.5 km of the 1995 magma chamber based on the analysis of satellite-derived interferograms (Amelung and Day 2002) was approved by the petrologic data that indicate 16-24 km depth. (2) No petrologic or geochemical evidence was found for pre- or syn-eruptive lateral magma movements beneath the Fogo-Brava platform during the 1995 eruption as was suggested by seismic studies (Heleno da Silva et al. 1997; Heleno and Fonseca 1999; Heleno 2003). The phonotephrites and basanites ejected during the 1995 are related by crystal fractionation; contamination by Brava phonolites is not indicated. (3) Amelung and Day (2002) proposed a persistent shallow magma chamber for the Monte Amarelo volcano that has been removed by the lateral collapse. However, no petrologic evidence for shallow magma chambers before the collapse and even throughout Fogo's subaerial evolution was found.

The magma plumbing systems of Fogo show a temporal trend to shallower magma differentiation levels during a period of more than 100 ka. This trend seems to have been interrupted by the Monte Amarelo collapse, since an early post-collapse magma stagnated at a deeper level than the late pre-collapse ones. Historic eruptions show

shallower differentiation depths and broader pressure ranges which indicates an increase in complexity of the magma storage systems.

The characteristics of Fogo's magma plumbing systems and their temporal evolution fit well in the context of other eastern Atlantic volcanic archipelagos off West-Africa, such as the Canary Islands and Madeira Archipelago. During the shield-building stages, major magma stagnation and differentiation typically occurs in the upper lithospheric mantle and to a lesser amount in the lower crust in 10-45 km depth (e.g. Hansteen et al. 1998; Schwarz et al. 2004; Klügel et al. 2005; Galipp et al. 2006; Longpré et al. 2008; Stroncik et al. 2009). Shallow crustal magma chambers are not common for those islands, although there are exceptions in terms of Tenerife and Gran Canaria (Canary Islands) that both have developed enduring shallow reservoirs after the major shield-building phase (e.g. Ablay et al. 1998; Schmincke and Sumita 2011). Another common feature seems to be short-term magma stagnation around the Moho and within the lower crust, which was observed, beside Fogo, at La Palma and Madeira (Schwarz et al. 2004; Klügel et al. 2005; Galipp et al. 2006).

Especially La Palma (Canary Islands), where numerous barometric and petrologic data, and age determinations are available (e.g. Ancochea et al. 1994; Klügel et al. 2000; Klügel et al. 2005; Galipp et al. 2006 and references therein), shows manifold analogies with Fogo. Both islands are of similar age, both are located at the western end and represent the historically most active islands of the respective archipelagos. The Moho is located at similar depths and the characteristics of the magma plumbing systems are similar. A trend to shallower magma differentiation levels was observed for La Palma and Fogo, and both islands have experienced large flank collapses that temporarily interrupted the upward migration trend of magma reservoirs. The lavas of the post-collapse units of both islands are on average more differentiated than those of the older units. Ankaramitic lavas are common in the units preceding the collapses, but seem to lack in the post-collapse rocks. This is in contrast to observations on Tenerife and El Hierro, where large lateral collapses were followed by the predominant eruption of more primitive, crystal-rich and denser lavas (Longpré et al. 2008; Manconi et al. 2009). Ultramafic and mafic cumulate xenoliths are common on both Fogo and La Palma. A major difference of both islands is, however, the common occurrence of phonolites on La Palma whereas they are very rare on Fogo.

The similar characteristics of the magma plumbing systems of the eastern Atlantic volcanic archipelagos are in contrast to other oceanic intra-plate volcanic provinces

such as Hawaii and Galápagos. Hawaiian volcanoes in their shield building stages commonly develop enduring shallow magma reservoirs below large summit calderas. Those reservoirs feed well-established rift zones where magma can be temporarily stored and remobilized by subsequently ascending magmas (e.g. Garcia et al. 1989, Tilling and Dvorak 1993, Walker 1999). The tapping of deeper magma reservoirs stored over a range of depths in the crust and the lithospheric mantle is indicated during sustained eruptions (Putirka 1997). Magma stagnation and differentiation on Galápagos archipelago is multi-faceted. Magmas of the central volcanoes that lack summit calderas differentiate in transient magma chambers in the uppermost mantle. The volcanoes of the western island experience magma differentiation in the crust; deep summit calderas are underlain by very shallow magma reservoirs whereas broad, shallow calderas are associated with magma differentiation in the lower crust (Geist et al. 1998).

The differences in the characteristics and developments of the magma plumbing systems of the eastern Atlantic archipelagos, Hawaii and the Galápagos Islands are presumably related to the distinct structural settings and thermomechanic properties of the underlying mantle and crust. The high magma supply rates of Hawaiian volcanoes compensate heat loss of ascending magmas in the crust and therefore allow the establishment of enduring shallow magma chambers (Clague 1987). The magma supply rates of the eastern Atlantic volcanoes are low compared to those of Hawaii (Carracedo 1999), which seems to prevent the development of shallow reservoirs. Galápagos volcanoes have magma supply rates of a similar order than Fogo and the Canary Islands (Amelung and Day 2002); nonetheless shallow magma chambers are common at least at the western Galápagos Islands. This difference is mainly a consequence of the different thermomechanic properties of the underlying lithosphere and crust that are principally a function of their respective age. The Mesozoic crust and lithosphere beneath the eastern Atlantic archipelagos (e.g. 155 Ma for La Palma, Verhoef et al. 1991; 125 Ma for Fogo, Courtney and White 1986) are significantly cooler than the <5 Ma old crust beneath the Galápagos Archipelago (White et al. 1993), which results in stronger heat removal of the ascending melts. For Fogo and La Palma higher magma supply rates would be required to allow the establishment of enduring shallow reservoirs than for the Galápagos Islands.

This thesis presents comprehensive insight into the magma plumbing systems and the magma ascent dynamics of historic eruptions of Fogo, and therefore supplies essential information for the ongoing geophysical monitoring and hazard assessment activities

(VIGIL monitoring network, Fonseca et al. 2003) with respect to future eruptions. For the first time geophysical hypotheses based on seismic and ground deformation data of pre- and syneruptive magma movement and ascent were tested by petrologic studies of the respective eruption products. The petrologic data indicate that during Fogo eruptions, magmas ascend from upper mantle depths to the surface within hours to days, including short-term stagnation within the lower crust. However, the dynamics and timing of pre-eruptive magma ascent by dike propagation are not known, but the lead times for future eruptions in form of pre-eruptive seismicity and volcanic tremor will be presumably short. Future eruptions are expected to occur not at the summit of Pico, but from fissures at its flanks and sparsely within the Cha das Caldeiras plain. Depending on the locality of future eruption fissures, the two villages in Cha das Caldeiras and their inhabitants may become affected by lava flows, fall out or hazardous volcanic gasses. In the worst case of emergency the evacuation of up to 1000 inhabitants must be organized immediately.

Outlook

This thesis represents an important piece of the puzzle in the geoscientific and especially petrologic exploration of Fogo and the Cape Verde Archipelago. Although the objectives of this work were addressed successfully, numerous questions and issues regarding the magmatic evolution of Fogo and the archipelago and presumable future developments remain still open. In the following some potentially important issues of future research are summarized:

- Detailed petrologic and geochemical investigations of the prehistoric volcanic units of Fogo, especially the Monte Amarelo Group that represents by far the main volume of the subaerial edifice, is still missing. More barometric and geochemical data are required to constrain the observed trend of changing depths of magma differentiation and the influence of the Monte Amarelo flank collapse on the evolution of the volcanic system.
- In regard of exploring the triggering mechanisms and the course of action of the Monte Amarelo collapse, detailed studies of late pre-collapse and early post-collapse lavas are required. Such an approach would additionally deliver important data for the assessment and dynamics of expected future flank instabilities, and for the ongoing monitoring activities.
- Detailed xenolith studies would allow further insights into the evolution of the magma plumbing systems of Fogo and of assumed intrusive complexes and crystal mush zones within the upper mantle, the crust and the volcanic edifice.
- Petrologic and barometric investigations of volcanic rocks of the submarine flanks of Fogo and especially of the group of active submarine volcanoes between Fogo and Brava would unravel the relations between seismicity and magma pathways beneath the Fogo-Brava platform.

References

- Ablay GJ, Carroll MR, Palmer MR, Martí J and Sparks RSJ (1998) Basanite–phonolite lineages of the Teide–Pico Viejo volcanic complex, Tenerife, Canary Islands. *J Petrol* 39(5):905–936
- Amelung F and Day S (2002) InSAR observations of the 1995 Fogo, Cape Verde, eruption: implications for the effects of collapse events upon island volcanoes. *Geophys Res Lett*, 29(12):GL013760
- Ancochea E, Hernán F, Cendrero A, Cantagrel JM, Fúster J, Ibarrola E and Coello J (1994) Constructive and destructive episodes in the building of a young oceanic island, La Palma, Canary Islands, and genesis of the Caldera de Taburiente. *J Volcanol Geotherm Res* 60(3–4):243–262
- Barker AK, Holm PM, Peate DW and Baker JA (2009) Geochemical stratigraphy of submarine lavas (3–5 Ma) from the Flamengos Valley, Santiago, Southern Cape Verde Islands. *J Petrol* 50(1):169–193
- Carracedo J (1999) Growth, structure, instability and collapse of Canarian volcanoes and comparisons with Hawaiian volcanoes. *J Volcanol Geotherm Res* 94:1–19
- Clague D (1987) Hawaiian xenolith populations, magma supply rates, and development of magma chambers. *Bull Volcanol* 49:577–587
- Clague DA and Dixon JE (2000) Extrinsic controls on the evolution of Hawaiian ocean island volcanoes. *Geochem Geophys Geosyst*, 1(4):1–9
- Courtney RC and White RS (1986) Anomalous heat-flow and geoid across the Cape-Verde Rise – evidence for dynamic support from a thermal plume in the mantle. *Geophys J Int* 87(3):815–867
- Day SJ, Heleno da Silva S and Fonseca J (1999) A past giant lateral collapse and present-day flank instability of Fogo, Cape Verde Islands. *J Volcanol Geotherm Res* 94:191–218
- Day SJ, Carracedo J, Guillou H, Pais Pais F, Rodriguez Badiola E, Fonseca J and Heleno da Silva S (2000) Comparison and cross-checking of historical, archaeological and geological evidence for the location and type of historical and sub-historical eruptions of multiple-vent oceanic island volcanoes. In: McGuire W, Griffiths D, Hancock P and Stewart I (eds) *The archaeology of geological catastrophes*. Geological Society, London, Special Publications, London, pp 281–306
- Elsworth D and Day SJ (1999) Flank collapse triggered by intrusion: the Canarian and Cape Verde Archipelagoes. *J Volcanol Geotherm Res* 94:323–340
- Foeken J, Day S and Stuart F (2009) Cosmogenic ^{3}He exposure dating of the Quaternary basalts from Fogo, Cape Verdes: implications for rift zone and magmatic reorganisation. *Quat Geochronol* 4:37–49
- Fonseca J, Faria B, Lima N, Heleno da Silva S, Lazaro C, d'Oreye N, Ferreira A, Barros I, Santos P, Bandomo Z, Day SJ, Osorio J, Baio M and Matos J (2003) Multiparameter monitoring of Fogo Island, Cape Verde, for volcanic risk mitigation. *J Volcanol Geotherm Res* 125:39–56
- Galipp K, Klügel A and Hansteen TH (2006) Changing depths of magma fractionation and stagnation during the evolution of an oceanic island volcano: La Palma (Canary Islands). *J Volcanol Geotherm Res* 155(3–4):285–306
- Garcia MO, Ho RA, Rhodes JM and Wolfe EW (1989) Petrologic constraints on rift-zone processes. *Bull Volcanol* 52(2):81–96
- Geist D, Naumann T and Larson P (1998) Evolution of Galápagos magmas: mantle and crustal fractionation without assimilation. *J Petrol* 39(5):953–971
- Geist D, White W, Naumann T and Reynolds R (1999) Illegitimate magmas of the Galápagos: insights into mantle mixing and magma transport. *Geology* 27(12):1103–1106
- Hansteen TH, Klügel A and Schmincke H-U (1998) Multi-stage magma ascent beneath the Canary Islands: evidence from fluid inclusions. *Contrib Mineral Petrol* 132:48–64

- Heleno da Silva S, Foulger G, Barros I, Querido A, Walker A and Fonseca J (1997) Seismic activity in Fogo and Brava Islands, Cape Verde. In: Réffega A, Figueiredo M, Silva L, Costa F, Mendes M, Torres P, da Silva P and Correia E (eds) A Erupção Vulcânica de 1995 na Ilha do Fogo, Cabo Verde. Ministério da Ciencia e da Tecnologia; Instituto de Investigação Científica Tropical, Lisbon, pp 79-91
- Heleno S (2003) O Vulcão do Fogo - Estudo Sismológico. Ph.D. thesis, Instituto Português de Apoio ao Desenvolvimento, Lisbon, pp 1-464
- Heleno S and Fonseca J (1999) A seismological investigation of the Fogo Volcano, Cape Verde Islands: preliminary results. *Volc Seis* 20:199-217
- Holm PM, Grandvoinet T, Friis J, Wilson JR, Barker AK and Plesner S (2008) An ^{40}Ar - ^{39}Ar study of the Cape Verde hot spot: temporal evolution in a semistationary plate environment. *J Geophys Res* 113(B8):B08201
- Klügel A, Hoernle KA, Schmincke H-U and White JDL (2000) The chemically zoned 1949 eruption on La Palma (Canary Islands): petrologic evolution and magma supply dynamics of a rift zone eruption. *J Geophys Res* 105(B3):5997-6016
- Klügel A, Hansteen TH and Galipp K (2005) Magma storage and underplating beneath Cumbre Vieja volcano, La Palma (Canary Islands). *Earth Planet Sci Lett* 236:211-226
- Kokfelt T (1998) A geochemical and isotopic study of the Island of Fogo, the Cape Verde Islands. PhD thesis. University of Copenhagen, pp 164
- Lodge A and Helffrich G (2006) Depleted swell root beneath the Cape Verde Islands. *Geology* 34:449-452
- Longpré M-A, Troll V and Hansteen TH (2008) Upper mantle magma storage and transport under a Canarian shield-volcano, Teno, Tenerife (Spain). *J Geophys Res* 113(B08203):11
- Longpré M-A, Troll VR, Walter TR and Hansteen TH (2009) Volcanic and geochemical evolution of the Teno massif, Tenerife, Canary Islands: some repercussions of giant landslides on ocean island magmatism. *Geochem Geophy Geosy* 10(12):Q12017
- Manconi A, Longpré M-A, Walter TR, Troll VR and Hansteen TH (2009) The effects of flank collapses on volcano plumbing systems. *Geology* 37(12):1099-1102
- Masson D, Watts A, Gee M, Urgeles R, Mitchell N, Le Bas T and Canals M (2002) Slope failures on the flanks of the western Canary Islands. *Earth-Sci Rev* 57:1-35
- Masson D, Le Bas M, Grevenmeyer I and Weinrebe W (2008) Flank collapse and large-scale landsliding in the Cape Verde Islands, off West Africa. *Geochem Geophy Geosy* 9(7)
- McGuire WJ (1996) Volcano instability: a review of contemporary themes. Geological Society, London, Special Publications 110(1):1-23
- McNutt M (1988) Thermal and mechanical properties of the Cape Verde Rise. *J Geophys Res* 93(B4):2784-2794
- Montelli R, Nolet G, Dahlen FA, Masters G, Engdahl ER and Hung S-H (2004) Finite-frequency tomography reveals a variety of plumes in the mantle. *Science* 303(5656):338-343
- Moore J, Normark W and Holcomb R (1994) Giant Hawaiian landslides. *Annu Rev Earth Pl Sc* 22(1):119-144
- Morgan WJ (1971) Convection plumes in the lower mantle. *Nature* 230(5288):42-43
- Munhá J, Mendes M, Palácios T, Silva L and Torres P (1997) Petrologia e geoquímica da erupção de 1995 e de outras lavas históricas na Ilha do Fogo, Cabo Verde. In: Réffega A, Figueiredo M, Silva L, Costa F, Mendes M, Torres P, da Silva T and Correia E (eds) A erupção vulcânica de 1995 na Ilha do Fogo, Cabo Verde. Ministério da Ciencia e da Tecnologia, Instituto de Investigação Científica Tropical, Lisbon, pp 119-132

- Nikogosian, I., Elliott, T. and Touret, J., 2002. Melt evolution beneath thick lithosphere: a magmatic inclusion study of La Palma, Canary Islands. *Chemical Geology*, 183(169-193).
- Pollitz FF (1991) Two-stage model of African absolute motion during the last 30 million years. *Tectonophysics* 194(1-2):91-106
- Presley TK, Sinton JM and Pringle M (1997) Postshield volcanism and catastrophic mass wasting of the Waianae Volcano, Oahu, Hawaii. *Bull Volcanol* 58(8):597-616
- Putirka K (1997) Magma transport at Hawaii: Inferences based on igneous thermobarometry. *Geology* 25(1):69-72
- Rhodes JM, Wenz KP, Neal CA, Sparks JW and Lockwood JP (1989) Geochemical evidence for invasion of Kilauea's plumbing system by Mauna Loa magma. *Nature* 337(6204):257-260
- Ribeiro O (1960) A Ilha do Fogo e as suas erupções, 2nd edn (The island of Fogo and its eruptions). Memorias, serie geographica I. Junta de Investigacoes do Ultramar, Ministerio do Ultramar, Lisbon
- Schmincke H-U and Sumita M (2011) Geological evolution of the Canary Islands. Görres-Druckerei und Verlag GmbH, Koblenz, pp. 196
- Schwarz S, Klügel A and Wohlgemuth-Ueberwasser C (2004) Melt extraction pathways and stagnation depths beneath the Madeira and Desertas rift zones (NE Atlantic) inferred from barometric studies. *Contrib Mineral Petrol* 147:228-240
- Stroncik N, Klügel A and Hansteen TH (2009) The magmatic plumbing system beneath El Hierro (Canary Islands): constraints from phenocrysts and naturally quenched basaltic glasses in submarine rocks. *Contrib Mineral Petrol* 157(5):593-607
- Tibaldi A (2004) Major changes in volcano behaviour after a sector collapse: insights from Stromboli, Italy. *Terra Nova* 16(1):2-8
- Tilling RI and Dvorak JJ (1993) Anatomy of a basaltic volcano. *Nature* 363(6425):125-133
- Torres P, Madeira J, Silva L, Brum da Silveira A, Serralheiro A and Mota Gomes A (1997) Carta geológica das erupções históricas da Ilha do Fogo: revisão e actualização. In: Réffega A, Figueiredo M, Silva L, Costa F, Mendes M, Torres P, da Silva T and Correia E (eds) A erupção vulcânica de 1995 na Ilha do Fogo, Cabo Verde. Ministério da Ciencia e da Tecnologia, Instituto de Investigação Científica Tropical, Lisbon, pp 119-132
- Verhoef J, Collette BJ, Dañobeitia JJ, Roeser HA and Roest WR (1991) Magnetic anomalies off West-Africa (20–38° N). *Mar Geophys Res* 13(2):81-103
- Vidal N and Merle O (2000) Reactivation of basement faults beneath volcanoes: a new model of flank collapse. *J Volcanol Geotherm Res* 99(1-4):9-26
- Voight B and Elsworth D (1997) Failure of volcano slopes. *Geotechnique* 47(1):1-31
- Walker GPL (1999) Volcanic rift zones and their intrusion swarms. *J Volcanol Geotherm Res* 94(1-4):21-34
- Wanamaker B, Wong T-F and Evans B (1990) Decrepitation and crack healing of fluid inclusions in San Carlos olivine. *J Geophys Res* 95(B10):15623-15641
- White WM, McBirney AR and Duncan RA (1993) Petrology and geochemistry of the Galápagos Islands: portrait of a pathological mantle plume. *J Geophys Res* 98(B11):19533-19563

Acknowledgements

Mein größter Dank gilt Dr. Andreas Klügel, der die Idee dieser Arbeit maßgeblich entwickelt hat und mir immer ein hervorragender Betreuer und Lehrer war, der mir viel Freiraum im Entwickeln der Arbeit gegeben hat und stets mit wertvollen Ideen aufwarten konnte, wenn ich mal nicht weiter wusste.

I want to thank Dr. Simon Day for sharing his knowledge about Fogo's geology and for his important support during the sampling process in the field.

Dr. Frank Lisker sei herzlich gedankt für die Erstellung des Zweitgutachtens.

Prof. Dr. Wolfgang Bach danke ich für die Möglichkeit zur Promotion in der AG „Petrologie der Ozeankruste“ und sein stets offenes Ohr bei allen Fragen und Problemen.

Vielen Dank geht an Dr. Thor H. Hansteen für die Mitentwicklung des Projektes und die Unterstützung meiner Arbeit.

Prof. Dr. Cornelia Spiegel sei gedankt für die Nutzung der Labore der AG „Geodynamik der Polargebiete“.

Heike Anders danke ich für die Hilfe bei der Probenaufbereitung und Durchführung der ICP-MS Analysen, Mario Thöner für Unterstützung an der Mikrosonde, Dagmar Rau und Stefan Jung für die RFA-Gesamtgesteinsanalytik, Folkmar Hauff für die Durchführung der Pb-Sr-Nd Isotopenanalytik, Brigitte Stoll und Ulrike Weis für die Hilfe am Iridium-Strip Heater, Sebastian Flotow für die Anfertigung von Dünnschliffen, und Daniel Schwander und Alexander Diehl für die Unterstützung bei der Fluideinschlussmikrothermometrie. Ein besonderer Dank gilt Jolanthe Ogermann und Anja Stöckel, die mich in verwaltungstechnischen Fragen stets profund durch den Bürokratiedschungel leiteten.

A special thanks to Bruno Faria for providing a work permit for the nature preserve of Fogo and for helpful comments on the manuscripts, and to Sandra Heleno da Silva for her interest and support of our work.

This research was supported by the Deutsche Forschungsgemeinschaft (DFG grants KL1313/9 and HA2100/12).

Meiner Bürokollegin Svenja Rausch sei herzlich gedankt für willkommene Ablenkungen und Zerstreuungen, wertvolle fachliche Diskussionen und ein offenes Ohr in allen Lebenslagen. Für wichtige moralische, technische und kalorische Unterstützung in allen Belangen gilt mein herzlicher Dank den werten Kollegen und Ehemaligen der Arbeitsgruppe „Petrologie der Ozeankruste“, namentlich Dr. Niels Jöns, Michael Hentscher, Jutta Ait-Majdari, Dr. Wolf-Achim Kahl, Li Ping Shu, Janis Thal, Dr. Eoghan Reeves, Dominik Niedermeier, Dr. Frieder Klein und Matthias Gotthieu.

Um muito obrigado por Dr. Ricardo Ramalho for comprehensive discussions about all topics of Cabo Verde, and a special thanks to Dr. Abigail Barker for helpful discussions and proofreading.

Dr. Ulrike Proske sei gedankt für die Durchsicht der Arbeit und vieles mehr.

Jikan, Neil Percival Young & Nicholas Edward Cave for guilt and company.

Sehr besonderer Dank gilt meiner Frau Katharina und unserem Sohn Lian Santino für Geduld, Erfüllung, Verständnis und Unterstützung. Meinen Eltern, die alles erst ermöglicht haben und mich während meines ganzen Lebens aufopferungsvoll unterstützt haben, und Familie Stein, die in vielen Lebenslagen eine wertvolle und selbstlose Unterstützung war und ist.

Appendix

The appendix of this thesis consists of two parts: The printed **Appendix A** comprises the electronic supplementary materials of the published and submitted papers represented by the CHAPTERS II and III; **Appendix B** represents the comprehensive electronic appendix on the accompanying CD.

Appendix A

Appendices **A1**, **A2a**, **A3 – A7** represent the electronic supplementary material of the published paper (CHAPTER II):

Hildner E, Klügel A and Hauff F (2011) Magma storage and ascent during the 1995 eruption of Fogo, Cape Verde Archipelago. Contrib Mineral Petrol, doi: 10.1007/s00410-011-0623-6

Appendices **A1**, **A2** and **A3** represent the electronic supplementary material of the submitted paper (CHAPTER III):

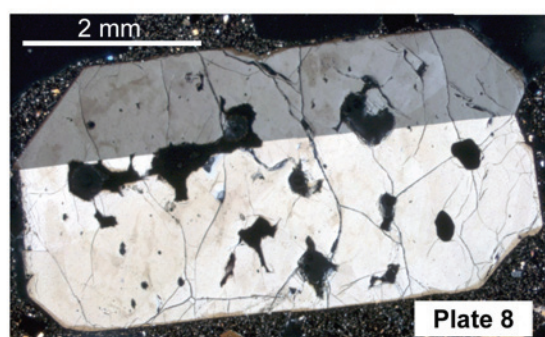
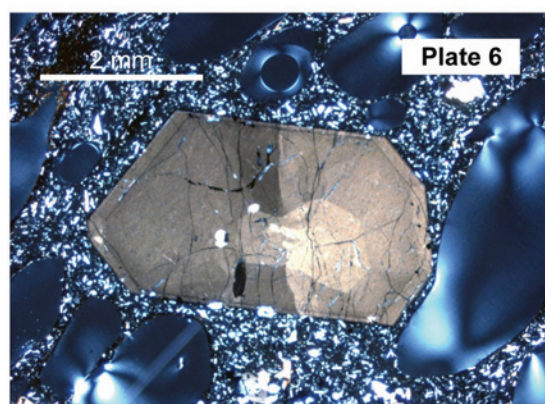
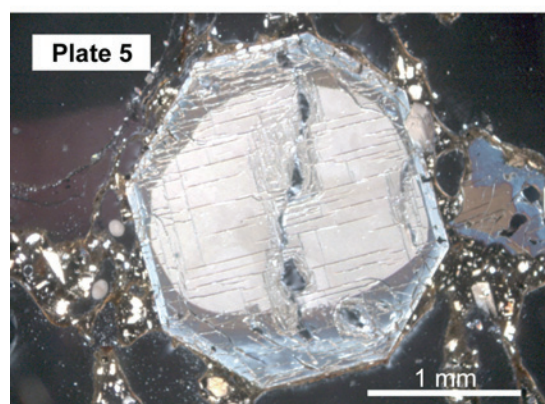
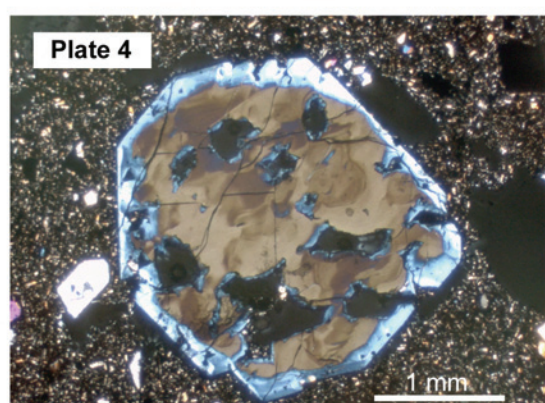
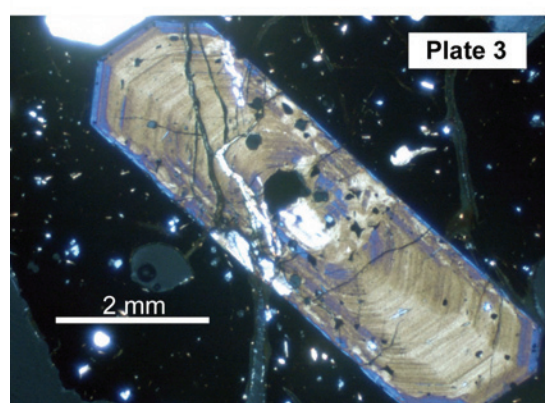
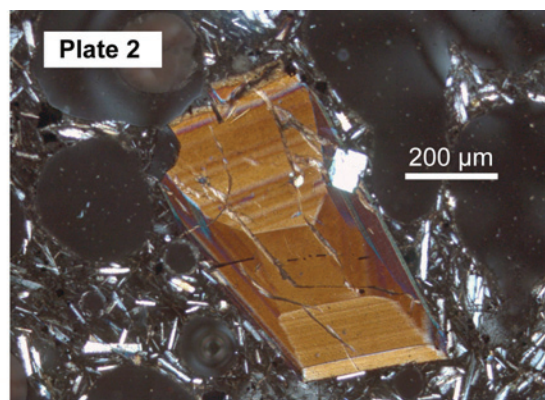
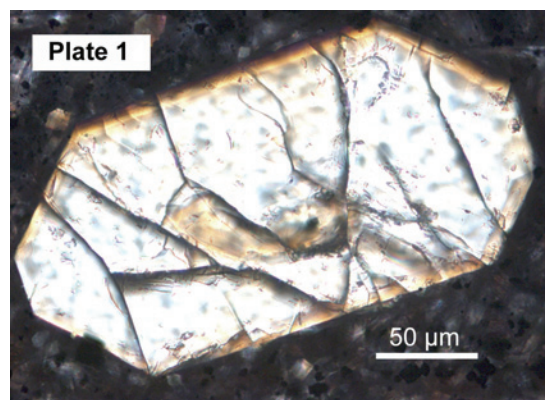
Hildner E, Klügel A and Hansteen TH (2011) Barometry of lavas from the 1951 eruption of Fogo, Cape Verde Islands: implications for historic and prehistoric magma plumbing systems (submitted to J Volcanol Geotherm Res 29.07.2011)

Color Plates - Occurrences of clinopyroxene phenocrysts

- A1** Standard measurements and reference values of EMP-analyses
- A2** Standard measurements and reference values for major and trace elements of XRF whole-rock analyses
 - a)** carried out at IFM-GEOMAR, Kiel
 - b)** carried out at Mineralogisch-Petrographisches Institut, University of Hamburg
- A3** Standard measurements and reference values of trace elements of ICP-MS analyses
- A4** Distribution coefficients (KD) and calculation of trace element fractionation
- A5** Observed versus predicted (Putirka 1999) clinopyroxene components of 1995 eruption products
- A6** Major (wt.%) and trace element (ppm) analyses of Brava and prehistoric Fogo samples used for Sr-Nd-Pb analyses. * denotes trace elements analyzed by XRF, all others by ICP-MS
- A7** Diffusion modeling data of olivine profiles of 1995 Fogo basanites

Color Plates

Clinopyroxene phenocrysts



Overview of the occurrences of clinopyroxene (Cpx) phenocrysts in historic and prehistoric Fogo lavas. All pictures were shot with crossed polarizers.

- Plate 1** Euhedral Cpx showing homogeneous core and a distinct rim phase. Very common in all Fogo samples. [Fogo 12 - Cpx 11]
- Plate 2** Euhedral Cpx showing distinct hour-glass texture. Very common in several samples; were avoided for Cpx-melt-barometry due to varying compositions depending on crystal face. [Fogo 09 - Cpx 05]
- Plate 3** Euhedral Cpx showing a pronounced growth texture within the slightly resorbed core phase and a distinct rim phase reestablishing the crystal faces. Common in Fogo lavas, especially in prehistoric ones. [Fogo 36 - Cpx 03]
- Plate 4** Euhedral Cpx showing a strongly resorbed core phase overgrown by equilibrium Cpx reestablishing the crystal faces. Common in some prehistoric samples. [Fogo 37 - Cpx 11]
- Plate 5** Euhedral Cpx showing a round resorbed core phase and two distinct equilibrium Cpx rim phases. Rather rare occurrence, predominantly in sample Fogo 16. [Fogo 16 - Cpx 01]
- Plate 6** Cpx with euhedral core phase showing undulatory extension overgrown by a distinct rim phase. The core most probably represents a xenocryst. Occur very rarely. [Fogo 15b – Cpx 01]
- Plate 7** Euhedral green-core Cpx overgrown by equilibrium Cpx. Occur very rarely, predominantly in the historic lavas. [Fogo 52 - Cpx 16]
- Plate 8** Homogeneous, slightly resorbed and twinned Cpx core overgrown by a thin zone of equilibrium Cpx. Very rare. [Fogo 37 - Cpx 10]

Appendix A1 Standard measurements and reference values of EMP-analyses

Standard	SiO ₂	TiO ₂	Al ₂ O ₃	FeO	MnO	MgO	CaO	Na ₂ O	K ₂ O	P ₂ O ₅	Cr ₂ O ₃	NiO	Total
VG2													
Average	50.65	1.87	14.00	11.96	0.17	6.77	11.24	2.78	0.19	0.18			99.81
SD	0.41	0.05	0.24	0.23	0.04	0.10	0.10	0.08	0.01	0.02			0.53
RSD%	0.82	2.88	1.71	1.94	22.48	1.49	0.93	3.03	5.58	9.42			0.54
Reference	50.81	1.85	14.06	11.84	0.22	6.71	11.12	2.62	0.19	0.2			99.86
VGA99													
Average	51.16	4.10	12.55	9.99	5.45	3.02	9.33	2.84	0.82	0.38			99.65
SD	0.31	0.06	0.20	4.23	6.56	2.37	0.08	0.08	0.02	0.03			0.52
RSD%	0.60	1.49	1.62	42.31	120.29	78.31	0.90	2.72	2.95	7.75			0.52
Reference	50.94	4.06	12.49	13.3	0.15	5.08	9.3	2.66	0.82	0.38			99.39
Kak-Augite													
Average	50.57	0.71	8.46	6.31	0.14	16.53	15.80	1.22	0.01		0.14	0.04	99.93
SD	0.38	0.09	0.59	0.11	0.03	0.14	0.26	0.05	0.00		0.02	0.02	0.99
RSD%	0.76	12.98	6.99	1.67	18.89	0.87	1.66	4.12	72.21		11.17	39.87	0.99
Reference	50.73	0.74	8.73	6.77	0.13	16.65	15.82	1.27	0				100.44
Cr-Augite													
Average	51.04	0.37	7.29	4.69	0.13	17.67	17.11	0.76	0.01	0.83	0.05		99.95
SD	0.35	0.05	0.55	0.09	0.03	0.15	0.29	0.03	0.00	0.03	0.02		0.90
RSD%	0.68	12.57	7.58	1.91	22.56	0.86	1.70	4.17	80.45	4.00	31.28		0.90
Reference	50.48	0.51	8.03	4.66	0.12	17.32	17.3	0.84	<0.1	0.85			100.11
SC-Olivine													
Average	40.67		0.03	9.49	0.13	49.58					0.01	0.36	100.35
SD	0.54		0.01	0.07	0.01	0.14					0.01	0.01	0.53
RSD%	1.33		15.30	0.70	7.38	0.29					41.10	3.30	0.53
Reference	40.67		0.03	9.49	0.13	49.58					0.01	0.36	100.35

Appendix A2 Standard measurements and reference values for major and trace elements of XRF whole rock analyses carried out at a) IFM-GEOMAR, Kiel and b) at Mineralogisch-Petrographisches Institut, University of Hamburg. Reference values are from: *Govindaraju K (1994) Compilation of working values and sample description for 383 geostandards. Geostand Newslett 18:1-158*

a)

	JB-2		JB-3		JA-2		JR-1	
	Reference	measured	Reference	measured	Reference	measured	Reference	measured
SiO₂	53.20	53.01	50.96	50.63	56.42	56.13	75.42	74.61
TiO₂	1.19	1.17	1.45	1.4	0.66	0.67	0.11	0.11
Al₂O₃	14.64	14.77	17.1	17.24	15.41	15.42	12.85	12.73
Fe₂O₃	14.3	14.46	11.85	11.99	6.21	6.38	0.89	0.85
MnO	0.31	0.21	0.17	0.18	0.108	0.11	0.1	0.11
MgO	4.65	4.75	5.2	5.25	7.6	8.07	0.1	0.15
CaO	9.85	9.87	9.8	9.76	6.29	6.24	0.65	0.69
Na₂O	2.03	2.03	2.75	2.76	3.11	3.03	4.02	4.11
K₂O	0.42	0.42	0.78	0.77	1.81	1.75	4.41	4.44
P₂O₅	0.1	0.1	0.29	0.29	0.146	0.16	0.02	0.02
Ba	220	228	245	241	315	290	46.7	52
Sr	178	180	400	404	250	241	29.4	28
Zr	51.2	45	98	89	112	97	100	91

b)

	JB-2		JB-3		JGB-1		
	Reference	measured	Reference	measured	Reference	measured	
SiO₂	53.20	54.11	50.96	50.81	43.44	44.15	
TiO₂	1.19	1.19	1.45	1.42	1.62	1.61	
Al₂O₃	14.64	14.82	17.1	17.09	17.66	17.70	
Fe₂O₃	14.3	14.32	11.85	11.81	15.16	15.30	
MnO	0.31	0.22	0.17	0.18	0.17	0.19	
MgO	4.65	4.63	5.2	5.14	7.83	7.89	
CaO	9.85	9.84	9.8	9.74	11.98	11.94	
Na₂O	2.03	2.05	2.75	2.71	1.23	1.25	
K₂O	0.42	0.42	0.78	0.75	0.24	0.23	
P₂O₅	0.1	0.10	0.29	0.28	0.05	0.05	
Ba	220	242	245	246	63	63	
Sr	178	175	400	496	321	319	
Zr	51.2	47	98	91	34	34	

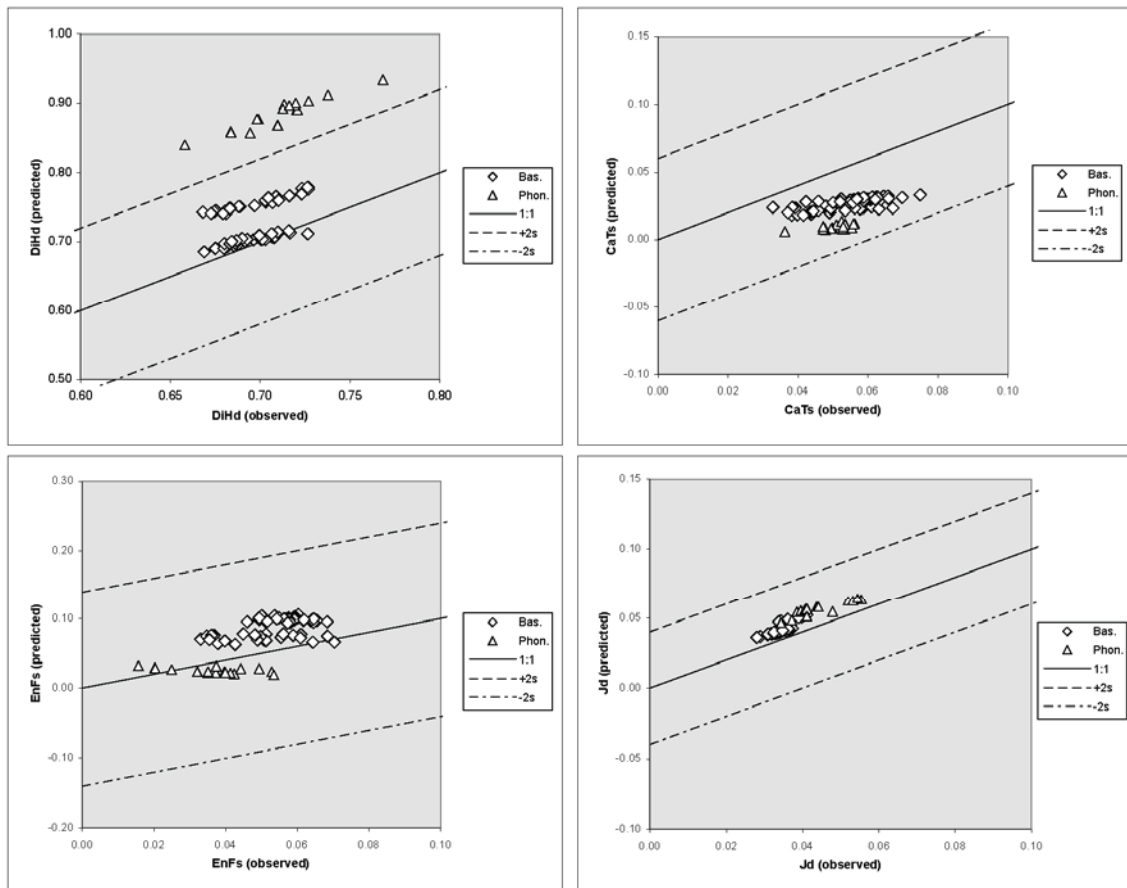
Appendix A3 Standard measurements and reference values of trace elements of ICP-MS analyses

	BCR2			BHVO2			BIR1								
	Ref.	±	Av. (13)	SD	RSD%	Ref.	±	Av. (3)	SD	RSD%	Ref.	±	Av. (2)	SD	RSD%
Li	9	2	8	1.18	15.46	4.8	0.2	2	3.02	139.61	3.6	0.2	-1.03	0.56	-54.54
Sc	33	2	38	1.51	3.96	32	1	36	0.89	2.44	44	1	50.50	1.72	3.41
V	416	14	470	11.48	2.44	317	11	357	5.71	1.60	310	11	367.76	7.74	2.10
Cr	18	2	17	0.69	4.03	280	19	328	8.30	2.53	370	8	460.67	16.75	3.64
Co	37	3	40	0.50	1.26	45	3	47	0.47	1.00	52	2	55.43	0.11	0.19
Ni	18	1	13	0.36	2.80	119	7	130	1.80	1.38	170	6	189.81	4.44	2.34
Cu	19	2	18	0.46	2.50	127	7	136	1.75	1.29	125	4	129.69	1.68	1.30
Zn	127	9	134	1.62	1.21	103	6	102	0.10	0.10	70	9	71.55	0.83	1.16
Ga	23	2	24	0.46	1.93	21.7	0.9	22.9	0.14	0.60	15.3	0.8	16.88	0.15	0.91
Rb	48	2	52	0.59	1.15	9.8	1	9.4	0.50	5.32	0.2	0.01	-0.86	0.28	-32.85
Y	37	2	36	0.46	1.28	26	2	26	0.24	0.91	16	1	15.88	0.18	1.10
Nb	12.6	0.4	12.4	0.18	1.46	18.1	2	18.2	0.18	0.97	5.55	0.05	0.53	0.05	8.79
Cs	1.1	0.1	1.0	0.17	16.30	0.1	0.001	-0.06	0.22	-366	0.01	0.003	-0.26	0.15	-56.68
La	25	1	25	0.27	1.06	15	1	16	0.17	1.10	63	0.07	0.48	0.07	15.58
Ce	53	2	54	0.73	1.36	38	2	38	0.44	1.15	1.90	0.4	1.78	0.10	5.85
Pr	6.8	0.3	6.7	0.12	1.75	5.35	0.17	5.33	0.13	2.42	0.37	0.02	0.35	0.00	1.02
Nd	28	2	28	0.79	2.85	25	1.8	24	0.80	3.30	2.50	0.7	2.30	0.01	0.25
Sm	6.7	0.3	6.7	0.14	2.11	6.2	0.4	6.3	0.19	2.97	1.12	0.02	1.10	0.03	2.37
Eu	2	0.1	2.04	0.06	2.92	2.07	0.02	2.18	0.11	4.86	0.55	0.05	0.56	0.01	2.14
Gd	6.8	0.3	7.3	0.19	2.66	6.3	0.2	6.8	0.09	1.35	1.80	0.4	2.03	0.05	2.37
Tb	1.07	0.04	1.11	0.02	1.59	0.92	0.03	0.99	0.01	1.23	0.36	0.03	0.39	0.00	1.09
Dy	6.41	0.05	6.86	0.10	1.43	5.31	0.02	5.65	0.13	2.25	4.00	1	2.84	0.14	5.10
Ho	1.33	0.06	1.41	0.03	1.78	1.04	0.04	1.06	0.03	2.59	0.56	0.05	0.64	0.02	3.20
Er	3.66	0.01	4.01	0.05	1.28	2.54	0.01	2.76	0.04	1.52	1.66	0.05	1.89	0.00	0.04
Tm	0.54	0.04	0.57	0.01	2.48	0.33	0.01	0.35	0.01	3.39	0.25	0.03	0.28	0.01	3.98
Yb	3.5	0.2	3.42	0.12	3.53	2	0.2	2.01	0.10	4.73	1.70	0.1	1.77	0.07	3.87
Lu	0.51	0.02	0.53	0.02	3.71	0.28	0.01	0.29	0.01	4.77	0.25	0.02	0.26	0.00	1.90
Hf	4.8	0.2	5.2	0.16	3.14	4.1	0.3	4.76	0.18	3.69	0.60	0.08	0.65	0.02	3.46
Ta	0.74	0.02	0.77	0.06	7.93	1.14	0.06	1.13	0.04	3.54	0.04	0.0004	0.09	0.05	53.32
Pb	11	2	9.7	0.47	4.81	1.6	0.3	1.56	0.09	5.75	3.10	0.3	2.78	0.12	4.40
Th	6.2	0.7	5.2	0.32	6.09	1.2	0.3	1.14	0.06	5.39	0.03	0.004	0.08	0.01	9.20
U	1.69	0.19	1.49	0.10	6.63	0.403	0.001	0.42	0.02	5.02	0.01	0.001	0.05	0.01	19.83

Appendix A4 Distribution coefficients (KD) and calculation of trace element fractionation for the 1995 basanites and phonotephrites. X is the fractionated portion of the respective mineral

KD	X	Li	Sc	V	Cr	Co	Ni	Cu	Zn	Ga	Rb	Sr	Y	Zr	Nb	Cs	Ba	La	Ce
OI	0.012	0.35	0.22	0.02	2.8	6.6	34	4.1	1.4	0.04	0.0004	0.0001	0.0001	0.0002	0.0002	0.0001	0.0001	0.0005	
Cpx	0.262	0.19	3	0.74	5.3	2.08	4.4	1.5	0.69	0.7	0.011	0.109	0.4	0.1	0.002	7E-05	0.0002	0.05	
Amph	0.118	0.098	6	3.4	7	2	16	1.8	0.41	0.6	0.25	0.3	0.02	0.2	0.1	0.02	0.6	0.08	
Mag	0.068	5.76	6.85	8	7.4	29	0.42	2.6	0.11	0.1	0.2	0.02	0.1	0.1	0.5	0.028	0.3	0.016	
Ap	0.015	0.027	0.22	9	0.03	0.28	0.25	0.2	1.2	1	0.2	0.1	0.05	0.05	0.05	0.3	11.2		
D _{Bulk}	0.475	0.139	3.986	2.235	6.167	2.865	11.390	1.445	0.897	0.829	0.084	0.188	0.286	0.108	0.040	0.077	0.155	0.186	
Mother (C _I)	Flow95	9	28	391	89	44	51	64	116	25	70	1009	31	390	99	0.750	771	61	
Daughter (C _O)	Fogo 09	17	4	184	4	14	3	10	115	27	129	1409	31	533	155	1.421	1214	86	
CalCebatch		15	12	246	26	23	9	53	122	28	124	1642	48	676	182	1.335	1287	99	
CalCrRayleigh		15	4	176	3	13	0.06	48	124	28	127	1702	50	692	184	1.359	1328	102	
KD	X	Pr	Nd	Sm	Eu	Gd	Tb	Dy	Ho	Er	Tm	Yb	Lu	Hf	Ta	Pb	Th	U	
OI	0.012	0.0001	0.001	0.0016	0.01	0.002	0.007	0.005	0.025	0.01	0.05	0.03	0.001	0.0003	0.001	0.0002	0.0003		
Cpx	0.262	0.1	0.2	0.3	0.29	0.25	0.33	0.31	0.4	0.27	0.4	0.35	0.35	0.25	0.01	0.008	0.007	0.006	
Amph	0.118	0.17	0.25	0.5	0.351	0.32	0.5	0.406	0.5	0.57	0.45	0.35	0.35	0.35	0.1	0.05	0.05	0.005	
Mag	0.068	0.01	0.026	0.024	0.025	0.018	0.02	0.3	0.017	0.018	0.018	0.023	0.16	0.16	0.1	0.4	0.1	0.11	
Ap	0.015	4	14	14.1	9.6	15.8	15.4	8.3	13.3	22.7	3	8.1	3	0.73	0.007	1	1		
D _{Bulk}	0.475	0.227	0.624	0.744	0.568	0.725	0.801	0.580	0.773	1.016	0.429	0.543	0.380	0.271	0.174	0.106	0.051	0.020	
Mother (C _I)	Flow95	16	60	12	3.66	10.36	1.320	7.080	1.220	2.990	0.400	2.200	0.320	8.54	5.72	3.08	4.47		
Daughter (C _O)	Fogo 09	18	63	11	3.44	9.19	1.188	6.662	1.191	3.238	0.407	2.600	0.358	8.57	6.09	8.66	2.15		
CalCebatch		25	74	14	4.63	11.91	1.457	8.841	1.368	2.967	0.549	2.810	0.453	13.05	9.41	5.35	8.13		
CalCrRayleigh		26	77	15	4.87	12.36	1.500	9.275	1.412	2.959	0.578	2.953	0.477	13.65	9.74	5.48	8.23		

Appendix A5 Observed compositions of clinopyroxene phenocrysts in basanites (Bas.) and phonotephrites (Phon.) from the Fogo 1995 eruption, compared to predicted compositions using models 3.1-3.7 of Putirka (1999). Clinopyroxene components: DiHd, diopside-hedenbergite; EnFs, enstatite-ferrosilite; CaTs, Ca-Tschermak's; Jd, jadeite. Error ranges of the predicted pyroxene compositions (dashed lines) comprise twice the standard error of estimate of the Putirka (1999) models, i.e., a 2σ uncertainty



Appendix A6 Major (wt.%) and trace element (ppm) analyses of Brava and prehistoric Fogo samples used for Sr-Nd-Pb analyses. * denotes trace elements analyzed by XRF, all others by ICP-MS

Sample	Brav 02	Brav 05	Brav 06	Brav 07	Brav 08	Brav 17	Brav 18
Rock type	phonolite	phonolite	phonolite	phonolite	phonolite	basanite	basanite
Latitude (N)	14°50.30'	14°50.30'	14°50.80'	14°51.41'	14°51.39'	14°52.02'	14°52.02'
Longitude (W)	24°42.21'	24°42.21'	24°42.45'	24°41.25'	24°41.24	24°44.43'	24°44.43'
Altitude (mNN)	800	800	900	580	580	10	10
<i>Major Elements</i>							
SiO ₂	50.23	53.04	50.58	54.70	49.34	41.99	38.54
TiO ₂	0.35	0.40	0.48	0.39	0.53	4.17	4.29
Al ₂ O ₃	21.86	20.64	20.72	20.95	21.60	14.98	11.72
Fe ₂ O ₃ t	3.40	3.71	4.01	3.87	4.03	12.53	16.35
MnO	0.19	0.27	0.21	0.22	0.20	0.20	0.18
MgO	0.53	0.26	0.76	0.35	0.46	5.71	7.73
CaO	1.44	1.49	2.46	1.37	2.61	12.00	15.00
Na ₂ O	11.08	10.21	4.88	4.78	10.45	2.69	2.66
K ₂ O	6.22	6.90	5.06	5.14	6.86	2.31	0.94
P ₂ O ₅	0.05	0.09	0.16	0.10	0.13	1.11	0.69
H ₂ O	1.17	1.69	8.76	7.13	0.81	3.21	2.02
CO ₂	0.29	0.14	0.13	0.11	0.56	0.03	0.65
Total	96.81	98.84	98.21	99.11	97.58	100.93	100.77
<i>Trace elements</i>							
Li	11.2	32.8	11.7	11.05	9.71	30.4	19.2
Sc	0.97	1.10	1.16	1.97	1.09	17.8	35.6
V	73.7	72.2	51.1	53.6	101	390	505
Cr	1.07	0.49	0.75	1.32	0.28	40.3	288
Co	1.51	1.19	1.57	0.98	2.71	26.4	55.4
Ni	0.64	0.55	1.33	2.23	0.54	23.4	134
Cu	1.07	1.09	1.79	2.11	1.50	44.0	190
Zn	144	163	121	176	147	130	138
Ga	37.6	36.5	31.3	47.7	38.0	25.5	24.5
Rb	213	220	171	214	225	72.4	28.8
Sr*	558	1098	4579	719	778	923	879
Y	11.3	22.0	33.2	16.6	19.5	47.2	32.8
Zr*	776	829	839	1482	768	557	309
Nb	108	137	144	235	106	138	67
Cs	1.95	2.52	1.70	3.48	2.65	0.75	0.30
Ba*	1142	1883	1383	315	1457	869	497
La	26.6	90.0	51.4	29.2	43.9	92.3	49.2
Ce	43.0	135	67.1	48.2	82.5	189	103
Pr	4.63	12.7	9.94	5.96	7.97	22.0	12.5
Nd	14.9	38.1	35.6	20.7	25.8	84.0	50.0
Sm	2.34	5.28	5.91	3.65	4.26	17.0	11.1
Eu	0.74	1.57	1.91	1.19	1.37	5.02	3.32
Gd	2.03	4.29	5.75	3.31	3.44	14.65	10.2
Tb	0.32	0.66	0.79	0.51	0.53	1.88	1.37
Dy	2.00	3.64	4.83	3.25	3.40	10.1	7.15
Ho	0.43	0.84	1.00	0.63	0.73	1.81	1.28
Er	1.34	2.47	2.98	1.94	2.20	4.57	3.19
Tm	0.21	0.39	0.43	0.29	0.36	0.59	0.40
Yb	1.41	2.69	2.70	2.09	2.39	3.36	2.22
Lu	0.20	0.41	0.42	0.32	0.38	0.48	0.31
Hf	12.2	13.2	12.5	26.7	11.8	9.43	6.51
Ta	1.72	2.23	3.78	6.20	1.85	7.15	3.45
Pb	12.8	9.21	8.04	12.3	12.5	4.70	2.76
Th	11.1	13.1	9.85	14.8	13.8	6.95	3.28
U	3.10	6.98	2.49	5.13	2.85	1.33	0.90

Appendix A6 (continued)

Sample	Brav 20	Brav 21	Brav 24	Brav 25	Brav 28	Fogo 19	Fogo 35
Rock type	basanite	basanite	basanite	phonolite	phonolite	tephriphon.	phonolite
Latitude (N)	14°52.23'	14°50.88'	14°50.71'	14°51.13'	14°53.24'	14°59.51'	14°53.69'
Longitude (W)	24°41.05'	24°43.85'	24°43.43'	24°40.99'	24°40.67'	24°21.80'	24°28.29'
Altitude (mNN)	250	500	550	480	0	1630	320
<i>Major Elements</i>							
SiO ₂	44.17	41.57	41.32	49.72	49.48	48.55	51.01
TiO ₂	3.15	3.25	3.15	0.55	0.38	1.77	1.04
Al ₂ O ₃	14.84	14.32	14.12	21.85	21.14	19.71	21.08
Fe ₂ O ₃ t	11.97	12.21	11.99	4.04	3.32	7.24	5.00
MnO	0.18	0.19	0.19	0.21	0.16	0.21	0.17
MgO	7.08	7.02	7.04	0.59	0.37	2.23	1.09
CaO	10.98	12.42	12.72	1.88	2.88	6.55	4.12
Na ₂ O	5.27	3.63	4.10	10.77	11.40	6.80	8.77
K ₂ O	1.00	2.23	2.64	6.72	5.98	5.13	6.26
P ₂ O ₅	0.55	0.84	0.70	0.06	0.16	0.48	0.19
H ₂ O	0.91	2.07	1.16	0.94	0.77	0.81	0.46
CO ₂	0.01	0.10	0.44	0.12	1.25	0.04	0.06
Total	100.11	99.85	99.57	97.45	97.29	99.52	99.25
<i>Trace elements</i>							
Li	12.6	18.3	12.7	10.5	10.8	26.1	15.1
Sc	25.4	24.5	25.1	1.06	1.07	4.71	2.30
V	353	321	337	101	98.5	197	132
Cr	167	180	179	0.31	0.02	16.1	1.93
Co	44.1	40.5	41.2	2.77	1.44	13.8	8.23
Ni	101	83.1	85.8	0.57	0.61	11.1	3.08
Cu	63.3	56.0	54.4	1.72	0.54	15.8	10.6
Zn	108	112	112	148	134	132	117
Ga	23.4	22.7	23.0	38.0	37.9	29.3	34.3
Rb	24.5	66.4	79.6	216	214	124	189
Sr*	894	1230	1266	624	711	2172	1847
Y	26.0	28.8	28.6	14.9	15.1	34.5	24.1
Zr*	290	327	355	765	833	623	629
Nb	65	75	76	108	130	167	131
Cs	0.64	0.57	0.62	2.39	2.31	1.75	2.79
Ba*	762	1373	1053	1415	1347	1572	1740
La	46.8	62.5	61.0	36.5	37.6	104.8	84.2
Ce	92.8	128	123	65.4	68.8	196	129
Pr	11.0	14.8	14.2	6.65	6.95	19.5	12.2
Nd	42.5	54.2	52.9	21.4	23.3	66.5	39.0
Sm	8.67	10.6	10.2	3.58	3.76	11.4	6.49
Eu	2.73	3.13	3.14	1.08	1.15	3.55	2.02
Gd	7.97	9.20	8.95	3.03	3.22	9.30	5.38
Tb	1.04	1.22	1.18	0.45	0.45	1.28	0.73
Dy	5.60	6.38	6.17	2.84	2.70	7.13	4.19
Ho	1.01	1.16	1.13	0.58	0.57	1.33	0.87
Er	2.57	2.80	2.80	1.62	1.70	3.56	2.56
Tm	0.32	0.37	0.36	0.27	0.24	0.50	0.40
Yb	1.81	1.97	1.88	1.74	1.61	2.98	2.36
Lu	0.26	0.28	0.29	0.29	0.24	0.45	0.36
Hf	6.00	6.59	6.73	11.4	12.5	9.36	8.66
Ta	3.07	3.64	3.73	1.88	2.29	6.54	3.52
Pb	3.60	2.57	2.43	12.22	6.92	10.6	18.7
Th	3.47	3.45	3.41	11.7	11.9	12.9	14.6
U	0.81	0.84	0.88	2.54	2.17	3.02	3.90

Appendix A7 Diffusion modeling data of olivine profiles of 1995 Fogo basanites. Discrepancy in Fo% between the core and rim compositions applied for the modeling and the values described in the paper, is due to the semiqualitative measurements of the olivine profiles.

Profile	Fe-Mg	Dt (m ²)	X (μm)	Length (μm)	t (h)	C0 rim (Fo%) C1 core (Fo%)	Dt (m ²)	X (μm)	Length (μm)	t (h)	C0 rim (wt.%) Cl core (wt.%)
Fogo 14_O11_T1	4.85E-13	0.7	2.8	1.23	71.6	79.1	5.82E-13	0.8	3.1	20.64	0.50
Fogo 14_O12_T1	1.26E-12	1.1	4.5	3.18	68.3	79.0	1.83E-13	0.4	1.7	6.48	1.10
Fogo 14_O14_T1_left	1.03E-12	1.0	4.1	2.62	69.9	78.6	1.93E-13	0.4	1.8	6.83	0.82
Fogo 14_O14_T1_right	7.02E-13	0.8	3.4	1.78	66.7	78.8	5.07E-14	0.2	0.9	1.80	0.83
Fogo 14_O16_T1_left	7.39E-13	0.9	3.4	1.87	70.0	78.9	8.89E-14	0.3	1.2	3.15	1.28
Fogo 14_O16_T1_right	6.10E-13	0.8	3.1	1.55	66.0	78.6	1.20E-13	0.3	1.4	4.25	1.00
Fogo 14_O11_T1_left	8.15E-13	0.9	3.6	2.07	68.1	79.7	5.12E-13	0.7	2.9	18.14	0.38
Fogo 14_O11_T1_right	9.27E-13	1.0	3.9	2.35	68.0	79.5	2.27E-13	0.5	1.9	8.04	1.09
Fogo 14_O12_T1	3.76E-13	0.6	2.5	0.95	67.7	78.6	2.44E-13	0.5	2.0	8.66	0.48
Fogo 15_O11_T1	9.93E-13	1.0	4.0	2.52	68.5	78.3	1.25E-13	0.4	1.4	4.44	1.84
Fogo 15_O11_T2	2.12E-12	1.5	5.8	5.36	67.7	78.8	1.64E-13	0.4	1.6	5.81	0.70
Fogo 15_O12a_T1	7.96E-13	0.9	3.6	2.02	69.0	78.0	1.80E-13	0.4	1.7	6.39	0.75
Fogo 15_O12a_T2	7.81E-13	0.9	3.5	1.98	66.9	79.0	2.64E-13	0.5	2.1	9.37	0.94
Fogo 15_O12b_T1	4.11E-13	0.6	2.6	1.04	66.0	78.6	1.23E-13	0.4	1.4	4.36	0.86
Fogo 15_O13_T1	2.13E-12	1.5	5.8	5.40	70.1	78.5	2.01E-13	0.4	1.8	7.14	0.50
Fogo 15_O13_T2	8.96E-13	0.9	3.8	2.27	70.9	79.6	1.67E-13	0.4	1.6	5.91	0.66
Fogo 15_O14_T1	1.54E-12	1.2	5.0	3.91	68.0	79.0	1.49E-13	0.4	1.5	5.29	1.00
Fogo 15_O14_T2	2.39E-12	1.5	6.2	6.06	70.6	79.1	2.17E-13	0.5	1.9	7.71	1.52
Fogo 15_O16_T1	6.34E-13	0.8	3.2	1.61	65.6	78.7	9.39E-14	0.3	1.2	3.33	0.73
Fogo 15_O16_T2	6.79E-13	0.8	3.3	1.72	70.4	78.9	1.80E-13	0.4	1.7	6.39	0.48
Fogo 15_O17_T1	2.67E-12	1.6	6.5	6.77	71.6	78.9	3.69E-13	0.6	2.4	13.08	0.50
Fogo 15_O17_T2	1.24E-12	1.1	4.5	3.15	71.9	79.1	1.37E-13	0.4	1.5	4.87	0.50
Fogo 15b_G101_T1	1.91E-12	1.4	5.5	4.85	73.1	78.9	1.13E-13	0.3	1.3	3.99	1.76
Fogo 15b_G102_T1	3.26E-12	1.8	7.2	8.28	71.4	78.8	9.47E-13	1.0	3.9	33.58	0.42
Fogo 15b_G103_T1_left	3.21E-13	0.6	2.3	0.81	70.5	79.1	9.74E-14	0.3	1.2	3.45	0.40
Fogo 15b_G103_T1_right	3.98E-13	0.6	2.5	1.01	74.3	79.2	1.57E-13	0.4	1.6	5.56	0.37
Fogo 15b_G104_T2_left	3.38E-12	1.8	7.4	8.57	72.6	78.8	3.84E-13	0.6	2.5	13.60	0.40
Fogo 15b_G104_T2_right	2.06E-12	1.4	5.7	5.23	72.0	78.6	3.64E-13	0.6	2.4	12.92	0.50
Fogo 15b_G105_T1_middle	6.07E-12	2.5	9.9	15.39	73.9	79.5	1.20E-13	0.3	1.4	4.24	0.57
Fogo 15b_G101_T1_right	2.82E-12	1.7	6.7	7.16	73.1	79.2	1.86E-13	0.4	1.7	6.61	0.59
Fogo 15b_G102_T1_left	4.20E-12	2.1	8.2	10.66	70.5	79.0	3.13E-13	0.6	2.2	11.11	0.40
Fogo 15b_G102_T1_right	4.21E-12	2.1	8.2	10.68	69.9	78.7	3.92E-13	0.6	2.5	13.89	0.46
Fogo 15b_G104_T1_left	3.72E-12	1.9	7.7	9.42	75.3	79.2	1.82E-13	0.4	1.7	6.46	0.55
Fogo 15b_G104_T1_right	1.86E-12	1.4	5.5	4.72	71.6	79.1	1.24E-13	0.4	1.4	4.39	0.55
Fogo 15b_G104_T2	8.90E-13	0.9	3.8	2.26	75.5	79.3	1.09E-13	0.3	1.3	3.88	0.35
Fogo 15b_G106_T1	4.25E-12	2.1	8.2	10.78	69.9	77.9	1.96E-13	0.4	1.8	6.94	1.27
Fogo 15b_G106_T3	5.80E-12	2.4	9.6	14.71	70.3	78.7	3.92E-13	0.6	2.5	14.44	0.48
Fogo 15b_G106_T5_left	6.76E-12	2.6	10.4	17.13	70.7	79.0	4.07E-13	0.6	2.6	14.44	0.48
Fogo 15b_G106_T5_right	2.51E-12	1.6	6.3	6.37	70.3	77.7	1.46E-13	0.4	1.5	5.18	0.60
Fogo 15b_G108_T1_left	6.50E-13	0.8	3.2	1.65	71.9	79.6	2.37E-13	0.5	1.9	8.41	0.70
Fogo 15b_G108_T1_right	7.41E-13	0.9	3.4	1.88	71.5	78.9	1.58E-13	0.4	1.6	5.59	0.63
Fogo 15b_G109_T1	6.49E-13	0.8	3.2	1.63	71.3	79.5	1.80	0.9	1.80	0.30	0.18
Fogo 15b_G1011_T1_left	9.73E-12	3.1	12.5	24.68	74.7	78.8	2.30E-13	0.46	1.83	33.58	1.84
Min	3.21E-13	0.6	2.3	0.81	65.6	77.7	5.07E-14	0.2	0.9	1.80	0.30
Max	9.73E-12	3.1	12.5	24.68	75.5	79.7	9.47E-13	1.0	3.9	33.58	1.84
Average	2.10E-12	1.32	5.27	5.33	70.4	78.9	2.30E-13	0.46	1.83	8.16	0.22

Appendix B (accompanying CD)

- B1** Sample list
- B2** Major and trace element whole-rock analyses of Fogo and Brava rocks
- B3** Microthermometric analyses of CO₂-dominated fluid inclusions in phenocrysts and xenoliths
- B4** Electron microprobe analyses (EMPA) of clinopyroxene (Cpx) rims conducted at IFM-GEOMAR Kiel, and calculated pressures and temperatures
- B5** Melt compositions used for Cpx-melt geothermobarometry
- B6** EMPA of matrix glasses
- B7** EMPA rim profiles of and traverses through Cpx phenocrysts
- B8** EMPA of olivine rims and cores
- B9** EMPA of traverses of olivine phenocrysts
- B10** EMPA of spinel of Fogo and Brava samples
- B11** EMPA of high-resolution qualitative profiles of olivine phenocryst rims and diffusion modeling
- B12** EMPA of high-resolution qualitative profiles of Cpx phenocryst rims
- B13** Sr-Nd-Pb isotope analyses of Fogo and Brava samples
- B14** Standard analyses and reference values for major and trace elements of XRF whole- rock analyses
- B15** Standard analyses and reference values of trace elements by ICP-MS at University of Bremen
- B16** EMPA of standard materials conducted at IFM-GEOMAR, Kiel